The background features a light blue line-art illustration of a robotic arm on the left, holding a cylindrical component. To the right is a 3D printed part with a complex, lattice-like structure. The entire scene is set against a dark blue background.

# Evaluation of Large-Format Metallic Additive Manufacturing (AM) for Steel Bridge Applications: Final Report of Tensile, Impact, and Fatigue Testing Results

Ryan J. Sherman, Ph.D., P.E.

Hannah D. Kessler, M.S.

Karl H. Frank, Ph.D., P.E.

Ronnie Medlock, P.E.

**October 2023**

## TECHNICAL REPORT DOCUMENTATION PAGE

1. Report No. GT-SEMM-23-01	2. Government Accession No.	3. Recipient's Catalog No.	
4. Title and Subtitle Evaluation of Large-Format Metallic Additive Manufacturing (AM) for Steel Bridge Applications: Final Report of Tensile, Impact, and Fatigue Testing Results		5. Report Date October 11, 2023	
		6. Performing Organization Code:	
7. Author(s) Ryan J. Sherman (ORCID 0000-0001-7525-4775), Hannah D. Kessler (ORCID 0000-0002-6135-350X), Karl H. Frank, Ronnie Medlock		8. Performing Organization Report No. GT-SEMM-23-01	
9. Performing Organization Name and Address Georgia Tech Research Corporation 926 Dalney St NW Atlanta, GA 30332		10. Work Unit No.	
		11. Contract or Grant No. 693JJ321C000032	
12. Sponsoring Agency Name and Address Office of Bridges and Structures Federal Highway Administration 1200 New Jersey Ave SE Washington, DC 20590		13. Type of Report and Period Covered	
		14. Sponsoring Agency Code	
15. Supplementary Notes			
16. Abstract Wire arc additive manufacturing (WAAM) is an additive manufacturing process capable of printing using metallic feedstocks, such as traditional welding wire consumables. Advances in WAAM allow large-scale components, measured on the scale of feet, to be fabricated. A lack of fundamental knowledge of the material and fatigue behaviors of WAAM currently prevents its widespread adoption into structural engineering. To address this need, the first objective of this work was to create material property datasets for WAAM ER70S-6 and ER80S-Ni1 through tension and notched bar impact (Charpy V-notch) tests. The second objective was to determine the influence of the as-fabricated surface finish on the fatigue behavior of WAAM ER70S-6 steel components through uniaxial fatigue tests on specimens. No significant anisotropy (difference in properties with respect to the build direction and deposition direction of the part) was noted in the yield and tensile strengths of the WAAM ER70S-6 and ER80S-Ni1 material. Low levels of anisotropy were observed in the elongation at fracture of the tensile specimens and the impact energies of the CVN specimens. The impact energies of all WAAM specimens tested at or above the AASHTO service temperatures exceeded the fracture critical Grade 50 steel requirement. Fatigue specimens with the machined surface finish exceeded the upper bound life of AASHTO fatigue detail category A. A 95 percent confidence limit regression with the slope set to 3.0 for all the as-built surface specimens exceeded AASHTO fatigue detail category D.			
17. Key Words Additive manufacturing, wire arc additive manufacturing, tension, impact, fatigue, steel bridge		18. Distribution Statement No restrictions. This document is available to the public through the National Technical Information Service, Springfield, VA 22161. <a href="http://www.ntis.gov">http://www.ntis.gov</a>	
19. Security Classif. (of this report) Unclassified	20. Security Classif. (of this page) Unclassified	21. No. of Pages 118	22. Price N/A

## SI\* (MODERN METRIC) CONVERSION FACTORS

### APPROXIMATE CONVERSIONS TO SI UNITS

Symbol	When You Know	Multiply By	To Find	Symbol
<b>LENGTH</b>				
in	inches	25.4	millimeters	mm
ft	feet	0.305	meters	m
yd	yards	0.914	meters	m
mi	miles	1.61	kilometers	km
<b>AREA</b>				
in <sup>2</sup>	square inches	645.2	square millimeters	mm <sup>2</sup>
ft <sup>2</sup>	square feet	0.093	square meters	m <sup>2</sup>
yd <sup>2</sup>	square yard	0.836	square meters	m <sup>2</sup>
ac	acres	0.405	hectares	ha
mi <sup>2</sup>	square miles	2.59	square kilometers	km <sup>2</sup>
<b>VOLUME</b>				
fl oz	fluid ounces	29.57	milliliters	mL
gal	gallons	3.785	liters	L
ft <sup>3</sup>	cubic feet	0.028	cubic meters	m <sup>3</sup>
yd <sup>3</sup>	cubic yards	0.765	cubic meters	m <sup>3</sup>
NOTE: volumes greater than 1,000 L shall be shown in m <sup>3</sup>				
<b>MASS</b>				
oz	ounces	28.35	grams	g
lb	pounds	0.454	kilograms	kg
T	short tons (2,000 lb)	0.907	megagrams (or "metric ton")	Mg (or "t")
<b>TEMPERATURE (exact degrees)</b>				
°F	Fahrenheit	5 (F-32)/9 or (F-32)/1.8	Celsius	°C
<b>ILLUMINATION</b>				
fc	foot-candles	10.76	lux	lx
fl	foot-Lamberts	3.426	candela/m <sup>2</sup>	cd/m <sup>2</sup>
<b>FORCE and PRESSURE or STRESS</b>				
lbf	poundforce	4.45	newtons	N
lbf/in <sup>2</sup>	poundforce per square inch	6.89	kilopascals	kPa
<b>APPROXIMATE CONVERSIONS FROM SI UNITS</b>				
Symbol	When You Know	Multiply By	To Find	Symbol
<b>LENGTH</b>				
mm	millimeters	0.039	inches	in
m	meters	3.28	feet	ft
m	meters	1.09	yards	yd
km	kilometers	0.621	miles	mi
<b>AREA</b>				
mm <sup>2</sup>	square millimeters	0.0016	square inches	in <sup>2</sup>
m <sup>2</sup>	square meters	10.764	square feet	ft <sup>2</sup>
m <sup>2</sup>	square meters	1.195	square yards	yd <sup>2</sup>
ha	hectares	2.47	acres	ac
km <sup>2</sup>	square kilometers	0.386	square miles	mi <sup>2</sup>
<b>VOLUME</b>				
mL	milliliters	0.034	fluid ounces	fl oz
L	liters	0.264	gallons	gal
m <sup>3</sup>	cubic meters	35.314	cubic feet	ft <sup>3</sup>
m <sup>3</sup>	cubic meters	1.307	cubic yards	yd <sup>3</sup>
<b>MASS</b>				
g	grams	0.035	ounces	oz
kg	kilograms	2.202	pounds	lb
Mg (or "t")	megagrams (or "metric ton")	1.103	short tons (2,000 lb)	T
<b>TEMPERATURE (exact degrees)</b>				
°C	Celsius	1.8C+32	Fahrenheit	°F
<b>ILLUMINATION</b>				
lx	lux	0.0929	foot-candles	fc
cd/m <sup>2</sup>	candela/m <sup>2</sup>	0.2919	foot-Lamberts	fl
<b>FORCE and PRESSURE or STRESS</b>				
N	newtons	2.225	poundforce	lbf
kPa	kilopascals	0.145	poundforce per square inch	lbf/in <sup>2</sup>

\*SI is the symbol for International System of Units. Appropriate rounding should be made to comply with Section 4 of ASTM E380.  
(Revised March 2003)

## TABLE OF CONTENTS

<b>CHAPTER 1: INTRODUCTION .....</b>	<b>1</b>
<b>CHAPTER 2: LITERATURE REVIEW .....</b>	<b>3</b>
<b>Types of Metallic Additive Manufacturing .....</b>	<b>3</b>
<b>Wire Arc Additive Manufacturing.....</b>	<b>3</b>
<b>Material Testing From the Literature .....</b>	<b>4</b>
Tension Testing.....	5
Impact Testing .....	5
Fatigue Testing.....	6
Fracture Toughness Testing.....	6
Fatigue Crack Growth Rate Testing .....	7
Hardness Testing.....	8
Other Testing .....	10
<b>Existing Large-Format Structural Applications of Metallic AM.....</b>	<b>10</b>
Oak Ridge National Laboratory (ORNL) .....	10
RAMLAB WAAMPeller .....	11
Imperial College of London.....	12
MX3D Fabrications .....	13
Tear-out Strength of WAAM Steel Plates .....	14
Darmstadt Technical University .....	14
<b>Standard Qualification .....</b>	<b>15</b>
American Society of Mechanical Engineers (ASME) .....	15
<b>CHAPTER 3: METHOD .....</b>	<b>17</b>
<b>WAAM Components .....</b>	<b>17</b>
Material Characterization Walls .....	17
Fatigue Builds .....	18
<b>Tension Testing .....</b>	<b>20</b>
Specimens .....	20
Procedure .....	22
<b>Impact Testing (Charpy V-Notch) .....</b>	<b>23</b>
Specimens .....	23
Procedure .....	24
<b>Fatigue Testing.....</b>	<b>25</b>
Machined Surface Specimens.....	25
As-built Surface Specimens.....	26
Procedure .....	27
<b>CHAPTER 4: RESULTS AND DISCUSSION .....</b>	<b>29</b>
<b>Results .....</b>	<b>29</b>
Tension Testing.....	29
Impact Testing (Charpy V-Notch).....	38
Fatigue Testing.....	46
<b>Discussion.....</b>	<b>51</b>
Tension Testing.....	51
Impact Testing (Charpy V-Notch).....	64

Fatigue Testing.....	71
<b>CHAPTER 5: WAAM APPLICATIONS IN TRANSPORTATION SECTOR.....</b>	<b>79</b>
<b>CHAPTER 6: CONCLUSIONS AND SUGGESTIONS .....</b>	<b>83</b>
<b>Conclusions.....</b>	<b>83</b>
Tension Testing.....	83
Impact Testing (Charpy V-Notch) .....	84
Fatigue Testing.....	84
<b>Suggested Future Work.....</b>	<b>85</b>
<b>REFERENCES.....</b>	<b>86</b>
<b>APPENDIX A: TENSION SPECIMEN LOCATIONS IN EACH WALL .....</b>	<b>93</b>
<b>APPENDIX B: PHOTOS OF TENSION SPECIMENS POST FRACTURE.....</b>	<b>97</b>
<b>APPENDIX C: CVN LOCATIONS IN EACH WALL.....</b>	<b>115</b>

## LIST OF FIGURES

Figure 1. Schematic. CVN and fracture propagation directions with respect to the BD and DD. ....	6
Figure 2. Schematic and Photo. Schematic of the material characterization walls under construction showing the orientation of the build and deposition directions (a) and photo of the finished material characterization wall (b). ....	17
Figure 3. Photo. Inner (spray transferred) and outer (short-circuit transferred) beads of WAAM builds. ....	18
Figure 4. Schematic and Photo. Schematic of fatigue component including dimensions (a) and photo of finished near-net component (b). ....	19
Figure 5. Photo. Cluster of pores in the grip length of specimen F80Lo-45-2. ....	21
Figure 6. Photo. Non-metallic inclusion in the grip length of specimen F80Hi-DD-2. ....	21
Figure 7. Photo. Non-metallic inclusion in the grip length of specimen F80Hi-45-1. ....	22
Figure 8. Photo. Non-metallic inclusion in the grip length of specimen F80Hi-45-2. ....	22
Figure 9. Schematic. Dimensions of Lo-M and Hi-M fatigue specimens. ....	25
Figure 10. Photo. AB fatigue specimen prior to hand finishing to remove notches from the transition and grip lengths; notches requiring removal indicated. ....	26
Figure 11. Photo. AB fatigue specimen after hand finishing to remove notches from the transition and grip lengths; typical undercut areas of gauge length width indicated. ....	27
Figure 12. Photo. Peak-to-peak width (dashed lines) and valley-to-valley width (solid lines) of an AB specimen. ....	27
Figure 13. Graph. Engineering stress-strain for F70Lo specimens. ....	34
Figure 14. Graph. Engineering stress-strain for F70Hi specimens. ....	35
Figure 15. Graph. Engineering stress-strain for F80Lo specimens. ....	36
Figure 16. Graph. Engineering stress-strain diagrams for F80Hi specimens. ....	37
Figure 17. Graph. Engineering stress-strain diagrams for all specimens. ....	38
Figure 18. Graph. Temperature versus impact energy for all F70Lo specimens. ....	43
Figure 19. Graph. Temperature versus impact energy for all F70Hi specimens. ....	44
Figure 20. Graph. Temperature versus impact energy for all F80Lo specimens. ....	45
Figure 21. Graph. Temperature versus impact energy for all F80Hi specimens. ....	46
Figure 22. Graph. S-N values for each specimen tested compared to design life AASHTO detail categories A-E'. ....	48
Figure 23. Photo. Typical fracture surface and initiation locations, fatigue crack propagation, and fast fracture (view of failure surface). ....	49
Figure 24. Photo. Typical fracture surface and initiation locations, fatigue crack propagation, and fast fracture (side view). ....	50
Figure 25. Graph. Yield strength, tensile strength, and elongation at fracture of DD specimens from the current study and the literature compared to the minimum requirements of AWS A5.18 for as-welded ER70S-6 and ASTM A709 for Grade 50 steel. ....	59
Figure 26. Photo. Internal discontinuity (circled) in gauge length of F80Hi-DD-2. ....	62
Figure 27. Graph. Contours of specimen F80Hi-45-2 showing the AM layers visible in the engineering $e_{yy}$ (vertical direction of figure) strain field. ....	63
Figure 28. Graph. Contours of specimen F80Lo-BD-3 showing the AM layers visible in the engineering $e_{yy}$ (vertical direction of photo) strain field. ....	64

Figure 29. Graph. Temperature versus impact energy for all $1/2 T$ specimens from all walls. ....	66
Figure 30. Graph. Temperature versus impact energy for BD $1/2 T$ specimens from all walls. ....	67
Figure 31. Graph. Temperature versus impact energy for DD $1/2 T$ specimens from all walls. ....	68
Figure 32. Graph. Temperature versus average impact energy for all BD $1/2 T$ specimens from all walls compared to BD specimens from the literature.....	70
Figure 33. Graph. Temperature versus average impact energy for all DD $1/2 T$ specimens from all walls compared to DD specimens from the literature. ....	71
Figure 34. Graph. S-N plot of as-built specimen data and corresponding mean regressions compared to mean life AASHTO detail categories.....	73
Figure 35. Graph. S-N plot of as-built specimen data and corresponding 95 percent confidence interval regressions compared to design life AASHTO detail categories. ....	73
Figure 36. Graph. S-N plot of machined specimen data and mean regression compared to the upper bound of AASHTO detail category A.....	74
Figure 37. Graph. S-N values for each as-built specimen tested compared to as-built surface finish specimens from the literature and AASHTO detail categories A-E.....	76
Figure 38. Graph. S-N values for each machined specimen tested compared to machined surface finish specimens from the literature and AASHTO detail categories A-E.....	77
Figure 39. Photo. Failure surface of specimen Lo-M-7 showing pores at the initiation edge.....	78
Figure 40. Drawing. Approximate locations from which tension specimens were removed from F70Lo. ....	93
Figure 41. Drawing. Approximate locations from which tension specimens were removed from F70Hi.....	94
Figure 42. Drawing. Approximate locations from which tension specimens were removed from F80Lo. ....	95
Figure 43. Drawing. Approximate locations from which tension specimens were removed from F80Hi.....	96
Figure 44. Photo. Specimen F70Lo-BD-1 in UTM grips post fracture.....	97
Figure 45. Photo. Specimen F70Lo-BD-2 in UTM grips post fracture.....	97
Figure 46. Photo. Specimen F70Lo-BD-3 in UTM grips post fracture.....	98
Figure 47. Photo. Specimen F70Lo-DD-1 in UTM grips post fracture.....	98
Figure 48. Photo. Specimen F70Lo-DD-2 in UTM grips post fracture.....	99
Figure 49. Photo. Specimen F70Lo-DD-3 in UTM grips post fracture.....	99
Figure 50. Photo. Specimen F70Lo-45-1 post fracture.....	100
Figure 51. Photo. Specimen F70Lo-45-2 in UTM grips post fracture.....	100
Figure 52. Photo. Specimen F70Lo-45-3 in UTM grips post fracture.....	101
Figure 53. Photo. Specimen F70Hi-BD-1 in UTM grips post fracture. ....	101
Figure 54. Photo. Specimen F70Hi-BD-2 in UTM grips post fracture. ....	102
Figure 55. Photo. Specimen F70Hi-BD-3 in UTM grips post fracture. ....	102
Figure 56. Photo. Specimen F70Hi-DD-1 in UTM grips post fracture. ....	103
Figure 57. Photo. Specimen F70Hi-DD-2 in UTM grips post fracture. ....	103
Figure 58. Photo. Specimen F70Hi-DD-3 in UTM grips post fracture. ....	104
Figure 59. Photo. Specimen F70Hi-45-1 in UTM grips post fracture.....	104
Figure 60. Photo. Specimen F70Hi-45-2 in UTM grips post fracture.....	105

Figure 61. Photo. Specimen F70Hi-45-3 in UTM grips post fracture.....	105
Figure 62. Photo. Specimen F80Lo-BD-1 in UTM grips post fracture.....	106
Figure 63. Photo. Specimen F80Lo-BD-2 in UTM grips post fracture.....	106
Figure 64. Photo. Specimen F80Lo-BD-3 in UTM grips post fracture.....	107
Figure 65. Photo. Specimen F80Lo-DD-3 in UTM grips post fracture.....	107
Figure 66. Photo. Specimen F80Lo-DD-4 in UTM grips post fracture.....	108
Figure 67. Photo. Specimen F80Lo-45-1 in UTM grips post fracture.....	108
Figure 68. Photo. Specimen F80Lo-45-2 in UTM grips post fracture.....	109
Figure 69. Photo. Specimen F80Lo-45-3 in UTM grips post fracture.....	109
Figure 70. Photo. Specimen F80Hi-BD-1 in UTM grips post fracture.....	110
Figure 71. Photo. Specimen F80Hi-BD-2 in UTM grips post fracture.....	110
Figure 72. Photo. Specimen F80Hi-BD-3 in UTM grips post fracture.....	111
Figure 73. Photo. Specimen F80Hi-DD-1 in UTM grips post fracture.....	111
Figure 74. Photo. Specimen F80Hi-DD-2 in UTM grips post fracture.....	112
Figure 75. Photo. Specimen F80Hi-DD-3 in UTM grips post fracture.....	112
Figure 76. Photo. Specimen F80Hi-45-1 in UTM grips post fracture.....	113
Figure 77. Photo. Specimen F80Hi-45-2 in UTM grips post fracture.....	113
Figure 78. Photo. Specimen F80Hi-45-3 in UTM grips post fracture.....	114
Figure 79. (Drawing). Approximate locations from which CVN specimens were removed from F70Lo.....	115
Figure 80. (Drawing). Approximate locations from which CVN specimens were removed from F70Hi.....	116
Figure 81. (Drawing). Approximate locations from which CVN specimens were removed from F80Lo.....	117
Figure 82. (Drawing). Approximate locations from which CVN specimens were removed from F80Hi.....	118

## LIST OF TABLES

Table 1. Welding process parameters for fracture toughness tests on WAAM ER70S-6 in the literature.....	7
Table 2. Average elastic-plastic fracture toughness of WAAM ER70S-6 in the literature.....	7
Table 3. Best-fit fatigue crack growth rate Paris law material constants for WAAM ER70S-6 in the literature.....	8
Table 4. Welding process parameters, hardness values, and approximate tensile strength per ASTM A370 on WAAM ER70S-6 in the literature.....	9
Table 5. GMAAM procedure qualification bead and layer width limits and test specimens for specimens with and without integrated backing [49].....	15
Table 6. Welding variables for each wall.....	18
Table 7. Welding variables for each fatigue build.....	20
Table 8. Number of CVN specimens for each material characterization wall.....	24
Table 9. Number of specimens tested from each component at each stress range.....	28
Table 10. Tensile test results for F70Lo specimens.....	30
Table 11. Tensile test results for F70Hi specimens.....	31
Table 12. Tensile test results for F80Lo specimens.....	32
Table 13. Tensile test results for F80Hi specimens.....	33
Table 14. Impact energy results for $\frac{1}{2} T$ F70Lo specimens.....	39
Table 15. Impact energy results for $\frac{1}{4} T$ F70Lo specimens.....	39
Table 16. Impact energy results for $\frac{1}{2} T$ F70Hi specimens.....	40
Table 17. Impact energy results for $\frac{1}{4} T$ F70Hi specimens.....	40
Table 18. Impact energy results for $\frac{1}{2} T$ F80Lo specimens.....	41
Table 19. Impact energy results for $\frac{1}{4} T$ F80Lo specimens.....	41
Table 20. Impact energy results for $\frac{1}{2} T$ F80Hi specimens.....	42
Table 21. Impact energy results for $\frac{1}{4} T$ F80Hi specimens.....	42
Table 22. Number of cycles, stress range, and R-ratio for each specimen tested.....	47
Table 23. Average notch and failure notch geometry for each specimen.....	50
Table 24. Tensile result comparison between directions tested.....	52
Table 25. Average tensile result comparison between directions tested and AWS 5.18 requirements.....	54
Table 26. Average tensile result comparison between directions tested and AWS 5.28 requirements.....	54
Table 27. Welding process and specimen parameters for available tensile tests on WAAM ER70S-6 in the literature.....	56
Table 28. Summary of specimen of available tensile tests on WAAM ER70S-6 in the literature.....	57
Table 29. Summary of specimen tensile strengths of available tensile tests on WAAM ER70S-6 in the literature.....	58
Table 30. Comparison of the average yield and tensile strengths and average percent elongation at fracture for all walls based on interpass temperature.....	61
Table 31. Ratios between the average absorbed energies of the BD and DD specimens for each wall.....	65
Table 32. Welding process parameters for CVN tests on WAAM ER70S-6 from the literature.....	69
Table 33. Detail constants, slope, and $R^2$ value for fatigue regressions for AB specimens.....	72

Table 34. Welding process and specimen parameters for available fatigue tests on WAAM ER70S-6 in the literature. ....	75
Table 35. List of potential components or applications for WAAM in the transportation sector. ....	80

## LIST OF ABBREVIATIONS

$\frac{1}{2} T$	one-half thickness CVN specimen
$\frac{1}{4} T$	one-quarter thickness CVN specimen
A	amp
AASHTO	American Association of State Highway and Transportation Officials
AB	as-built
AISC	American Institute of Steel Construction
AISI	American Iron and Steel Institute
AM	additive manufacturing, additively manufactured
Ar	argon
ASME	American Society of Mechanical Engineers
AS/NZS	Australian/New Zealand Standard
AWS	American Welding Society
BD	build direction
BJT	binder jetting
BS	British Standard
BVPC	Boiler and Pressure Vessel Code
CAD	computer-aided design
CL	confidence limit
CMT	cold metal transfer
CNC	computerized numerical control
CO <sub>2</sub>	carbon dioxide
C(T)	compact tension
CVN	Charpy V-notch
DD	deposition direction
DED	directed energy deposition
DIC	digital image correlation
EDM	electrical discharge machining
ESA	European Space Agency
F	Fahrenheit
FC	fracture critical
FCGR	fatigue crack growth rate
FE	finite element
ft	foot; feet
GMAAM	gas metal arc additive manufacturing
GMAW	gas metal arc welding
GTAW	gas tungsten arc welding
hr	hour
Hz	hertz
in	inch
ISO	International Organization for Standardization
kip	kilopound
kJ	kilojoule
ksi	kilopound per square inch
LRFD	load and resistance factor design
M	machined

MEX	material extrusion
mil	thousandth of an inch
min	minute
MJT	material jetting
N/A	not applicable
NCHRP	National Cooperative Highway Research Program
NDE	nondestructive evaluation
NFC	non-fracture critical
NN	near-net
O2	oxygen
OB	overbuilt
ORNL	Oak Ridge National Laboratory
PBF	powder bed fusion
RAMLAB	Rotterdam Additive Manufacturing Laboratorium
QAQC	quality assurance quality control
SD	standard deviation
SHL	sheet lamination
SOM	Skidmore Owings & Merrill
UTM	universal testing machine
V	volt
VPP	vat photopolymerization
WAAM	wire arc additive manufacturing, wire arc additively manufactured

## LIST OF SYMBOLS

<i>A</i>	detail category constant
<i>B</i>	number of weld beads per layer of test specimen
<i>C</i>	Paris law material constant
$e_{yy}$	strain in vertical direction
$J_{IC}$	elastic-plastic fracture toughness.
<i>m</i>	slope of the S-N curve
<i>M</i>	Paris law material constant
<i>N</i>	number of cycles
$R^2$	coefficient of determination
$R_a$	arithmetical mean height
$R_t$	maximum height
$S_r$	stress range
<i>T</i>	thickness
<i>W</i>	layer width of test specimen welded
<i>X</i>	width
<i>Z</i>	height

## CHAPTER 1: INTRODUCTION

Metallic additive manufacturing (AM) can offer an array of positive characteristics: automation, capability to fabricate geometric complexity, component optimization, consolidated assembly, digital inventory, and reduced material waste. Other large-scale metallic industries have realized and applied these advantages, including aerospace, power generation, maritime, and defense [1–4]. Wire arc additive manufacturing (WAAM) is a directed energy deposition (DED) AM process capable of printing using metallic feedstocks, such as traditional welding wire consumables. Advances in WAAM, namely its integration with robotic arms and positioners, allow large-scale components, measured on the scale of feet, to be fabricated [5]. WAAM can be an attractive option for producing large-scale structural components for these reasons. However, a current lack of fundamental knowledge of the material and fatigue behaviors of WAAM prevents its widespread adoption in the construction and transportation structure industries.

The American Welding Society (AWS) A5.18 ER70S-6 is a commonly used welding wire classification and is a matching filler metal for ASTM A709 Grade 50 steel, a grade commonly used in bridge construction and included in the Bridge Welding Code [6–8]. The tension, impact, and fatigue properties of WAAM ER70S-6 have been studied; however, the depth of knowledge is limited. AWS A5.28 ER80S-Ni1 is a common welding wire with added corrosion resistance [9]. It is commonly used as a filler metal with ASTM A709 Grade 50W steel, a grade commonly used in bridge construction when atmospheric corrosion resistance in the uncoated condition is desired [6,7]. The tension and impact properties of WAAM ER80S-Ni1 have not been studied outside of the current study.

The goal of this study was to act as a critical first step to safely advance the integration of WAAM into transportation infrastructure, thereby enabling the benefits of AM to be leveraged in steel bridge and other highway structures across the United States. The study had the following objectives:

- Create robust material property datasets for wire arc additively manufactured ER70S-6 and ER80S-Ni1 steel components through tension (ASTM A370-22) and notched bar impact (Charpy V-notch (CVN), ASTM A370-22) tests [10].
- Compare the results of the tension and impact tests of the current study to results from the literature and the specifications of AWS A5.18, AWS A5.28, and American Association of State Highway and Transportation Officials (AASHTO) *Load and Resistance Factor Design (LRFD) Bridge Design Specifications (9<sup>th</sup> Edition)* [8,9,11].
- Determine the influence of the as-fabricated surface finish on the fatigue behavior of wire arc additively manufactured ER70S-6 steel components through uniaxial fatigue tests on specimens (similar in geometry to those prescribed in ASTM E466-21 [12]).
- Compare the fatigue performance of the as-fabricated and machined surface finish specimens to the fatigue detail categories of the AASHTO *LRFD Bridge Design Specifications*.

- Draw on the outcomes of the tension, impact, and fatigue testing to determine a component or repair application that is a suitable candidate for production by WAAM and for future full-scale component or member testing.

Chapter 2 reviews the state of the literature at the time of this report, including types of metallic AM, the state of the WAAM process, material testing from the literature, and existing large-format structural applications of metallic AM. Chapter 3 describes the WAAM components manufactured for the current study and the methodology of the tension, impact, and fatigue tests performed. Chapter 4 presents the results of the tension, impact, and fatigue tests; analysis and discussion of the results; and comparison of the results to the applicable standards. Chapter 5 presents a list of potential applications of WAAM in the transportation industry based on the results of the current study and the inherent advantages of WAAM. Chapter 6 presents conclusions and suggestions based on the results of the current study.

## CHAPTER 2: LITERATURE REVIEW

### TYPES OF METALLIC ADDITIVE MANUFACTURING

Joint International Organization for Standardization (ISO) and ASTM document, ISO/ASTM 52900:2021, defines seven AM process categories for all material types: binder jetting (BJT), directed energy deposition (DED), material extrusion (MEX), material jetting (MJT), powder bed fusion (PBF), sheet lamination (SHL), and vat photopolymerization (VPP) [13]. PBF and DED processes are most widely used with metallic feedstocks.

ISO/ASTM 52900:2021 defines PBF as a “process in which thermal energy selectively fuses regions of a powder bed” [13]. A thin layer of metallic powder is leveled and preheated on a build platform in an enclosed chamber. A heat source, typically a laser or electron beam, traces the part pattern in the powder layer, creating a single fused layer. The build platform is then lowered, and a subsequent layer of powder is leveled over the existing fused layer and fused. This process repeats until the entire part has been formed [14,15]. Some PBF processes include laser beam powder bed fusion and electron beam powder bed fusion [16]. PBF processes can produce high-resolution features, internal passages, and maintain dimensional control; however, PBF production times are typically slower and build volumes are limited compared to DED processes [1,17].

ISO/ASTM 52900:2021 defines DED as a “process in which focused thermal energy is used to fuse materials by melting as they are being deposited” [13]. Normally, one or more beads of melted material are deposited in a single layer that is permitted to solidify before a subsequent layer is placed. This step is repeated until the entire part is formed [1]. Some examples of DED processes include WAAM, laser metal deposition, and direct metal printing [18]. Advances in the DED process, namely its integration with robotic arms and positioners, allow the fabrication of large-scale components measured in feet. Though DED processes are typically faster and capable of producing larger parts than PBF processes, components produced by DED processes may require more extensive post-processing than those produced by PBF.

### WIRE ARC ADDITIVE MANUFACTURING

WAAM, also known as gas metal arc additive manufacturing (GMAAM), is one of the most common forms of DED metallic AM. The WAAM process uses the same traditional welding wire as gas metal arc welding (GMAW) as the feedstock material. Welding wire is inexpensive compared to the metallic powder used in the PBF process, offering favorable economics for large-scale structures [5,19]. The energy source, a shielded arc, melts the wire, and a single layer of material is deposited. This step is repeated until the entire part is formed [17,20]. WAAM has shown promise for manufacturing large parts because it achieves higher deposition rates, leading to faster production times than other metallic AM processes [1–3]. WAAM also has a higher material usage efficiency, but the finished part is typically of a lower resolution than those produced by the PBF process [2,20]. While WAAM generally allows for greater design freedom, some design aspects (e.g., horizontal or nearly horizontal overhangs) can be challenging to fabricate [21]. However, many of these limitations can be overcome with a robotic positioner.

There are several other challenges associated with the WAAM process. Thermal cycles due to the layer-by-layer fabrication process can lead to high residual stresses and cause distortion in the finished part [19,20]. Welding and process parameters (e.g., nominal current, wire feed speed, travel speed, build path oscillation strategy of deposition, preheat temperature, and interpass temperature) have been shown to influence the material properties and discontinuities of the finished product [22]. The discontinuities that can occur in a WAAM fabrication are similar to those in traditional arc welding processes and can include porosity, cracking, and delamination. However, if the deposition process is monitored during fabrication and post-processing strategies (e.g., post-process heat treatment, interpass cold rolling, and/or interpass cooling) are implemented, research has shown that discontinuities can be minimized, and more desirable material properties can be achieved [20,23,24].

Cold metal transfer (CMT), a GMAW process based on the short-circuit transfer process, is a popular process choice in the literature that attempts to minimize residual stresses and improve shape accuracy [25,26]. Unlike the traditional GMAW process, the current cycles up and down in the CMT process to control the weld bead deposition. When the tip of the electrode contacts the molten pool, a servomotor retracts the welding wire, which causes the droplet to be deposited. During bead deposition, the current drops close to zero, significantly reducing splatter generation. After the bead is deposited, the arc is struck again, and another bead is deposited similarly [27]. Studies that used CMT in the literature did not report fusion issues. As will be discussed following, short-circuit transfer is part of the means and methods of the fabricator that produced the WAAM parts for the current study.

## **MATERIAL TESTING FROM THE LITERATURE**

Aluminum, titanium, nickel, and steel alloys (i.e., stainless and low-carbon) have all been used as feedstock for WAAM processes [18]. The tensile strength, impact energy resistance, fatigue performance, fracture toughness, fatigue crack growth rate, and hardness of these alloys have been studied to varying degrees. Most existing literature focuses on the PBF process or specialized alloys used in the aerospace, energy, or defense sectors.

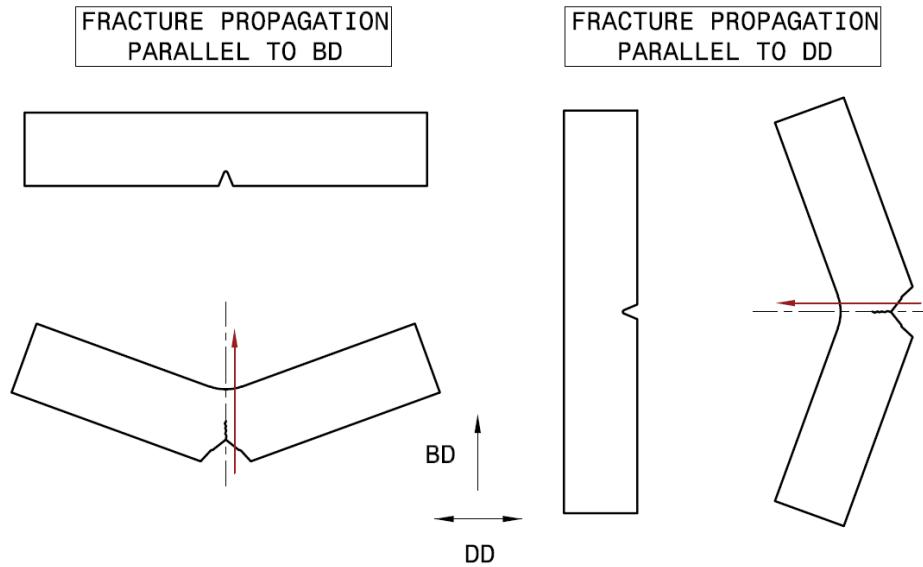
Steel bridges in the United States are commonly fabricated using carbon steel. A standard welding consumable classification for traditional welded joints in steel bridges and other transportation structures is AWS ER70S-6, a matching filler metal for ASTM A709 Grade 50 steel [6,7]. ER70S-6 is also a common feedstock for WAAM. This feedstock provides a cost-effective solution for large-scale steel structure applications and has demonstrated excellent build performance in previous large-format WAAM fabrications [28,29]. Further, the tensile and impact properties of ER70S-6 are well-aligned with traditional bridge steels. Weathering steel (ASTM A709 Grade 50W or similar) can be used for added corrosion resistance in bridge construction. For this reason, AWS ER80S-Ni1, a matching filler metal for ASTM A709 Grade 50W steel, was of interest in the current study; however, no historical material property data using ER80S-Ni1 in WAAM was available at the time of this report. For these reasons, the following historical material property data will focus on components using ER70S-6 feedstock fabricated using the WAAM process. However, it should be noted that other higher strength carbon steel WAAM feedstocks exist and have been studied to a lesser degree, namely ER90S-B, ER100S-1, and ER120S-G [26,30].

## **Tension Testing**

Thirty-three studies were identified in the existing literature that quantified the tensile properties of ER70S-6 WAAM steel [25,26,30–60]. Most studies evaluated tensile specimens in at least two directions of the build due to concerns of potential anisotropy in AM materials that may arise from the layer-by-layer fabrication process. These directions correspond to the longitudinal axis of the tensile specimen parallel to the build direction (BD) and the longitudinal axis of the tensile specimen parallel to the deposition direction (DD) (i.e., perpendicular to the build direction). Note that anisotropy is not an inherently negative attribute; it need only be understood so that designers can appropriately account for it. In addition, a small subset of studies tested specimens fabricated with their longitudinal axes oriented at a 45-degree angle between the BD and DD. At the time of this report, no published literature was available that quantified the tensile properties of ER80S-Ni1 WAAM steel. The testing conducted as a part of the current study seeks to build on the existing body of ER70S-6 WAAM tension test results and initialize a body of ER80S-Ni1 tension test results by testing specimens with respect to all three directions. Existing test data from the literature were aggregated and compared to the results of the current study in Chapter 4, Results and Discussion.

## **Impact Testing**

Eleven studies in the existing literature were identified that quantified the impact properties of ER70S-6 WAAM steel using CVN testing [33,39,49–51,60–65]. Similar to the tensile investigations in the literature, most studies that performed impact tests evaluated two sets of specimens. The first set was machined so that fracture propagated parallel to the build direction (BD), and the second set was machined so that fracture propagated parallel to the deposition direction (DD), with only one study testing additional CVNs with fracture propagation at a 45-degree angle between the BD and DD. See Figure 1 for a schematic of the CVN and fracture propagation directions with respect to the BD and DD. At the time of this report, no published literature was available that quantified the impact properties of ER80S-Ni1 WAAM steel. The testing conducted as a part of the current study seeks to build on the existing ER70S-6 WAAM impact test results and initialize a body of ER80S-Ni1 impact test results by testing CVNs with their fracture propagation oriented parallel to the BD and DD. Existing test data from the literature were aggregated and compared to the results of the current study in Chapter 4, Results and Discussion.



Source: FHWA.

**Figure 1. Schematic. CVN and fracture propagation directions with respect to the BD and DD.**

### Fatigue Testing

Six studies were identified that have investigated the fatigue performance of WAAM ER70S-6 steel [54,66–70]. These studies spanned a variety of stress ranges, R-ratios, surface roughness conditions, surface treatments, and test types. At the time of this report, no published literature quantified the fatigue performance of ER80S-Ni1 WAAM steel. The testing conducted as a part of the current study seeks to build on the existing body of ER70S-6 WAAM fatigue test results. Existing test data from the literature were aggregated and compared to the results of the current study in Chapter 4, Results and Discussion.

### Fracture Toughness Testing

Two studies that investigated the fracture toughness of WAAM ER70S-6 steel in accordance with ASTM E1820 were identified [26,30,71]. Both studies investigated two different specimen orientations: specimens with fracture propagation parallel to the BD and specimens with fracture propagation parallel to the DD. Each study tested standard compact tension ( $C(T)$ ) specimens per ASTM E1820. Note that fracture toughness tests were not performed in the current study.

Table 1 presents the welding process parameters for each fracture toughness study, and Table 2 presents the average elastic-plastic fracture toughness,  $J_{Ic}$ , for each specimen orientation.

**Table 1. Welding process parameters for fracture toughness tests on WAAM ER70S-6 in the literature.**

Reference	Process Notes	Wire Diameter (in)	Voltage (V)	Current Range (A)	Wire Feed Rate (ft/min)	Print Travel Speed (in/min)	Welding Heat Input (kJ/in)	Shielding Gas Composition <sup>a</sup> (percent)
Dirisu et al. (2019) [26]	CMT	0.047	13.3	157	21.3	15.7	8.0	80 Ar / 20 CO <sub>2</sub>
Ermakova et al. (2020) [30]	CMT	0.047	—	—	24.6	17.3	—	80 Ar / 20 CO <sub>2</sub>

— no data was reported.

**Table 2. Average elastic-plastic fracture toughness of WAAM ER70S-6 in the literature.**

Reference	Specimen Thickness (in)	Specimen Count BD	Specimen Count DD	Elastic-Plastic Fracture Toughness BD, $J_{Ic}$ (kip-in/in <sup>2</sup> )	Elastic-Plastic Fracture Toughness DD, $J_{Ic}$ (kip-in/in <sup>2</sup> )	Fracture Toughness Ratio, BD/DD
Dirisu et al. (2019) [26]	0.630	1	2	2.02	1.50	1.34
Ermakova et al. (2020) [30]	0.630	2	2	2.24	2.55	0.88

The average BD over DD ratio for the two studies was 1.11. Ermakova et al. concluded that the specimen orientation did not significantly affect the fracture toughness, but Dirisu et al. noted the significance of notch orientation in their results. Due to the limited number of fracture toughness investigations and specimens per investigation, conclusions cannot be drawn regarding the isotropy or anisotropy of WAAM ER70S-6 steel fracture toughness.

### Fatigue Crack Growth Rate Testing

One study by Ermakova et al. was identified that investigated the fatigue crack growth rate (FCGR) of WAAM ER70S-6 steel [72]. Note that the current study did not test fatigue crack growth rate. Ermakova et al. investigated two different specimen orientations: specimens with crack growth parallel to the BD and specimens with crack growth parallel to the DD. Each type of specimen was tested under Mode I fracture mechanics loading (in accordance with ASTM E647) with a load ratio (R-ratio) of 0.1 and at maximum load levels of 2.25 and 2.47 kips [73]. Six specimens were tested at each maximum load level. The FCGR results were compared to the upper bound limits of *BS7910: Guide to methods for assessing the acceptability of flaws in metallic structures* published by the British Standards Institution [74], and the results of the same tests on wrought S355G+10M structural steel, a European steel grade with a yield strength of approximately 50 ksi. The welding process parameters for this study were the same as those shown in Table 1 for their 2020 study. Lines of best fit were made for each combination of build

orientation and maximum load level to determine Paris law material constants ( $C$  and  $M$ ), as shown in Table 3.  $R^2$  in Table 3 is the coefficient of determination.

**Table 3. Best-fit fatigue crack growth rate Paris law material constants for WAAM ER70S-6 in the literature.**

Orientation	Maximum Load (kips)	C	M	R <sup>2</sup>
BD	2.25	$2.14 \times 10^{-8}$	2.74	0.950
DD	2.25	$3.76 \times 10^{-9}$	3.20	0.951
BD	2.47	$9.75 \times 10^{-9}$	2.95	0.990
DD	2.47	$3.43 \times 10^{-8}$	2.61	0.992

The DD specimens had a 100 percent longer fatigue life for the maximum load of 2.25 kips. The BD specimens had a 30 percent longer fatigue life for the maximum load of 2.47 kips. The lowest FCGR was observed in the DD specimens tested at the 2.25-kip load level, while the highest FCGR was observed in the DD specimens tested at the 2.47-kip load level. It was concluded that specimen extraction location within the WAAM-fabricated wall did not significantly affect the FCGR. In addition, the FCGR trends of the WAAM specimens fell below the upper bound trends recommended by BS7910 but above those observed from experiments on S355G+10M structural steel. The microstructural deformation mechanism was reportedly ductile for the DD specimens and brittle for the BD specimens. At this time, a conclusion cannot be drawn regarding the isotropy or anisotropy of fatigue crack growth of WAAM ER70S-6, as only one study has investigated FCGR.

### Hardness Testing

Hardness tests of WAAM ER70S-6 were identified in 18 studies [25,26,30,31,34,35,37–40,45,48,49,58,61,63,64,75]. The welding process parameters, type of hardness measure, average hardness values, and approximate tensile strength per ASTM A370 are presented in Table 4 [10]. The average value was reported if hardness values were provided at multiple locations in a study.

**Table 4. Welding process parameters, hardness values, and approximate tensile strength per ASTM A370 on WAAM ER70S-6 in the literature.**

Reference	Process Notes	Wire Diameter (in)	Voltage (V)	Current Range (A)	Wire Feed Rate (ft/min)	Print Travel Speed (in/min)	Welding Heat Input (kJ/in)	Shielding Gas Composition (Percent)	Type of Hardness Measure	Hardness	Approximate Tensile Strength per ASTM A370 (ksi)
Haden et al. (2017) [31]	—	0.035	19.0	—	16.67	5.98	—	75 Ar / 25 CO2	Vickers	141 HV	68
Adinarayanappa and Simhambhatla (2017) [75]	—	0.047	—	—	6.5-16.4	58.80	—	82 Ar / 18 CO2	Vickers	198 HV*	93
Waqas et al. (2018) [63]	—	—	—	—	—	—	—	—	Brinell	149 HB <sup>‡</sup>	71
Corpus (2019) [34]	—	0.023	30.0	160	110.00	16.00	18.0	60 Ar / 40 CO2	Rockwell	38.3 HRC	171
Dirisu et al. (2019) [26]	CMT	0.047	13.3	157	21.3	15.75	8.0	80 Ar / 20 CO2	Vickers	268 HV <sup>‡</sup>	124
Ghaffari et al. (2019) [35]	As-Printed	0.035	28.0	320	20.47	11.81	45.5	100 Ar	Vickers	160 HV <sup>‡</sup>	80
Ghaffari et al. (2019) [35]	Milled	0.035	28.0	320	20.47	11.81	45.5	100 Ar	Vickers	154 HV <sup>‡</sup>	73
Kuhne et al. (2019) [61]	—	0.039	27	255	—	15.72	26.3	92 Ar / 8 CO2	Vickers	169 HV <sup>‡</sup>	83
Muller et al. (2019) [25]	GMAW	0.039	27.6	218	34.78	—	142.8**	82 Ar / 18 CO2	Vickers	141 HV <sup>‡</sup>	68
Muller et al. (2019) [25]	CMT** Standard	0.039	11.1	158	16.41	—	66.8**	82 Ar / 18 CO2	Vickers	157 HV <sup>‡</sup>	77
Muller et al. (2019) [25]	CMT** Cycle Step	0.039	16.4	204	30.84	—	53.2**	82 Ar / 18 CO2	Vickers	172 HV <sup>‡</sup>	84
Rafieezad et al. (2019) [37]	—	0.035	28.0	320	20.47	11.81	45.5	100 Ar	Vickers	160 HV <sup>‡</sup>	80
Ron et al. (2019) [38]	—	0.047	23.9	210	20.01	5.51	54.6	98 Ar / 2 O2	Vickers	192 HV	91
Waqas et al. (2019) [39]	—	0.047	19	120	—	8.27	16.5	—	Brinell	149 HB <sup>‡</sup>	72
Aladlur et al. (2020) [40]	Overlapped	0.047	27.1	229	26.25	25.59	14.5	80 Ar / 20 CO2	Vickers	151 HV	72
Aladlur et al. (2020) [40]	Oscillated	0.047	26.6	244	26.25	7.87	49.5	80 Ar / 20 CO2	Vickers	142 HV	68
Ermakova et al. (2020) [30]	—	0.047	—	—	24.61	17.32	—	80 Ar / 20 CO2	Vickers	155 HV <sup>‡</sup>	77
Nemani et al. (2020) [45]	—	0.035	28.0	135	20.5	—	19.2	—	Vickers	160 HV	80
Ayan and Kahraman (2021) [48]	—	0.047	23	90-100	6.6	3.94	31.5-35.1	86 Ar / 12 CO2 / 2 O2	Vickers	140 HV*	68
Douglass and Schaeffer (2021) [49]	Fast Cooling Rate	—	—	—	—	—	10.0	—	Vickers	161 HV <sup>†</sup>	81
Douglass and Schaeffer (2021) [49]	Slow Cooling Rate	—	—	—	—	—	27.0	—	Vickers	152 HV <sup>†</sup>	73
Mohiuddin and Mohideen (2021) [64]	—	0.047	26-28	130-150	8.2	9.84-11.76	20.6-21.4	100 CO2	Brinell	133 HB <sup>§</sup>	64
Shamir et al. (2022) [58]	—	0.047	—	—	23.0	15.7	—	80 Ar / 20 CO2	Vickers	170.4 HV <sup>‡</sup>	83

—no data was reported.

\*500 g impact load.

\*\*Approximated based on energy per layer and layer thicknesses provided.

<sup>‡</sup>Impact load not reported in the study. The standard is 3,000 kg.

<sup>‡</sup>300 g impact load.

<sup>‡</sup>1000 g impact load.

<sup>‡</sup>Average values from tests with 500 g and 2000 g impact loads.

<sup>†</sup>10,000 g impact load.

<sup>§</sup>187.5 kg impact load.

## **Other Testing**

Several other material properties outside the scope of the current study have also been investigated for WAAM ER70S-6. These studies are briefly summarized following.

### ***Residual Stress***

High residual stresses have been shown in the literature for titanium and nickel alloys produced by WAAM, where mitigation procedures were not taken [76]. Though residual stresses are also likely to be a consideration for mild steels produced by WAAM, their magnitude and influence have not yet been investigated.

### ***Corrosion and Corrosion Fatigue***

Corrosion resistance and corrosion fatigue have been investigated in two studies by Ron et al. [38,66]. It was shown that the general corrosion resistance of WAAM ER70S-6 steel was similar to its traditionally manufactured counterpart ST-37, a low carbon steel grade with a similar chemical composition to ER70S-6. The results of the corrosion fatigue tests indicated that the WAAM ER70S-6 steel showed a much lower stress range at  $10^8$  cycles (20.3 ksi) than ST-37 (34.8 ksi). Microstructural imperfections inherent to the WAAM process were related to the lower corrosion fatigue performance.

### ***Functionally Graded Materials***

Several WAAM studies have investigated the potential of creating a functionally-graded material using ER70S-6 feedstock in combination with a second feedstock material [75,77,78]. The functionally-graded materials were created by simultaneously melting two wires of different material types or depositing several layers of one material followed by several layers of the other material. The first process created a blended transition in properties, whereas the second led to a more abrupt transition. Both methods were shown to create functionally-graded materials successfully.

## **EXISTING LARGE-FORMAT STRUCTURAL APPLICATIONS OF METALLIC AM**

Details for a small number of structural-scale components or full-size structures fabricated by WAAM are available in the existing literature. A number of the fabrications were created for demonstration purposes to showcase the potential for large-format WAAM; as such, many of these builds did not undergo structural testing. Several of these components or structures are summarized in the following sections. The examples discussed were either large-format WAAM ER70S-6 fabrications or related to structural engineering applications.

### **Oak Ridge National Laboratory (ORNL)**

Two full-scale optimized excavator arms were built in 2017 using WAAM and ER70S-6 feedstock [79,80]. The interpass temperature was targeted to stay between 392 degrees F and 662 degrees F, optimally at approximately 572 degrees F, to allow for proper layer stacking. An initial arm segment, approximately 4 feet long, was fabricated to test the design requirements.

The two final excavator arms were 7 feet tall. Each arm took approximately five days of continuous printing, weighed approximately 400 pounds, and required 14 miles of wire. One of the arms was installed on an excavator and was used for a three-day live demonstration. No mechanical failures were observed in the arm during the demonstration. Tensile experiments were performed in the build and deposition directions. Interestingly, finite element (FE) models of temperature contours of the arm at several stages during the fabrication were created; however, the results were not compared to the actual temperature contours during printing.

ORNL undertook a comparison between direct additive manufacturing (casting), indirect additive manufacturing (WAAM), and traditional fabrication through the design of a wind turbine skeleton node [81]. This skeleton node connects structural beams and other elements that carry the electrical modules to the outer enclosure of a wind turbine. The intersection of seven members in two different planes makes the shape of the node complex, costly, and time-consuming to manufacture by traditional means. The cast components were fabricated with EN-GJS-400-18-LT grade iron, the WAAM component was fabricated with ER70S-6 weld wire, and the traditionally fabricated node was manufactured with S355 structural steel. Three cast nodes were created (approximately 2,100 pounds), one node was created by WAAM (approximately 340 pounds), and one node was created by traditional manufacturing (approximately 720 pounds). Each node fit into an approximately 4.6 by 2.2 by 2.7 cubic foot volume. The cast and WAAM nodes were topology optimized before production. Note that the optimization processes for the cast nodes and the WAAM node were different. Weight reduction of the WAAM node was easier in the low-stress areas than the cast nodes because internal holes and supports could be added to the walls. The cast nodes were tested and sustained loads 4.8 times the design load without material failure (i.e., minor plastic deformation), and the WAAM node sustained loads 7.0 times the design load without material failure (i.e., minor plastic deformation). The traditionally fabricated node was not tested; rather, it was only used for a cost comparison. At the time of the report, the node fabricated by traditional means was estimated to be the most cost-effective; however, it was noted that with potential future technological advances and cost reduction, WAAM would be the most promising AM technology for the application.

### **RAMLAB WAAMPeller**

A collaboration between Rotterdam Additive Manufacturing Laboratorium (RAMLAB), Damen Shipyard, Promarin, Autodesk, and Bureau Veritas produced three different WAAM ship propellers (“WAAMPellers”) in 2017 [82,83]. The propellers were designed similarly to those used on Damen’s Stan Tug 1606, the ship used for full-scale testing. The first prototype was composed of mild steel, the second of stainless steel, and the final propeller of a nickel-bronze-aluminum alloy. The wire for the final propeller was custom-made. The propellers were 53.1 inches in diameter, weighed approximately 400 pounds, comprised of 298 layers, and took approximately 11 days to fabricate. The WAAM process created ridges in the completed component. The first two prototypes used a computerized numerical control (CNC) milling process. However, for the final WAAMPeller, a three-day hand-finishing process was used. This hand-finishing process was the same as what was used for the typical cast propellers. The final WAAMPeller was tested (i.e., bollard pull testing, speed trials, and crash stop tests), and it became the first class-approved AM propeller on November 30, 2017 by Bureau Veritas.

## Imperial College of London

In 2017, five square hollow stub-section columns of varying heights and wall thicknesses were fabricated by PBF using two different types of stainless-steel powder (PH1 and 316L) [84]. The stub columns were tested in compression. In addition, tensile specimens were printed and evaluated. While the results of this study's tensile and compressive tests do not directly provide information relating to WAAM, when these were conducted, they were believed to be the first structural tests on metallic AM cross-sections.

In 2021, compression tests were performed on 14 WAAM stainless-steel hollow square stub columns of varying cross-sectional dimensions and thicknesses [85]. These tests were performed in support of MX3D's AM pedestrian bridge, described in the following section. Geometric measurements indicated the WAAM sections had more imperfections than conventionally formed sections. When the WAAM specimens' imperfections were normalized, their compressive strength performance was similar to conventionally formed columns and those created by PBF. Compressive strength predictions of the American Institute of Steel Construction (AISC), Eurocode, and continuous strength methods were accurate or slightly conservative when effective properties of the WAAM steel were used and unconservative when machined properties were used. The WAAM columns exhibited greater variability between repeat specimens. Further testing and reliability analyses were deemed necessary to determine appropriate safety factors for WAAM columns.

In 2023, results from bending tests were reported on 14 WAAM stainless-steel hollow square stub beams of varying cross-sectional dimensions and thicknesses [86]. The WAAM beams performed similarly to traditionally produced stainless steel hollow sections, but an increased susceptibility to local buckling was noted in the more WAAM slender sections. More variability was observed in the WAAM sections' flexural capacities due to the process's inherent variability. The cross-section design provisions of Eurocode, AISC, and the continuous strength method were generally applicable to the WAAM sections. The predictions of the continuous strength method were found to be the most consistent and accurate. Further testing and reliability analyses were deemed necessary to confirm the findings of the study.

Guo et al. reported the results of 60 double-lap shear tests on WAAM bolted connections [87]. The specimens were created by waterjet cutting plates from flat-sided oval tubes made by WAAM using ER70S-6 welding wire feedstock. Two different orientations were tested: shear load parallel to the layers and shear load perpendicular to the layers. Four different sizes of ASTM F568 grade 12.9 bolts were used: M16 (0.630-inch diameter), M20 (0.787-inch diameter), M24 (0.945-inch diameter), and M30 (1.181-inch diameter). Two plate thicknesses were tested: nominally 0.102-0.114 inches and 0.291-0.311 inches. The edge distances (measured from the center of the hole) varied between 0.827 and 4.646 inches to induce different failure modes. The failure modes observed were shear-out (with or without end splitting), net section tension, and bearing failure. The orientation of the load with respect to the layers did not have a significant impact on the ultimate capacities of each connection, but the specimens that were loaded parallel to the layers were found to be more likely to fail by end splitting. When compared to the predictions of standards for structural steel (i.e., Eurocode and AISC) and cold-formed steel, American Iron and Steel Institute (AISI) and Australian/New Zealand Standard (AS/NZS), the net section tension and bearing failure capacity predictions from the structural

steel codes were more accurate than the cold-formed steel codes, but all specifications overestimated the shear-out strengths.

### **MX3D Fabrications**

Van Bolderen explored the stability of stainless-steel (Grade 308L) hollow circular columns created using WAAM [88]. These columns were fabricated by MX3D using two different strategies. The first set of columns were fabricated in a traditional continuous manner where the welding robot started at one point of the wall and traveled from that point around the perimeter of the column until it was back at the starting point. The second set of columns were fabricated in a “dot-by-dot” manner where the welding robot placed discrete “dots” of weld material around the perimeter of the shape. The dot-by-dot strategy included a waiting time between the deposition of the dots, intended to reduce induced thermal stresses. Both types of columns were tested in bending and compression to induce buckling. Four-point bend testing was performed on each specimen four times, with the specimen rotated 90 degrees about its longitudinal axis after each test. The bending stiffness of both types of specimens was lower than anticipated for the wall thicknesses and did not vary significantly between the cross sections. There was no significant difference in the buckling resistance of both types of specimens; however, the buckling loads were typically less than the expected Euler buckling load. Tensile tests were also performed in the build and deposition directions. Some anisotropy was observed during these evaluations.

To date, the largest structural application of WAAM is a pedestrian bridge (span of 34.4 feet) fabricated from Grade 308LSi stainless-steel by MX3D in collaboration with Arup [89]. Planning for the project began in 2015. The fabrication was executed over six months. Structural testing occurred during and after fabrication, including tensile testing, compression testing of stub columns, and in-situ structural load testing. The in-situ structural load test included vertical load testing of the bridge substructure (with and without the bridge deck installed) and horizontal load testing of the bridge handrails. The structural investigations confirmed that the bridge could sustain the full service design load of 44 kips. In addition, the bridge was outfitted with a smart structure network to monitor the structural performance in real-time. At completion, the bridge weighed 9.9 kips and used approximately 680 miles of wire. The bridge was opened to the public in July 2021 [90,91].

In 2019, MX3D collaborated with Takenaka, one of Japan's largest architecture, engineering, and construction firms, to design and fabricate a duplex stainless-steel connector for timber framing [92]. The hollow, tree-like connectors were optimized and manufactured with MX3D's proprietary MetalXL 3D technology. Once installed, these connectors were filled with mortar for improved buckling strength. The collaboration also involved destructive and nondestructive testing on a series of connectors. The testing demonstrated that the connectors had strong and consistent material properties. Limited information regarding the structural evaluation is included on the MX3D website.

MX3D collaborated with Skidmore, Owings & Merrill (SOM) in 2021 to design and fabricate a stainless-steel skeletal floor for a European Space Agency (ESA) supported lunar habitat design [93]. A primary objective of the design was to minimize the total mass while meeting the strength requirements. The floor was split into six segments, each of which was

fabricated vertically. Welds joined together these six segments. The fabrication process took approximately 11 days. The lunar floor, with a final weight of approximately 8.7 kips, was displayed at the 2021 Venice Biennale.

### **Tear-out Strength of WAAM Steel Plates**

Kotteman investigated the bearing and tear-out strength of WAAM plates fabricated using ER70S-6 feedstock using 46 specimens [43]. The specimens had an average thickness of either 0.118 inches or 0.236 inches (actual thickness varied because the specimens were tested in the as-fabricated condition). A 0.709-inch diameter hole was used with end distances ranging from 0.851 to 1.560 inches from the center of the hole to the edge of the plate in the direction of load application. Half of the experiments had a typical double shear bolted configuration with a nut and washer using an M16 bolt, while the other half were pinned with a smooth steel rod in double shear. The resulting force-deformation curves of the WAAM specimens were similar to a conventional steel plate connection. Kotteman recommended reduction factors based on the thickness and loading direction to account for the effective thickness of the as-fabricated material. Tensile specimens were fabricated and tested in addition to the tear-out and bearing specimens; results of these tests are presented in Chapter 4, Results and Discussion.

### **Darmstadt Technical University**

The first example of a structure fabricated in-situ was created at Darmstadt Technical University in Germany [29]. The structure, an ER70S-6 WAAM pedestrian bridge, was fabricated on-site over a creek by a welding robot. Before the in-situ full-scale bridge was fabricated, a one eighth scale model was fabricated in a controlled laboratory setting. The scaled bridge was load tested and found to have adequate strength. The full-scale bridge (approximately an eight-foot span) was created in two symmetrical halves joined in the middle using a traditional welded connection [41]. One of the largest challenges associated with the fabrication was that the build direction was not vertical, as typically performed for WAAM fabrication. The cantilevered elements of the bridge were created by depositing the first layer horizontally, and subsequent layers were placed at an incline of 45 degrees. This process helped to prevent the dripping of the layers as they cooled. Initially, each layer was deposited along the entire transverse length of the bridge; however, as the build progressed, deformations due to thermally induced residual stresses caused the cross section to twist. As such, the fabrication strategy was modified to divide the transverse width into five segments. The middle segment of the transverse width was fabricated first, followed by each side. Results of material and load tests for the full-scale bridge are forthcoming.

The research group at Darmstadt Technical University has also presented several optimized AM alternatives to typical structural details. The following have been fabricated using WAAM [94]. Currently, no material or structural test data are available for these structural details.

- A double-angle connection was optimized into a beam hook connection and fabricated directly on a structural column;
- A stiffener was fabricated directly onto a beam;

- A node for connecting four members of a space truss was optimized and fabricated; and
- A conventional clamping element was optimized and fabricated on a beam web.

In addition, a *T*-stub end plate connection was optimized and fabricated [95]. Three specimens were tested, each comprised of one optimized L-shaped AM-fabricated connector fabricated directly onto a thin steel baseplate. The AM L-shaped specimen was then bolted to a welded steel L-shape of much greater stiffness, similar to a back-to-back angle detail, using an M20 bolt. A tensile load was applied to the free (i.e., not bolted) legs of the L-shaped connections, resulting in an eccentrically applied load to the connection. The average measured load-bearing capacity of the connection was 36.7 kips, with a standard deviation of 0.90 kips. These results were not compared to any calculated capacities.

## STANDARD QUALIFICATION

### American Society of Mechanical Engineers (ASME)

The American Society of Mechanical Engineers (ASME) Code Case 3020 is evaluating the qualification of DED-GMAAM for use in the Boiler and Pressure Vessel Code (BPVC) [49]. GMAAM is an extension of current industry experience and research; as such, it was selected as the first DED process incorporated [96]. The code case specifies a qualification procedure that tests the extremes of cooling rates. Specimens (tensile and impact energy) must be fabricated and tested using the highest heat input and highest interpass temperature and at the lowest heat input and lowest interpass temperature. Other considerations for GMAAM welding procedure qualification are the number of weld beads per layer and overall layer width. Additionally, bending specimens must be fabricated and tested. The qualification procedure from Code Case 3020 is reproduced in Table 5 [49].

**Table 5. GMAAM procedure qualification bead and layer width limits and test specimens for specimens with and without integrated backing [49]**

Number of Weld Beads per Layer of Test Specimen, B	Layer Width of Test Specimen Welded, W (in)	Number of Weld Beads per Layer Qualified	Maximum Layer Width Qualified	Required Number of Tension Tests, QW-150*	Required Number of Side Bend Tests, QW-160*	Required Number of CVN Tests, QW-170*
1	$\leq \frac{1}{2}$	1 to 2	2W	4 (2)	6 (4)	6 (3)
2 to 8	< 1	2 to 2B	2W	4 (2)	6 (4)	6 (3)
2 to 8	1 to 2	2 to 2B	2W	4 (2)	6 (4)	6 (6)
> 8	$\geq 2$	2 to unlimited	unlimited	4 (2)	6 (4)	9 (6)

\*Value in parentheses indicates quantity without integrated backing.

ASME sponsored a research project conducted at Lincoln Electric Additive Solutions to validate the rules presented in Table 5. The main variables studied in this project were heat input, interpass temperature, transfer mode, and wall thickness [97]. The impact of these

variables was assessed through tension and CVN testing, with specimens oriented in the  $X$  (width),  $T$  (thickness), and  $Z$  (height) directions (if the wall was thick enough to permit extraction of specimens in the  $T$  direction). All walls were produced using ER70S-6 welding wire feedstock. Three different wall sizes were produced: 1-bead walls, 3-bead walls, and unlimited bead walls (containing more than 20 beads in any given layer). Walls were created using two different transfer modes (i.e., spray and short-circuit), two different heat inputs (i.e., low: 10-12 kJ/inch and high: 21-23 kJ/inch), and two different interpass temperatures (i.e., low: 250 degrees F and high: 750 degrees F). Forced heating was required to maintain the high interpass temperature on some walls. It was concluded that the tension and CVN properties were isotropic, the “bracketed cooling rate” approach provided satisfactory repeatability of mechanical properties, and the results were in keeping with what is historically known about deposited weld metal.

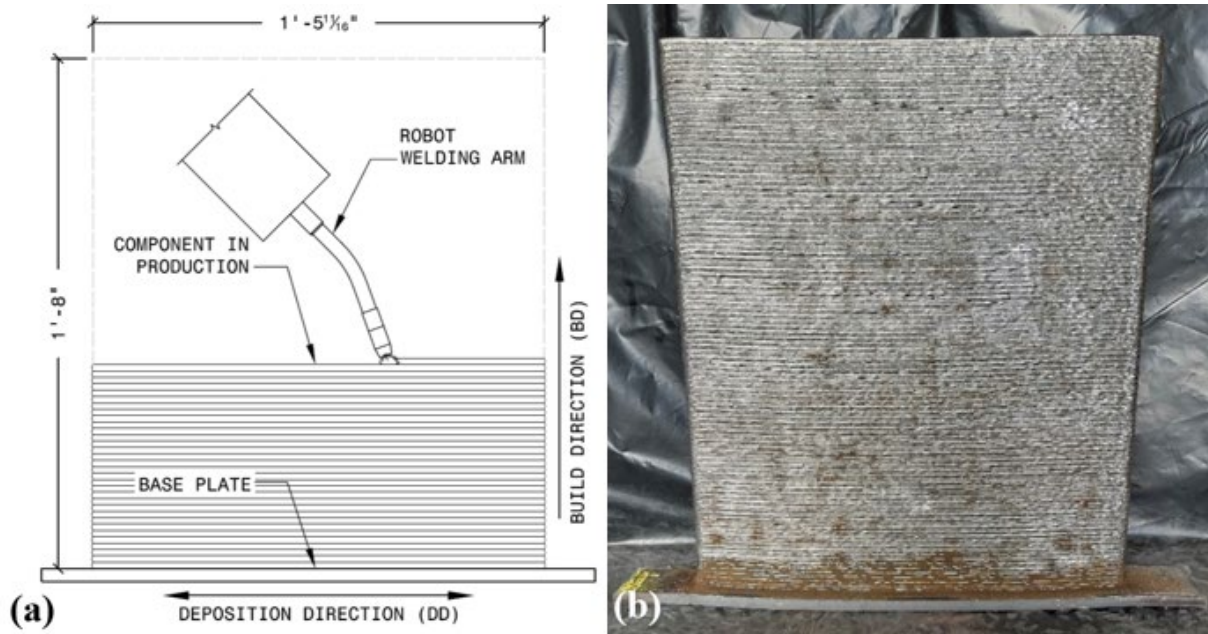
## CHAPTER 3: METHOD

### WAAM COMPONENTS

WAAM can be an option for producing large-scale structural components because it is capable of producing parts on the scale of feet with traditional welding wire consumables and commercial robotic welding hardware. ER70S-6 was chosen as a feedstock for this study because its impact and tensile properties are aligned with traditional bridge steels and the literature has shown it to have promising performance as a WAAM feedstock. ER80S-Ni1 was chosen as a feedstock for the current study because it is compatible with weathering steel (ASTM A709 Grade 50W) and its performance as a WAAM feedstock has yet to be characterized.

### Material Characterization Walls

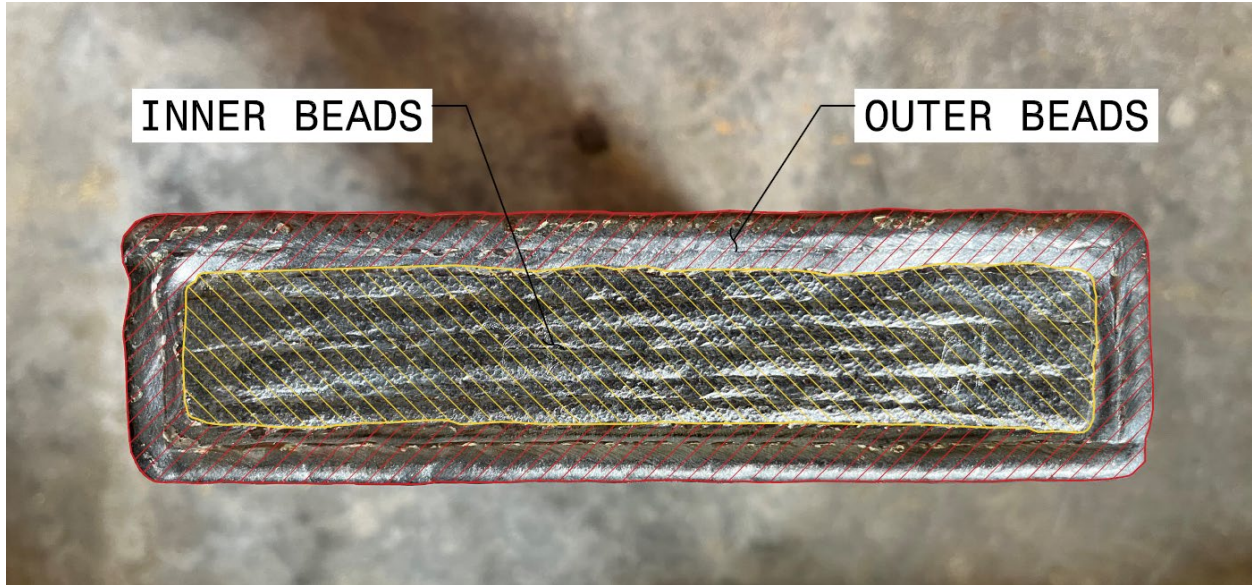
Four material characterization walls with approximate dimensions of 1 foot 5 <sup>11</sup>/<sub>16</sub> inches wide by 1 foot 8 inches tall by 1 <sup>1</sup>/<sub>8</sub> inches thick were fabricated using WAAM. Figure 2 shows a schematic and a photo of the material characterization walls under construction and the orientation of the build and deposition directions. Per the fabricator's means and methods, the outer beads of each layer were short-circuit transferred and the inner beads of each layer were spray transferred (Figure 3). Table 6 provides the wire type, wire diameter, average heat input for the outer and inner beads, average interlayer temperature, total print time, and shielding gas composition for each wall.



Source: FHWA

Source: FHWA

**Figure 2. Schematic and Photo. Schematic of the material characterization walls under construction showing the orientation of the build and deposition directions (a) and photo of the finished material characterization wall (b).**



Source: FHWA

**Figure 3. Photo. Inner (spray transferred) and outer (short-circuit transferred) beads of WAAM builds.**

**Table 6. Welding variables for each wall.**

Wall ID	Wire Type	Wire Diameter (in)	Average Heat Input, Outer Bead (kJ/in)	Average Heat Input, Inner Bead (kJ/in)	Average Interlayer Temp. (°F)	Total Print Time (hr)	Shielding Gas Composition (Percent)
F70Lo	ER70S-6	0.045	11.0	19.0	250	63.7	90 Ar / 10 CO2
F70Hi	ER70S-6	0.045	10.5	18.5	590*	23.5	90 Ar / 10 CO2
F80Lo	ER80S-Ni1	0.045	11.0	14.5	250	60.9	95 Ar / 5 CO2
F80Hi	ER80S-Ni1	0.045	11.5	14.5	710	25.9	95 Ar / 5 CO2

\*The infrared temperature sensor was not active during the build. The average temperature was generated from two manual measurements with a handheld thermocouple probe.

### Fatigue Builds

Four fatigue components were fabricated by WAAM. The components' shapes were determined by creating a fatigue specimen cross section based on the specimen described in Section 5.2.2.1 of ASTM E466-21 [12]. The cross section was extruded at a distance of approximately 7 1/4 inches to enable eight one-half inch fatigue specimens to be sliced from each component (Figure 4a). Two types of fatigue components were fabricated: two “near-net” (NN) components which had dimensions as close to the final desired specimen cross-section as possible; and two “overbuilt” (OB) components which were oversized by approximately 0.2 inches in each direction such that the as-built surface finish could be machined smooth. Two different target interpass temperatures were selected for testing (i.e., 250 degrees F and 750 degrees F), representing the lower and upper bounds of typical fabrication for the fabricator.

The outer beads of each layer were short-circuit transferred, and each layer's inner beads were spray transferred per the fabricator's means and methods (Figure 3). Figure 4b shows a finished fatigue component. Components were named based on their corresponding interpass temperature ("Lo" for 250 degrees F or "Hi" for 750 degrees F) and surface finish condition ("AB" for as-built or "M" for machined); for example, component "Hi-AB" was built with the high interpass temperature of 750 degrees F and remained with the as-built surface finish condition. The wire type, wire diameter, average heat input for the outer and inner beads, average interlayer temperature, total print time, and shielding gas composition for each wall are presented in Table 7.

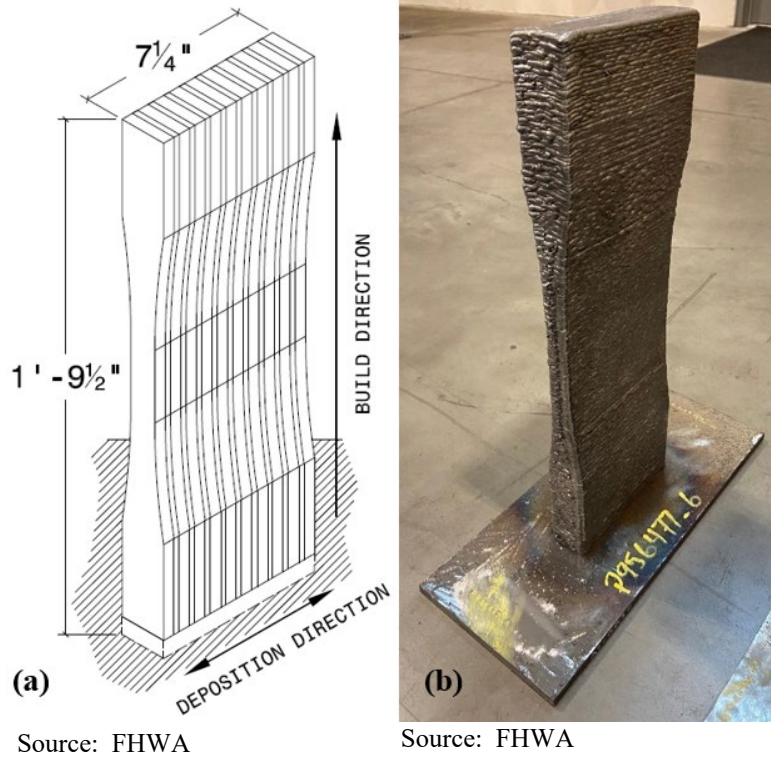


**Figure 4. Schematic and Photo. Schematic of fatigue component including dimensions (a) and photo of finished near-net component (b).**

**Table 7. Welding variables for each fatigue build.**

<b>Component ID</b>	<b>Wire Type</b>	<b>Wire Diameter (in)</b>	<b>Average Heat Input, Outer Bead (kJ/in)</b>	<b>Average Heat Input, Inner Bead (kJ/in)</b>	<b>Average Interlayer Temp. (°F)</b>	<b>Total Print Time (hr)</b>	<b>Shielding Gas Composition (Percent)</b>
Lo-M	ER70S-6	0.045	11.0	17.0	250	94.6	90 Ar / 10 CO2
Lo-AB	ER70S-6	0.045	11.0	18.0	250	66.0	90 Ar / 10 CO2
Hi-M	ER70S-6	0.045	10.0	17.0	750	24.9	95 Ar / 5 CO2
Hi-AB	ER70S-6	0.045	10.0	17.0	750	19.5	95 Ar / 5 CO2

## TENSION TESTING

### Specimens

To evaluate tensile properties, 1/2 inch thick sheet-type specimens with dimensions per ASTM A370-22 Section 9.2 were manufactured from four nominally 1 1/8 inch thick AM walls produced by WAAM [10]. Twenty-seven total specimens were removed from walls F70Lo, F70Hi, and F80Lo: three each with their longitudinal axes parallel to the BD, three each with their longitudinal axes parallel to the DD, and three each with their longitudinal axes at a 45-degree angle to the build and deposition directions (45). Eight total specimens were removed from wall F80Hi: three with their longitudinal axes parallel to the BD, two with their longitudinal axes parallel to the DD, and three with their longitudinal axes at a 45-degree angle to the build and deposition directions (45). The approximate locations from which the specimens were removed from each wall are shown in Appendix A.

Specimens are labeled in the following format “WALL ID-ORIENTATION-SAMPLE#.” For example, specimen “F70Lo-BD-2” is specimen number 2 taken from wall F70Lo with its longitudinal axis parallel to the build direction. Specimens were measured with calipers to the nearest 0.001 inches per ASTM A370-22 and visually inspected for manufacturing discontinuities. Specimen F80Lo-45-2 had a small cluster of pores in one of its grip lengths (Figure 5). Specimens F80Hi-DD-2, F80Hi-45-1, and F80Hi-45-2 had non-metallic inclusions in their grip lengths (Figure 6 through Figure 8).



Source: FHWA.

**Figure 5. Photo. Cluster of pores in the grip length of specimen F80Lo-45-2.**



Source: FHWA.

**Figure 6. Photo. Non-metallic inclusion in the grip length of specimen F80Hi-DD-2.**



Source: FHWA.

**Figure 7. Photo. Non-metallic inclusion in the grip length of specimen F80Hi-45-1.**



Source: FHWA.

**Figure 8. Photo. Non-metallic inclusion in the grip length of specimen F80Hi-45-2.**

### Procedure

Per ASTM A370-22 Section 14.4.2, any fracture outside the middle 50 percent of the gauge length is of concern because it could cause abnormally low or unrepresentative elongation values [10]. If the minimum value of the desired elongation is still achieved with a break outside

the middle 50 percent of the gauge length, the test results are considered acceptable. Because the current research is some of the first tensile tests on WAAM ER70S-6 and the first tensile tests on WAAM ER80S-Ni1, care was taken to ensure that the machine and grips were in proper alignment such that a representative dataset could be achieved. Additionally, a virtual extensometer in the digital image correlation (DIC) post-processing software was used to determine the elongation at fracture following the completion of the test; therefore, the extensometer placement could be adjusted along the length of the reduced section to capture the elongation at fracture of the specimen best.

The alignment of the universal testing machine (UTM) grips was verified using analog dial calipers. For a vertical travel distance of 4.0 inches, the lateral variation in the front-back and left-right directions was within plus or minus 0.001 inches. Additionally, alignment was checked using an American Iron and Steel Institute (AISI) 1018 bar specimen. This bar was aligned within 0.5 degrees from vertical in the lower grip, after which the upper grip was clamped at a 3.0-inch separation distance. A 1-inch gauge length clip-on extensometer was used to monitor the specimen's modulus of elasticity for tests ranging between 0 and 2 kips. Five tests were conducted with the extensometer clipped to the front of the specimen and five tests with the extensometer clipped to the back. The modulus of elasticity determined from the tests during which the extensometer was clipped to the front and back of the specimen were 29,820 plus or minus 348 ksi and 29,878 plus or minus 319 ksi, respectively. The expected modulus of elasticity value was 29,733 ksi. There was not a statistically significant difference between the front and back orientations and the expected value; as such, it is unlikely that there was significant bending moment, torsion, or angular misalignment. All specimens, except for F70Lo-45-1, were tested on the UTM which underwent the above alignment verification. Specimen F70Lo-45-1 was tested on a UTM which was not within alignment tolerances.

The UTM was set to a crosshead speed equal to 0.003 inches/min (0.0015 plus or minus 0.003 inches/inch/min of the 2.0-inch original parallel reduced section), which was acceptable per ASTM A370-22 Section 8.4 [10]. During testing, DIC was used to monitor the full strain field on the front of each specimen. An onboard data acquisition system was synchronized to acquire load values from the UTM while each picture was taken. Photographs were taken at a rate of 1 Hz for specimen F70Lo-45-1 and a rate of 0.5 Hz for all other specimens. Strain calculations were performed with Gaussian weights using a step size of 7 pixels and a subset size of 29 pixels. Following the strain analysis, a virtual extensometer of 2.0 inches length was used to determine the strain history during the duration of the test.

## **IMPACT TESTING (CHARPY V-NOTCH)**

### **Specimens**

Charpy V-notch (CVN) impact testing is an inexpensive and efficient evaluation to gain an indirect measure of a material's resistance to fracture. Current material specifications for base metal specify minimum CVN impact energy requirements for all bridge steels. As such, standard-sized CVN specimens were extracted from the four walls and tested in the current study [10]. The notched face and face opposite of the notch were machined using wire electrical

discharge machining (EDM), while the remaining two faces were surface ground. Wire EDM has been shown to cause residual stresses on the cut surfaces of steel. These stresses affect a depth less than 0.002 inches from the surface of the cut and relax significantly over time [98]. For these reasons, wire EDM was deemed an acceptable machining method, and the residual stresses at the cut surfaces were neglected. After the standard sized blanks were produced, a standard sized V-notch broach was used to cut the notch into each specimen. Note that several specimens were produced that were out of tolerance due to internal discontinuities within some of the material characterization walls. Additionally, the notch on several specimens was also broached too deep, not due to internal discontinuities. All specimens that were outside of dimensional tolerance were still tested for informational purposes, but their values were redacted from the data analysis.

CVN specimens were extracted at two points through the thickness of the walls: the middle of the thickness ( $1/2 T$ , nominally  $9/16$  inches from the outer edge of the wall) and the quarter point of the thickness ( $1/4 T$ , nominally  $9/32$  inches from the outer edge of the wall). Specimens were also extracted with their notches parallel to the BD and parallel to the DD. A total of 272 CVN specimens were tested. Table 8 shows the number of specimens of each orientation and thickness location that were tested from each wall.

**Table 8. Number of CVN specimens for each material characterization wall.**

Wall ID	Number of $1/2 T$ BD Specimens	Number of $1/2 T$ DD Specimens	Number of $1/4 T$ BD Specimens	Number of $1/4 T$ DD Specimens
F70Lo	28	29	5	6
F70Hi	29	30	6	6
F80Lo	28	30	6	6
F80Hi	23	28	6	6
Total	108	117	23	24

CVN specimens were labeled in the following format “WALL ID-NOTCH ORIENTATION-SAMPLE#.” For example, specimen “F70Lo-BD-2” is specimen number 2 taken from wall F70Lo with its notch parallel to the build direction (i.e., longitudinal axis perpendicular to the build direction), and F80Hi-DD-12 is specimen number 12 taken from wall “F80Hi” with its notch parallel to the deposition direction (i.e., longitudinal axis perpendicular to the build direction). CVN specimens were measured to the nearest 0.001 inches and visually inspected for manufacturing discontinuities. The notch of each CVN specimen was verified using a go-no-go gauge to ensure that the ligament length of each specimen was 0.315 plus or minus 0.001 inch.

## Procedure

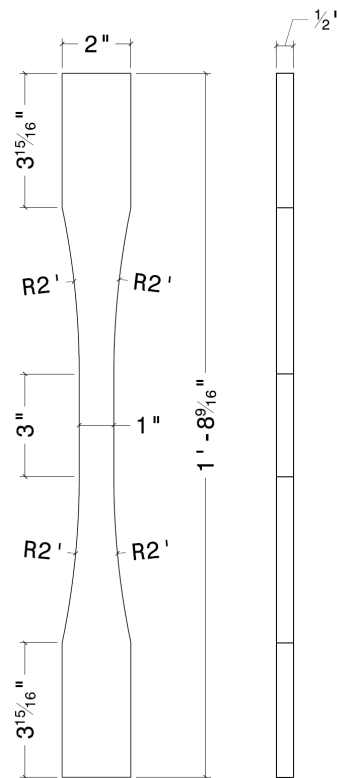
Sets of two to four  $1/2 T$  specimens of each orientation (i.e., BD and DD) from each plate were tested at seven temperature levels (i.e., -110, -90, -60, -30, 10, 40, and 70 degrees F) to develop a temperature-transition curve. Sets of three to six  $1/4 T$  specimens were tested at -30 degrees F. All specimens were tested per ASTM A370-22 on an impact tester with a useable

range of 440 ft-lbf. Prior to testing, specimens were held in a temperature-controlled bath for a minimum of five minutes at the desired test temperature. Specimens were transferred from the bath to the anvils of the impact tester and broken within five seconds. The angular encoder of the impact tester measured and converted the angular rotation of the hammer to the corresponding absorbed energy. The measured absorbed energy was recorded as each specimen was broken.

## FATIGUE TESTING

### Machined Surface Specimens

Machined (M) surface finish fatigue specimens of  $\frac{1}{2}$  inch thickness were extracted from each overbuilt fatigue component. All machined faces were ground to a surface finish of less than 40 microinches. The profile of the machined surface finish coupon is shown in Figure 9. The cross-sectional area (0.5 inches squared) in the reduced section and the gauge length (3 inches) for each type were consistent. The dimensions of the reduced section were measured to the nearest 0.001 inches, and the specimens were visually inspected for any apparent discontinuities. Specimens are labeled in the following format "INTERPASS TEMP.-SURFACE FINISH-SAMPLE#." For example, specimen Lo-M-3 is specimen number 3, taken from the low interpass overbuilt component with a machined surface finish.



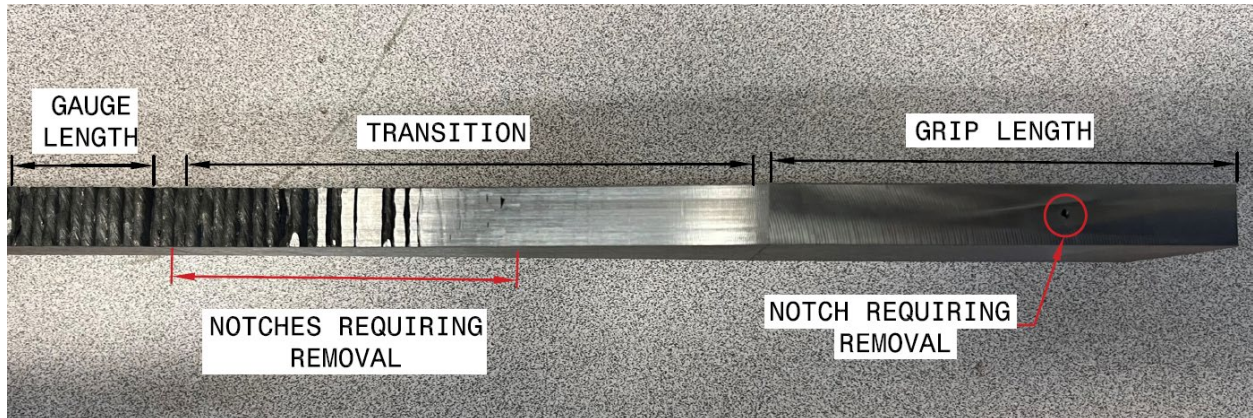
Source: FHWA.

**Figure 9. Schematic. Dimensions of Lo-M and Hi-M fatigue specimens.**

## As-built Surface Specimens

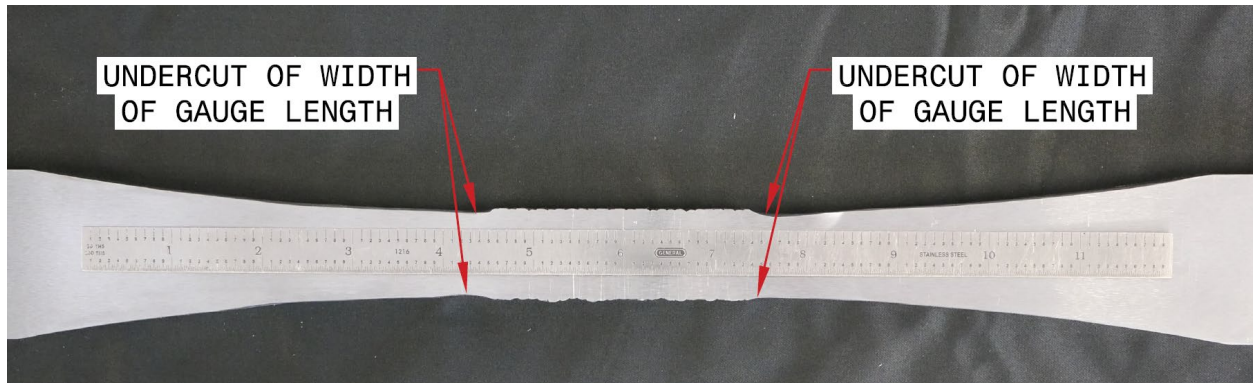
As-built (AB) surface finish fatigue specimens of  $\frac{1}{2}$  inch thickness were extracted from each near-net fatigue component. All other machined faces were ground to a surface finish of less than 40 microinches. The as-built surface finish was left on the  $\frac{1}{2}$  inch edges of each side of the gauge length for each specimen. The profile of each type of machined surface finish specimen was determined based on the geometry of the component received, leading to slightly different profiles for each type. After machining, the transition from the machined radius to the as-built gauge length of each specimen and grip length were hand finished to smooth any notches that were not removed during the machining (Figure 10). The hand finishing slightly undercut the gauge length (Figure 11).

Photographs of each finished specimen were taken and imported into a computer-aided design (CAD) program to measure each AB specimen's average width from peak-to-peak and valley-to-valley. Note that the valleys and peaks were not always directly across from each other, leading to some measurements not being perpendicular to the longitudinal axis of the specimen (Figure 12). Other dimensions of each specimen were measured to the nearest 0.001 inch, and the specimens were visually inspected for any apparent discontinuities. The specimen thickness and average valley-to-valley measurement for each specimen were used to determine the nominal area in the gauge length. Specimens are labeled in the following format "INTERPASS TEMP.-SURFACE FINISH-SAMPLE#." For example, specimen Hi-AB-6 is specimen number 6, taken from the high interpass near-net component with an as-built surface finish.



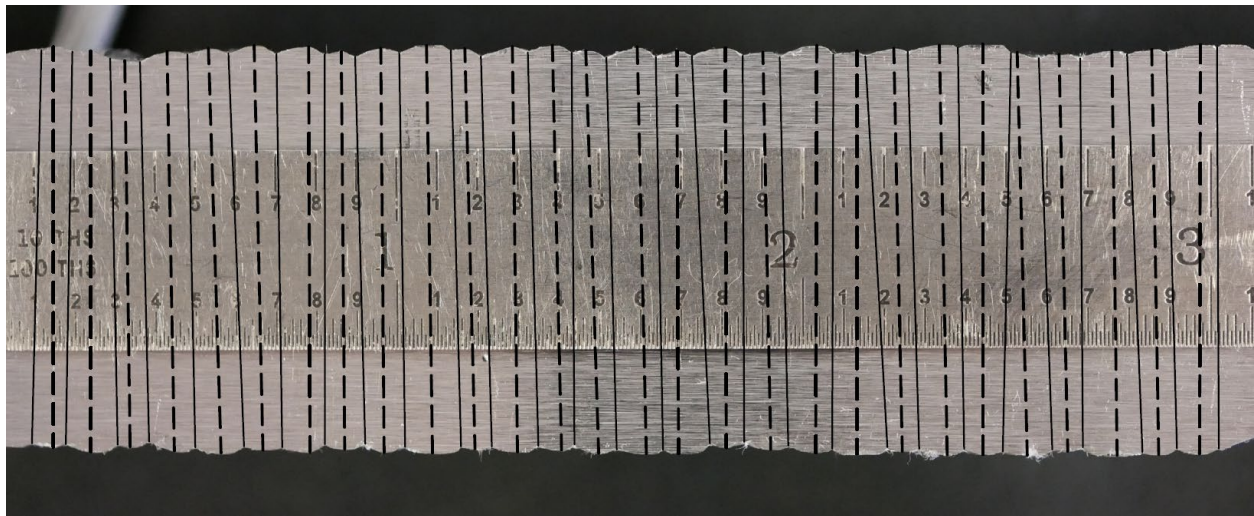
Source: FHWA.

**Figure 10. Photo. AB fatigue specimen prior to hand finishing to remove notches from the transition and grip lengths; notches requiring removal indicated.**



Source: FHWA.

**Figure 11. Photo. AB fatigue specimen after hand finishing to remove notches from the transition and grip lengths; typical undercut areas of gauge length width indicated.**



Source: FHWA.

**Figure 12. Photo. Peak-to-peak width (dashed lines) and valley-to-valley width (solid lines) of an AB specimen.**

## Procedure

Specimens were cyclically loaded in uniaxial tension in a 55-kip capacity UTM. Table 9 shows the number of specimens tested from each fatigue component at each stress range. Stress range cycles were applied in a sinusoidal waveform to the specimens at a rate of 15 Hz for all stress ranges except the 38 ksi stress range, which was applied at 12 Hz. Both cycle rates (12 Hz and 15 Hz) were within the recommended range of  $10^{-2}$  and  $10^2$  Hz from ASTM E466-21 to ensure that rate-dependent effects were not seen in the cycle counts for each specimen.

Prior to testing, strain gages were applied at the center of the width and gauge length of the machined specimens to verify that the correct stress range was achieved. At least 90 cycles were applied to the machined specimens, and the stress range recorded by the strain gage was compared to the desired stress range. Because the width of the gauge length of the as-built specimens was undercut, DIC was used to evaluate the strain field at the transition and the gage

length in addition to a strain gage. At least 90 cycles were applied to the as-built specimens, and no stress concentrations at the undercut area were noted.

**Table 9. Number of specimens tested from each component at each stress range.**

<b>Component ID</b>	<b>Stress Range, S<sub>r</sub> (ksi)</b>	<b>Number of Specimens Tested</b>
Lo-AB	12	1
Lo-AB	16	3
Lo-AB	20	3
Lo-M	30	2
Lo-M	38	2
Hi-AB	12	1
Hi-AB	16	3
Hi-AB	20	3
Hi-M	30	2
Hi-M	38	2

## CHAPTER 4: RESULTS AND DISCUSSION

### RESULTS

#### Tension Testing

The yield strength, tensile strength, percent elongation at fracture, and reduction of area were determined for each tensile specimen. The yield strength was determined using an offset of 0.2 percent per ASTM A370-22 Section 14.2.1. The tensile strength was determined as the largest stress achieved during testing per ASTM A370-22 Section 14.3. The percent elongation at fracture was determined using a virtual extensometer with an original gauge length of 2.0 inches per ASTM A370-22 Section 14.4.4.2. The reduction of area was determined by measuring the width and thickness of the cross section at the fracture location per ASTM A370-22 Section 14.5. The yield strength, tensile strength, percent elongation at fracture, and reduction of area for F70Lo, F70Hi, F80Lo, and F80Hi specimens are provided in Table 10 through Table 13, respectively. In addition, Figure 13 through Figure 16 plot the engineering stress-strain diagrams for all F70Lo, F70Hi, F80Lo, and F80Hi specimens, respectively. Figure 17 compares the engineering stress-strain diagrams for all four walls.

**Table 10. Tensile test results for F70Lo specimens.**

<b>Specimen ID</b>	<b>0.02 Percent Offset Yield Strength (ksi)</b>	<b>Tensile Strength (ksi)</b>	<b>Elongation at Fracture (Percent)</b>	<b>Reduction of Area (Percent)</b>
F70Lo-BD-1	54.4	72.1	35.0	68.7
F70Lo-BD-2	57.2	73.2	34.8	69.3
F70Lo-BD-3	57.5	73.6	36.1	67.0
<i>F70Lo-BD Average</i>	<i>56.4</i>	<i>73.0</i>	<i>35.3</i>	<i>68.4</i>
<i>F70Lo-BD Std. Dev.</i>	<i>1.4</i>	<i>0.6</i>	<i>0.6</i>	<i>1.0</i>
F70Lo-DD-1	59.7	74.5	40.0	70.3
F70Lo-DD-2	58.4	73.6	40.9	69.4
F70Lo-DD-3	58.3	73.6	41.9	72.9
<i>F70Lo-DD Average</i>	<i>58.8</i>	<i>73.9</i>	<i>40.9</i>	<i>70.8</i>
<i>F70Lo-DD Std. Dev.</i>	<i>0.6</i>	<i>0.4</i>	<i>0.8</i>	<i>1.5</i>
F70Lo-45-1	58.6	74.7	N/A*	69.2
F70Lo-45-2	59.7	74.1	31.7	71.3
F70Lo-45-3	58.8	74	32.9	67.6
<i>F70Lo-45 Average</i>	<i>59.0</i>	<i>74.3</i>	<i>32.3*</i>	<i>69.4</i>
<i>F70Lo-45 Std. Dev.</i>	<i>0.5</i>	<i>0.3</i>	<i>0.6*</i>	<i>1.5</i>
<b><i>Overall Average</i></b>	<b><i>58.1</i></b>	<b><i>73.7</i></b>	<b><i>36.7*</i></b>	<b><i>69.5</i></b>
<b><i>Overall Std. Dev.</i></b>	<b><i>1.5</i></b>	<b><i>0.7</i></b>	<b><i>3.6*</i></b>	<b><i>1.7</i></b>

\*Elongation at fracture of specimen F70Lo-45-1 is not reported because the specimen was tested on an unaligned UTM and DIC recording was terminated prior to fracture. The average and standard deviation were calculated without this elongation value.

**Table 11. Tensile test results for F70Hi specimens.**

<b>Specimen ID</b>	<b>0.02 Percent Offset Yield Strength (ksi)</b>	<b>Tensile Strength (ksi)</b>	<b>Elongation at Fracture (Percent)</b>	<b>Reduction of Area (Percent)</b>
F70Hi-BD-1	45.7	65.1	42.6	72.0
F70Hi-BD-2	45.9	65.0	45.2	72.5
F70Hi-BD-3	45.7	65.2	42.7	72.2
<i>F70Hi-BD Average</i>	<i>45.8</i>	<i>65.1</i>	<i>43.5</i>	<i>72.2</i>
<i>F70Hi-BD Std. Dev.</i>	<i>0.1</i>	<i>0.1</i>	<i>1.2</i>	<i>0.2</i>
F70Hi-DD-1	48.5	65.8	43.7	73.6
F70Hi-DD-2	47.2	65.4	43.3	70.9
F70Hi-DD-3	48.7	67.1	48.5	73.1
<i>F70Hi-DD Average</i>	<i>48.1</i>	<i>66.1</i>	<i>45.1</i>	<i>72.5</i>
<i>F70Hi-DD Std. Dev.</i>	<i>0.6</i>	<i>0.7</i>	<i>2.4</i>	<i>1.2</i>
F70Hi-45-1	46.3	65.2	27.7	73.5
F70Hi-45-2	46.4	65.2	41.6	72.8
F70Hi-45-3	46.7	65.3	45.2	71.9
<i>F70Hi-45 Average</i>	<i>46.4</i>	<i>65.2</i>	<i>38.2</i>	<i>72.7</i>
<i>F70Hi-45 Std. Dev.</i>	<i>0.2</i>	<i>0.0</i>	<i>7.6</i>	<i>0.6</i>
<b><i>Overall Average</i></b>	<b><i>46.8</i></b>	<b><i>65.5</i></b>	<b><i>42.3</i></b>	<b><i>72.5</i></b>
<b><i>Overall Std. Dev.</i></b>	<b><i>1.1</i></b>	<b><i>0.6</i></b>	<b><i>5.5</i></b>	<b><i>0.8</i></b>

**Table 12. Tensile test results for F80Lo specimens.**

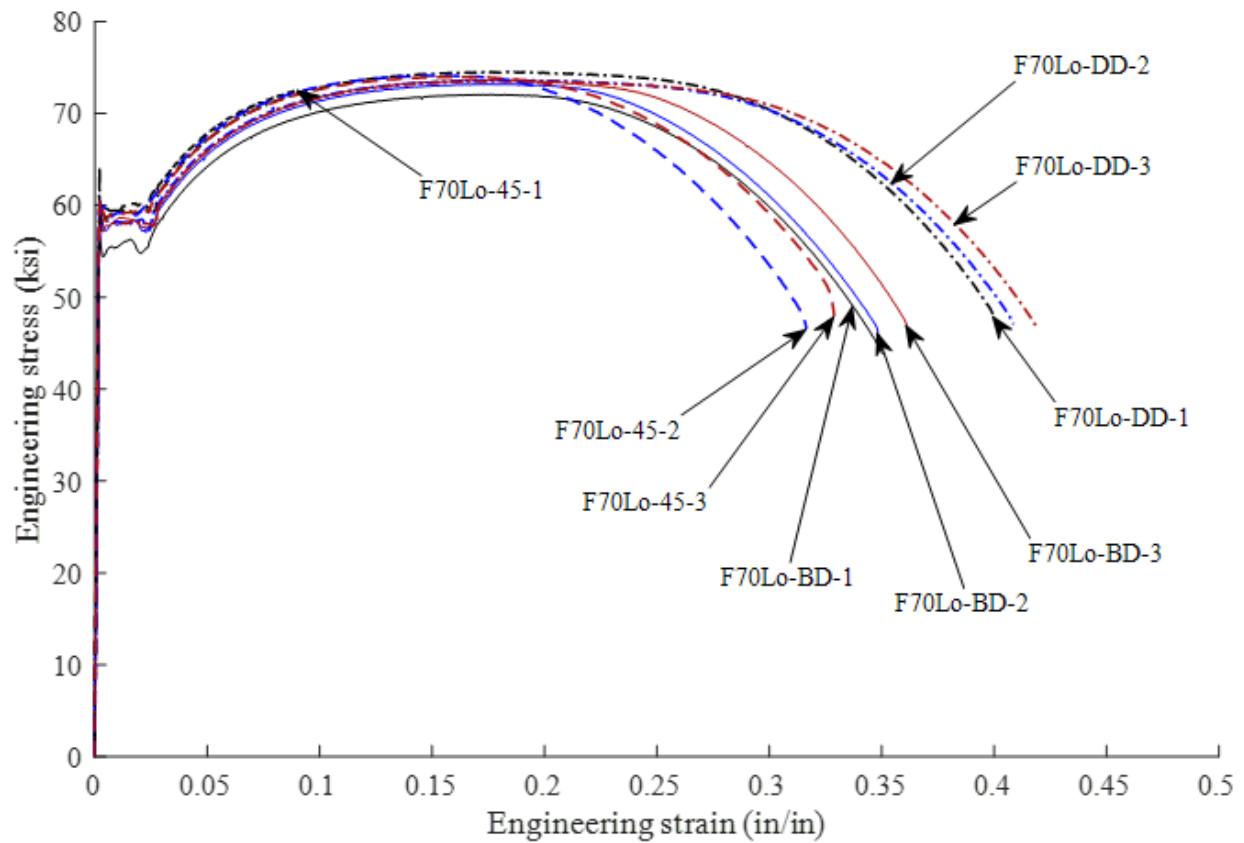
<b>Specimen ID</b>	<b>0.02 Percent Offset Yield Strength (ksi)</b>	<b>Tensile Strength (ksi)</b>	<b>Elongation at Fracture (Percent)</b>	<b>Reduction of Area Percent)</b>
F80Lo-BD-1	57.7	76.5	33.9	64.7
F80Lo-BD-2	59.2	77.2	33.4	69.7
F80Lo-BD-3	60.4	77.4	33.2	66.0
<i>F80Lo-BD Average</i>	<i>59.1</i>	<i>77.1</i>	<i>33.5</i>	<i>66.8</i>
<i>F80Lo-BD Std. Dev.</i>	<i>1.1</i>	<i>0.4</i>	<i>0.3</i>	<i>2.1</i>
F80Lo-DD-3	60.7	76.8	36.9	71.4
F80Lo-DD-4	62.7	78.9	40.7	67.9
<i>F80Lo-DD Average</i>	<i>61.7</i>	<i>77.9</i>	<i>38.8</i>	<i>69.7</i>
<i>F80Lo-DD Std. Dev.</i>	<i>1.0</i>	<i>1.0</i>	<i>1.9</i>	<i>1.8</i>
F80Lo-45-1	61.1	78.0	31.4	71.0
F80Lo-45-2	61.4	77.7	33.6	68.1
F80Lo-45-3	61.2	77.8	23.2	69.0
<i>F80Lo-45 Average</i>	<i>61.2</i>	<i>77.8</i>	<i>29.4</i>	<i>69.3</i>
<i>F80Lo-45 Std. Dev.</i>	<i>0.1</i>	<i>0.1</i>	<i>4.4</i>	<i>1.2</i>
<b><i>Overall Average</i></b>	<b><i>60.2</i></b>	<b><i>77.3</i></b>	<b><i>32.2</i></b>	<b><i>68.5</i></b>
<b><i>Overall Std. Dev.</i></b>	<b><i>1.2</i></b>	<b><i>0.5</i></b>	<b><i>4.0</i></b>	<b><i>2.3</i></b>

**Table 13. Tensile test results for F80Hi specimens.**

<b>Specimen ID</b>	<b>0.02 Percent Offset Yield Strength (ksi)</b>	<b>Tensile Strength (ksi)</b>	<b>Elongation at Fracture (Percent)</b>	<b>Reduction of Area (Percent)</b>
F80Hi-BD-1	53.0	71.2	39.7	68.9
F80Hi-BD-2	50.9	71.0	39.6	72.0
F80Hi-BD-3	51.2	71.2	40.2	68.4
<i>F80Hi-BD Average</i>	<i>51.7</i>	<i>71.1</i>	<i>39.8</i>	<i>69.8</i>
<i>F80Hi-BD Std. Dev.</i>	<i>0.9</i>	<i>0.1</i>	<i>0.2</i>	<i>1.6</i>
F80Hi-DD-1	54.8	72.3	42.8	69.4
F80Hi-DD-2	51.7	70.6	30.1*	50.6
F80Hi-DD-3	51.6	70.5	42.1	70.1
<i>F80Hi-DD Average</i>	<i>52.7</i>	<i>71.1</i>	<i>42.5*</i>	<i>63.4</i>
<i>F80Hi-DD Std. Dev.</i>	<i>1.5</i>	<i>0.8</i>	<i>0.3*</i>	<i>9.0</i>
F80Hi-45-1	52.1	70.6	41.4	69.2
F80Hi-45-2	50.7	71.3 <sup>s</sup>	38.5 <sup>s</sup>	67.4
F80Hi-45-3	51.4	71.1	35.8	70.4
<i>F80Hi-45 Average</i>	<i>51.4</i>	<i>71.0</i>	<i>38.6</i>	<i>69.0</i>
<i>F80Hi-45 Std. Dev.</i>	<i>0.6</i>	<i>0.3</i>	<i>2.3</i>	<i>1.2</i>
<b><i>Overall Average</i></b>	<b><i>51.9</i></b>	<b><i>71.1</i></b>	<b><i>40.0*</i></b>	<b><i>67.4</i></b>
<b><i>Overall Std. Dev.</i></b>	<b><i>1.2</i></b>	<b><i>0.5</i></b>	<b><i>2.1*</i></b>	<b><i>6.0</i></b>

\*The average and standard deviation do not include the elongation at fracture of specimen F80Hi-DD-2, which had an internal discontinuity in its gauge length.

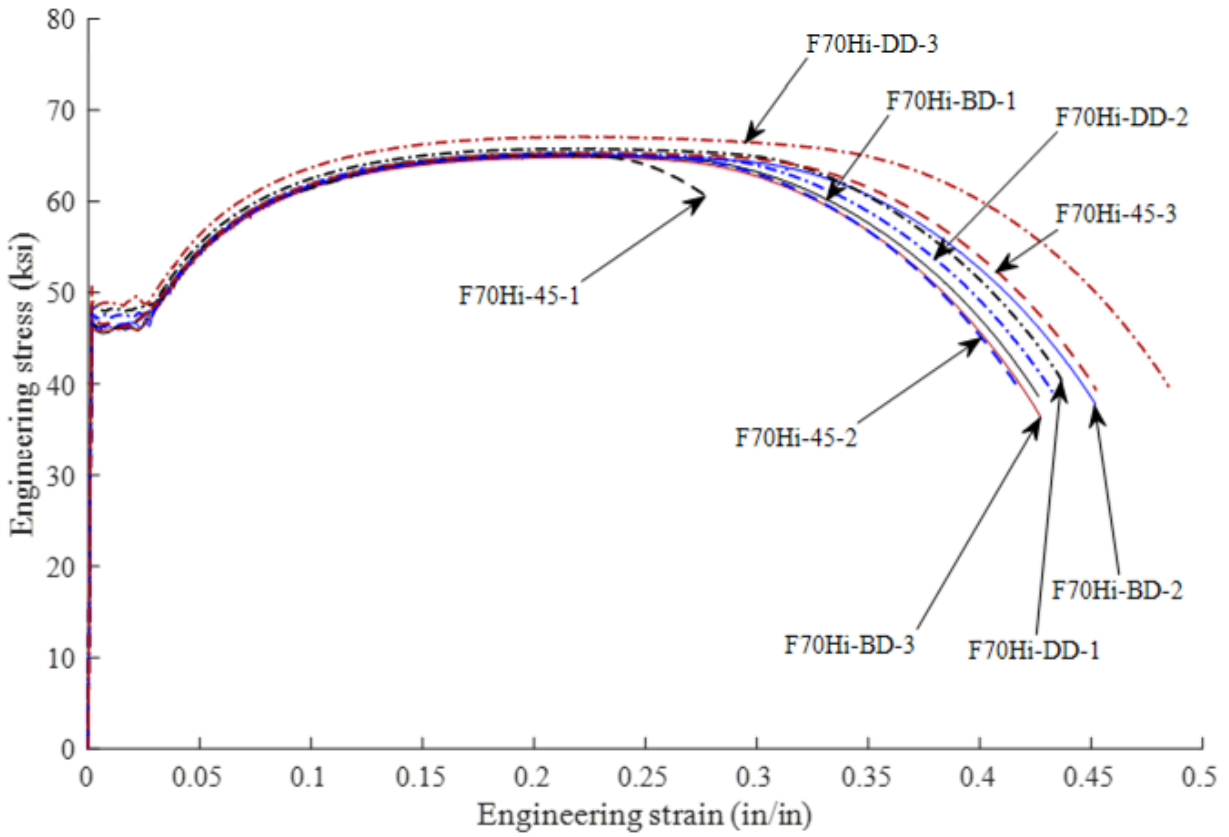
<sup>s</sup>DIC data recording was terminated prior to fracture. The tensile strength was determined from UTM data and elongation at fracture was determined from measuring the fractured specimen.



Source: FHWA.

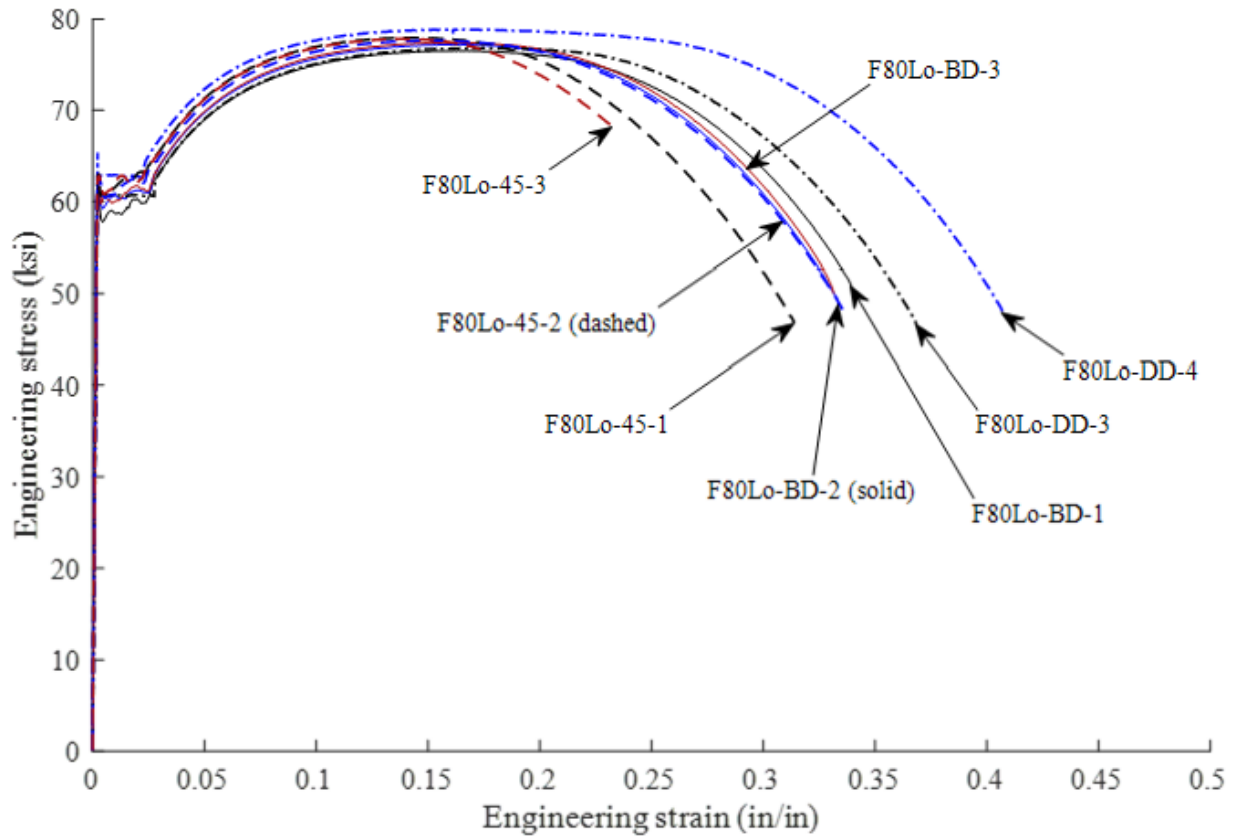
Note 1: Arrow points to where the DIC recording of the test of F70Lo-45-1 was terminated early, not visible due to the overlay of data at the point of termination. This specimen was tested on an unaligned UTM and censored from statistical calculations. Data shown for information purposes only.

**Figure 13. Graph. Engineering stress-strain for F70Lo specimens.**



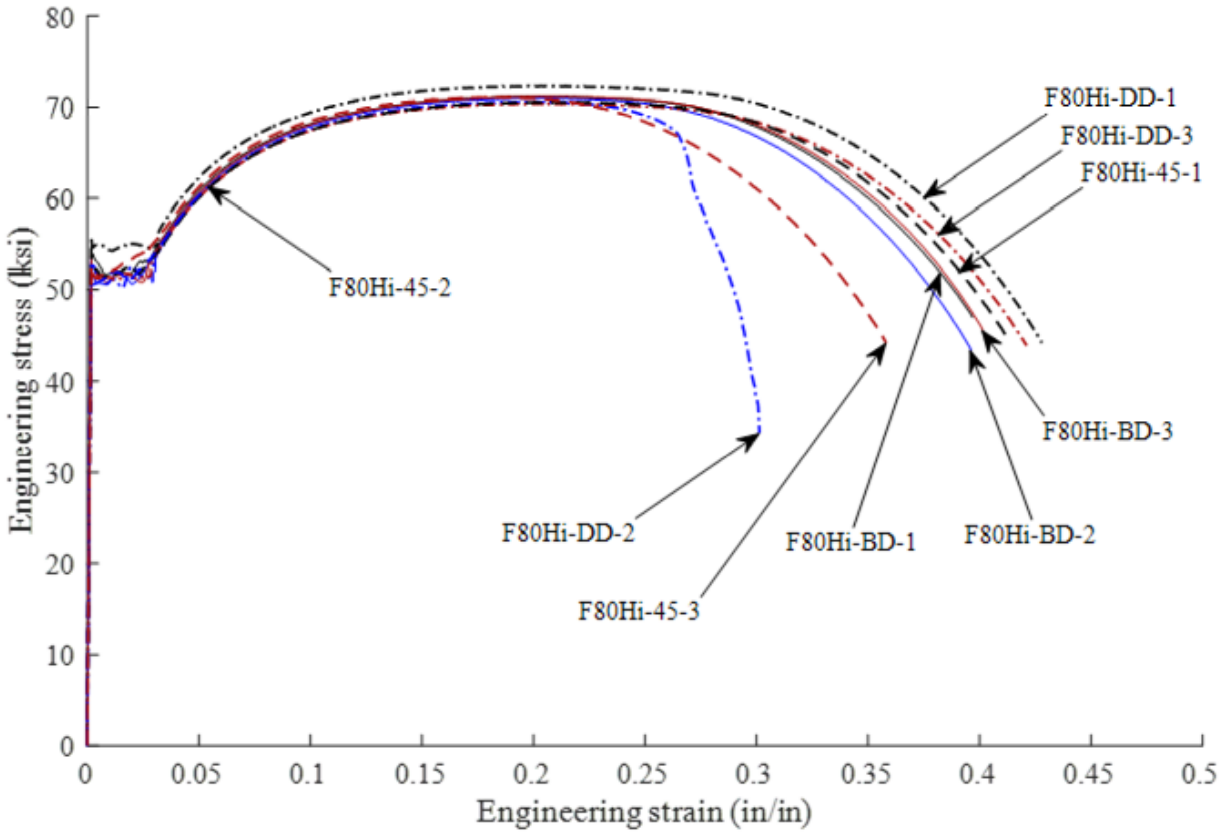
Source: FHWA.

**Figure 14. Graph. Engineering stress-strain for F70Hi specimens.**



Source: FHWA.

**Figure 15. Graph. Engineering stress-strain for F80Lo specimens.**

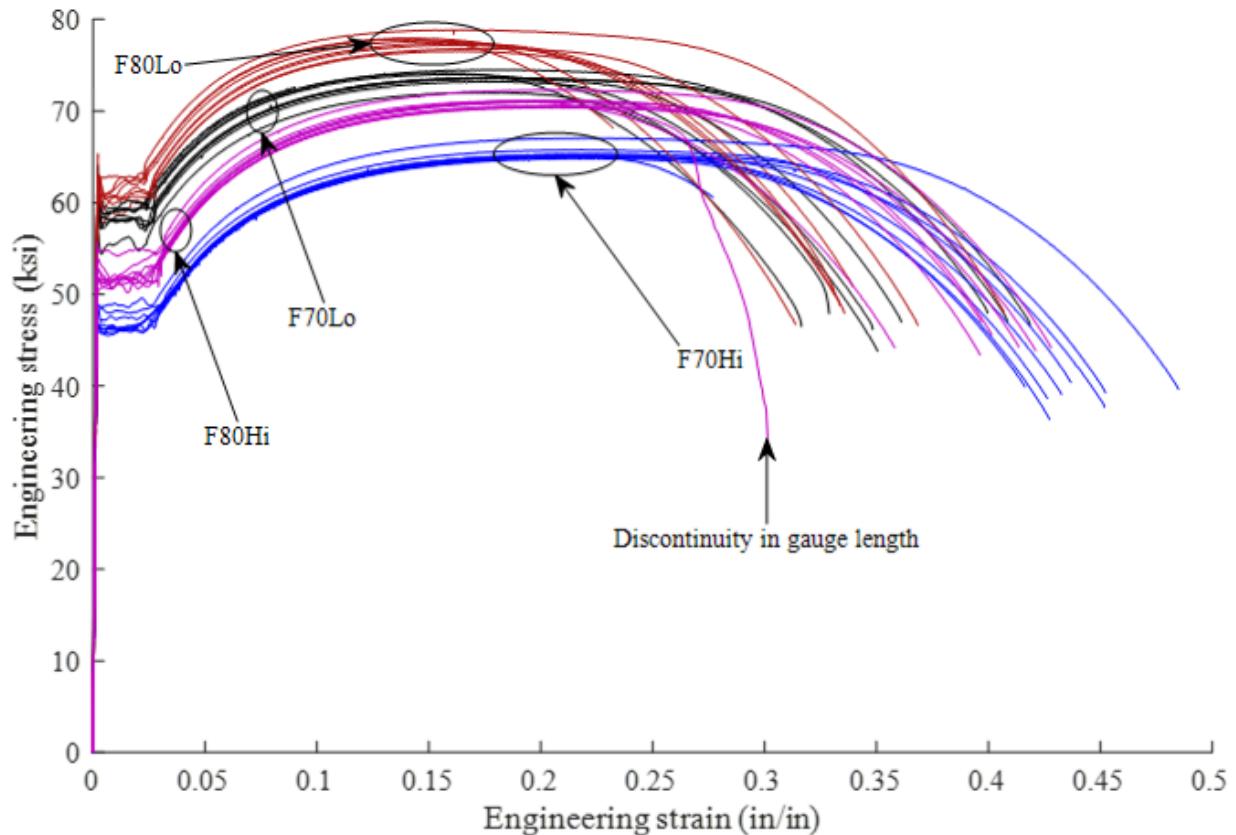


Source: FHWA.

Note 1: Arrow points to where the DIC recording of the test of F80Hi-45-2 was terminated early, not visible due to the overlay of data at the point of termination.

Note 2: F80HI-DD-2 has a discontinuity in its gauge length.

**Figure 16. Graph. Engineering stress-strain diagrams for F80Hi specimens.**



Source: FHWA.

**Figure 17. Graph. Engineering stress-strain diagrams for all specimens.**

### Impact Testing (Charpy V-Notch)

Table 14 and Table 15 show the tested temperatures and the corresponding absorbed energies for the  $\frac{1}{2} T$  and  $\frac{1}{4} T$  specimens, respectively, from wall F70Lo. Table 16 and Table 17 show the tested temperatures and the corresponding absorbed energies for the  $\frac{1}{2} T$  and  $\frac{1}{4} T$  specimens, respectively, from wall F70Hi. Table 18 and Table 19 show the tested temperatures and the corresponding absorbed energies for the  $\frac{1}{2} T$  and  $\frac{1}{4} T$  specimens, respectively, from wall F80Lo. Table 20 and Table 21 show the tested temperatures and the corresponding absorbed energies for the  $\frac{1}{2} T$  and  $\frac{1}{4} T$  specimens, respectively, from wall F80Hi. As previously stated, all specimens were evaluated using a go-no-go gauge to ensure compliance with ASTM A370-22. During the evaluation, several specimens outside of geometric tolerance were identified and notated in the footnotes of Table 14 through Table 21. Measured values from the specimens outside of the standard were censored from the data analysis; however, the data was reported in the tables for informational purposes.

**Table 14. Impact energy results for  $1/2 T$  F70Lo specimens.**

Specimen ID	Temperature (°F)	Impact Energy (ft-lbf)	Specimen ID	Temperature (°F)	Impact Energy (ft-lbf)
F70Lo-BD-05	-110	28.3	F70Lo-DD-05	-110	81.9
F70Lo-BD-15	-110	28.3	F70Lo-DD-14	-110	6.6
F70Lo-BD-23	-110	16.7	F70Lo-DD-24	-110	53.6
F70Lo-BD-32	-110	21.5	F70Lo-DD-35	-110	35.1
F70Lo-BD-03	-90	24.5	F70Lo-DD-03	-90	6.2
F70Lo-BD-09	-90	33.5	F70Lo-DD-09	-90	42.5
F70Lo-BD-21	-90	32.6	F70Lo-DD-22	-90	71.8
F70Lo-BD-27	-90	57.5	F70Lo-DD-33	-90	35.4
F70Lo-BD-02	-60	55.4	F70Lo-DD-02	-60	42.7
F70Lo-BD-08	-60	49.1	F70Lo-DD-08	-60	36.3
F70Lo-BD-20	-60	58.5	F70Lo-DD-21	-60	68.1
F70Lo-BD-26	-60	15.0	F70Lo-DD-28	-60	51.6
F70Lo-BD-01	-30	99.6	F70Lo-DD-01	-30	65.3
F70Lo-BD-07	-30	45.8	F70Lo-DD-07	-30	99.6
F70Lo-BD-19	-30	40.0	F70Lo-DD-20	-30	113.1
F70Lo-BD-25	-30	85.8	F70Lo-DD-27	-30	38.1
F70Lo-BD-04	10	68.1	F70Lo-DD-04	10	149.4
F70Lo-BD-10	10	70.4	F70Lo-DD-10	10	127.1
F70Lo-BD-22	10	101.4	F70Lo-DD-23	10	183.0
F70Lo-BD-28	10	82.6	F70Lo-DD-34	10	102.7
F70Lo-BD-06	40	104.4	F70Lo-DD-06	40	188.3
F70Lo-BD-16	40	88.7	F70Lo-DD-15	40	100.5
F70Lo-BD-24	40	122.0	F70Lo-DD-26	40	134.5
F70Lo-BD-33	40	96.7	F70Lo-DD-36	40	189.2
F70Lo-BD-17	70	145.6	F70Lo-DD-16	70	182.1
F70Lo-BD-18	70	144.7	F70Lo-DD-17	70	134.8
F70Lo-BD-34	70	126.3	F70Lo-DD-19*	70	247.3*
F70Lo-BD-35	70	169.2	F70Lo-DD-25*	70	178.0*
			F70Lo-DD-32	70	160.3

\*Notch depth slightly too deep

**Table 15. Impact energy results for  $1/4 T$  F70Lo specimens.**

Specimen ID	Temperature (°F)	Impact Energy (ft-lbf)	Specimen ID	Temperature (°F)	Impact Energy (ft-lbf)
F70Lo-BD-11	-30	32.8	F70Lo-DD-11	-30	94.0
F70Lo-BD-12	-30	37.8	F70Lo-DD-12	-30	109.6
F70Lo-BD-29	-30	80.0	F70Lo-DD-13	-30	85.0
F70Lo-BD-30	-30	42.0	F70Lo-DD-29	-30	76.1
F70Lo-BD-31	-30	59.4	F70Lo-DD-30	-30	97.0
			F70Lo-DD-31	-30	85.3

**Table 16. Impact energy results for 1/2 TF70Hi specimens.**

Specimen ID	Temperature (°F)	Impact Energy (ft-lbf)	Specimen ID	Temperature (°F)	Impact Energy (ft-lbf)
F70Hi-BD-05	-110	20.3	F70Hi-DD-05	-110	58.6
F70Hi-BD-15	-110	60.2	F70Hi-DD-14	-110	60.4
F70Hi-BD-23	-110	31.3	F70Hi-DD-23	-110	48.6
F70Hi-BD-34	-110	44.4	F70Hi-DD-33*	-110	83.6*
F70Hi-BD-03	-90	66.3	F70Hi-DD-03	-90	28.3
F70Hi-BD-10	-90	68.3	F70Hi-DD-09	-90	92.0
F70Hi-BD-21	-90	18.9	F70Hi-DD-21	-90	42.7
F70Hi-BD-28	-90	29.5	F70Hi-DD-28	-90	84.1
F70Hi-BD-02	-60	51.9	F70Hi-DD-02	-60	44.4
F70Hi-BD-08	-60	111.8	F70Hi-DD-08*	-60	169.1*
F70Hi-BD-26	-60	32.3	F70Hi-DD-18	-60	237.4
F70Hi-BD-36	-60	103.1	F70Hi-DD-20	-60	119.6
F70Hi-BD-01	-30	111.4	F70Hi-DD-26	-60	203.3
F70Hi-BD-07	-30	44.6	F70Hi-DD-01	-30	155.0
F70Hi-BD-25	-30	64.7	F70Hi-DD-07	-30	211.5
F70Hi-BD-35	-30	68.6	F70Hi-DD-19	-30	215.7
F70Hi-BD-04	10	218.0	F70Hi-DD-25	-30	189.3
F70Hi-BD-14*	10	221.0*	F70Hi-DD-04	10	265.1
F70Hi-BD-17	10	157.4	F70Hi-DD-10	10	261.3
F70Hi-BD-19	10	215.0	F70Hi-DD-22	10	262.8
F70Hi-BD-22	10	237.2	F70Hi-DD-32	10	268.6
F70Hi-BD-06	40	256.8	F70Hi-DD-06	40	266.4
F70Hi-BD-16	40	192.9	F70Hi-DD-15	40	262.7
F70Hi-BD-24	40	208.5	F70Hi-DD-24	40	270.2
F70Hi-BD-33	40	122.1	F70Hi-DD-34	40	262.2
F70Hi-BD-09*	70	259.1*	F70Hi-DD-16	70	260.9
F70Hi-BD-18	70	257.6	F70Hi-DD-17	70	261.1
F70Hi-BD-20	70	268.2	F70Hi-DD-27*	70	259.8*
F70Hi-BD-27	70	258.3	F70Hi-DD-35*	70	262.5*
			F70Hi-DD-36	70	261.9

\*Notch slightly too deep

\*Notch slightly too deep

**Table 17. Impact energy results for 1/4 TF70Hi specimens.**

Specimen ID	Temperature (°F)	Impact Energy (ft-lbf)	Specimen ID	Temperature (°F)	Impact Energy (ft-lbf)
F70Hi-BD-11	-30	75.8	F70Hi-DD-11	-30	107.4
F70Hi-BD-12	-30	98.9	F70Hi-DD-12	-30	206.2
F70Hi-BD-13	-30	100.7	F70Hi-DD-13	-30	238.5
F70Hi-BD-29	-30	138.8	F70Hi-DD-29	-30	237.0
F70Hi-BD-30	-30	119.5	F70Hi-DD-30	-30	110.2
F70Hi-BD-31*	-30	87.3*	F70Hi-DD-31	-30	211.5

\*Notch slightly too deep

**Table 18. Impact energy results for  $1/2 T$  F80Lo specimens.**

Specimen ID	Temperature (°F)	Impact Energy (ft-lbf)	Specimen ID	Temperature (°F)	Impact Energy (ft-lbf)
F80Lo-BD-07	-110	43.2	F80Lo-DD-05	-110	7.0
F80Lo-BD-17	-110	39.6	F80Lo-DD-15	-110	59.5
F80Lo-BD-23	-110	40.6	F80Lo-DD-28	-110	58.4
F80Lo-BD-33	-110	28.1	F80Lo-DD-34	-110	49.5
F80Lo-BD-03	-90	60.8	F80Lo-DD-03	-90	60.3
F80Lo-BD-15	-90	59.9	F80Lo-DD-09	-90	54.6
F80Lo-BD-21	-90	69.8	F80Lo-DD-23	-90	70.9
F80Lo-BD-27	-90	94.5	F80Lo-DD-27	-90	76.0
F80Lo-BD-02	-60	103.8	F80Lo-DD-02	-60	51.1
F80Lo-BD-14	-60	127.1	F80Lo-DD-08	-60	85.6
F80Lo-BD-20	-60	63.6	F80Lo-DD-20	-60	105.4
F80Lo-BD-26	-60	64.6	F80Lo-DD-26	-60	87.5
F80Lo-BD-01	-30	118.8	F80Lo-DD-01	-30	117.0
F80Lo-BD-09	-30	124.4	F80Lo-DD-07	-30	112.3
F80Lo-BD-19	-30	113.2	F80Lo-DD-19	-30	130.6
F80Lo-BD-25	-30	86.4	F80Lo-DD-25	-30	84.7
F80Lo-BD-04	10	187.5	F80Lo-DD-04	10	181.3
F80Lo-BD-16	10	147.4	F80Lo-DD-10	10	170.0
F80Lo-BD-22	10	179.9	F80Lo-DD-24	10	180.5
F80Lo-BD-28	10	146.0	F80Lo-DD-32*	10	181.4*
F80Lo-BD-08	40	190.8	F80Lo-DD-36	10	174.2
F80Lo-BD-18	40	169.3	F80Lo-DD-06	40	150.6
F80Lo-BD-24	40	188.7	F80Lo-DD-16	40	171.4
F80Lo-BD-34	40	184.9	F80Lo-DD-33	40	189.9
F80Lo-BD-05*	70	190.6*	F80Lo-DD-35	40	192.6
F80Lo-BD-10*	70	203.1*	F80Lo-DD-14	70	187.8
F80Lo-BD-35	70	232.7	F80Lo-DD-17	70	190.8
F80Lo-BD-36	70	245.0	F80Lo-DD-18	70	169.1
*Notch slightly too deep			F80Lo-DD-21*	70	178.6*
			F80Lo-DD-22*	70	228.4*

\*Notch slightly too deep

**Table 19. Impact energy results for  $1/4 T$  F80Lo specimens.**

Specimen ID	Temperature (°F)	Impact Energy (ft-lbf)	Specimen ID	Temperature (°F)	Impact Energy (ft-lbf)
F80Lo-BD-11	-30	102.2	F80Lo-DD-11	-30	106.2
F80Lo-BD-12	-30	105.9	F80Lo-DD-12	-30	100.1
F80Lo-BD-13	-30	92.5	F80Lo-DD-13	-30	113.1
F80Lo-BD-29	-30	112.6	F80Lo-DD-29	-30	105.9
F80Lo-BD-30	-30	87.1	F80Lo-DD-30	-30	106.1
F80Lo-BD-31	-30	107.9	F80Lo-DD-31	-30	104.1

**Table 20. Impact energy results for  $1/2 T$  F80Hi specimens.**

Specimen ID	Temperature (°F)	Impact Energy (ft-lbf)	Specimen ID	Temperature (°F)	Impact Energy (ft-lbf)
F80Hi-BD-16	-110	67.7	F80Hi-DD-06	-110	84.4
F80Hi-BD-27*	-110	25.7*	F80Hi-DD-15	-110	29.4
F80Hi-BD-33	-110	71.6	F80Hi-DD-24	-110	63.8
F80Hi-BD-03	-90	52.0	F80Hi-DD-32	-110	66.8
F80Hi-BD-14	-90	27.9	F80Hi-DD-03	-90	109.7
F80Hi-BD-21	-90	37.4	F80Hi-DD-10	-90	74.3
F80Hi-BD-28	-90	52.8	F80Hi-DD-22	-90	99.7
F80Hi-BD-02	-60	93.2	F80Hi-DD-27	-90	40.9
F80Hi-BD-10	-60	123.5	F80Hi-DD-02	-60	111.3
F80Hi-BD-20	-60	56.5	F80Hi-DD-09	-60	118.3
F80Hi-BD-26	-60	116.0	F80Hi-DD-21	-60	146.9
F80Hi-BD-09	-30	75.1	F80Hi-DD-26	-60	122.7
F80Hi-BD-19	-30	120.3	F80Hi-DD-01	-30	126.5
F80Hi-BD-25	-30	87.0	F80Hi-DD-08	-30	117.4
F80Hi-BD-01*	10	143.2*	F80Hi-DD-19	-30	179.7
F80Hi-BD-15	10	115.1	F80Hi-DD-25	-30	159.6
F80Hi-BD-32	10	176.8	F80Hi-DD-04	10	186.5
F80Hi-BD-05^	40	183.2^	F80Hi-DD-14	10	188.8
F80Hi-BD-07	40	182.2	F80Hi-DD-23	10	196.6
F80Hi-BD-35	40	235.2	F80Hi-DD-28	10	187.3
F80Hi-BD-08^	70	178.1^	F80Hi-DD-16	40	211.9
F80Hi-BD-17	70	213.2	F80Hi-DD-17	40	224.4
F80Hi-BD-36	70	195.9	F80Hi-DD-33	40	261.4
			F80Hi-DD-35	40	240.6
			F80Hi-DD-07*	70	214.9*
			F80Hi-DD-18	70	202.2
			F80Hi-DD-20*	70	258.8*
			F80Hi-DD-34	70	264.1

\*Notch slightly too deep  
^Large hole from discontinuity

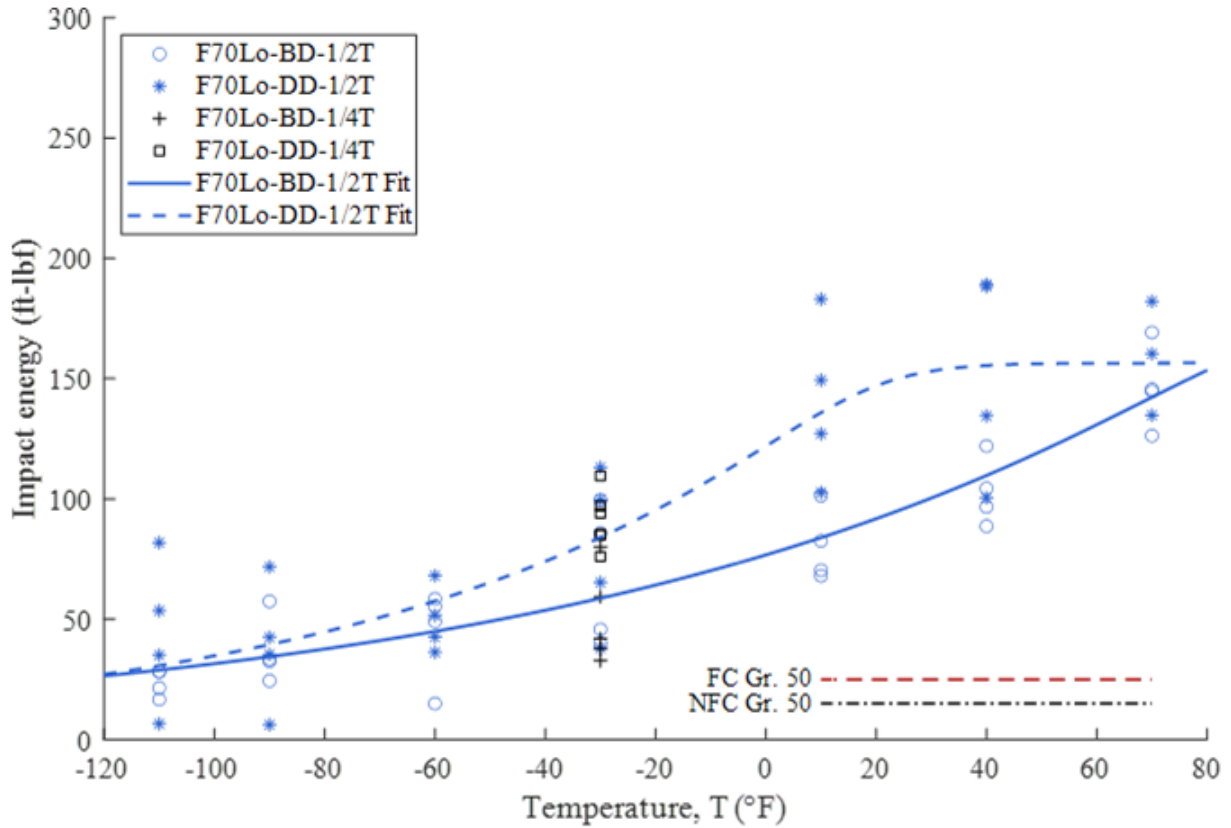
\*Notch slightly too deep

**Table 21. Impact energy results for  $1/4 T$  F80Hi specimens.**

Specimen ID	Temperature (°F)	Impact Energy (ft-lbf)	Specimen ID	Temperature (°F)	Impact Energy (ft-lbf)
F80Hi-BD-11	-30	148.4	F80Hi-DD-11	-30	121.2
F80Hi-BD-12	-30	102.7	F80Hi-DD-12	-30	116.3
F80Hi-BD-13	-30	138.1	F80Hi-DD-13*	-30	119.3*
F80Hi-BD-29	-30	141.5	F80Hi-DD-29	-30	201.3
F80Hi-BD-30	-30	136.8	F80Hi-DD-30	-30	135.3
F80Hi-BD-31*	-30	147.8*	F80Hi-DD-31	-30	126.9

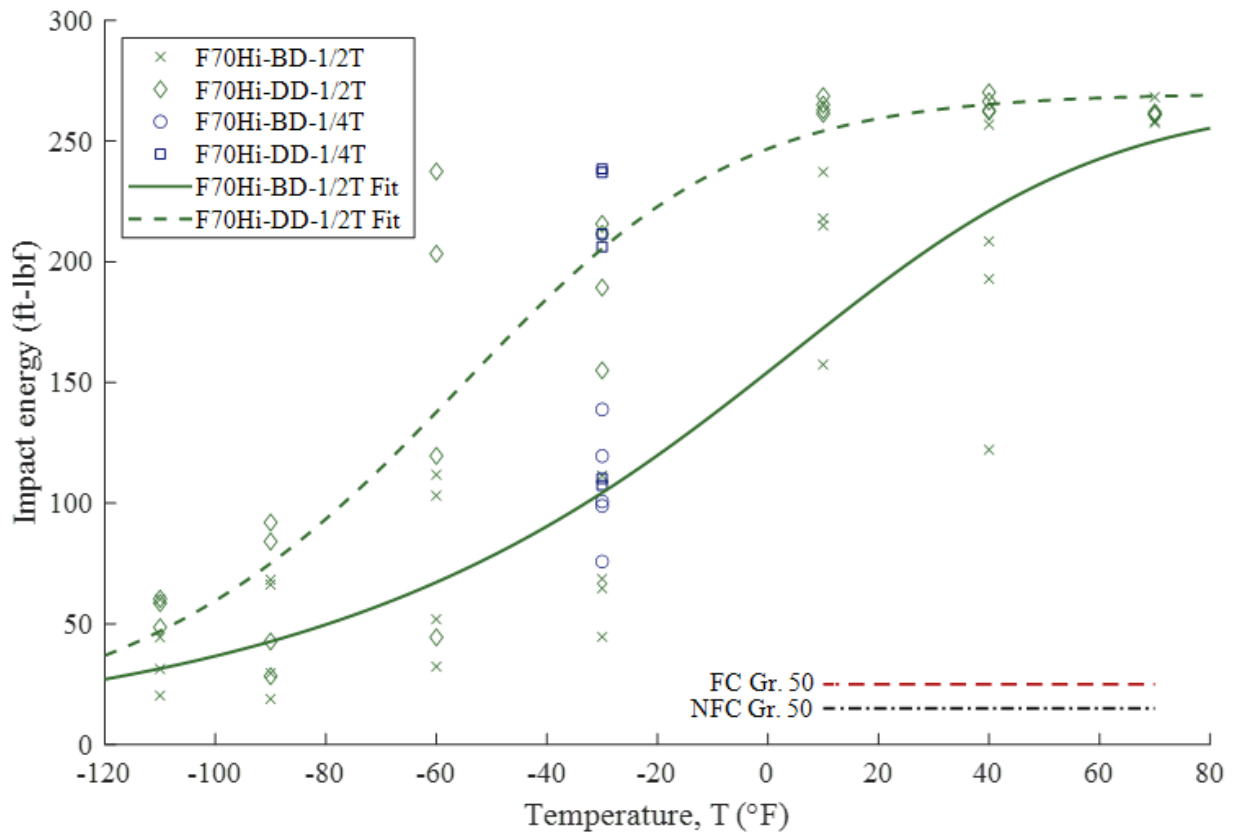
\*One end undersized, 0.384 inches.      \*One end undersized, 0.378 inches.

Figure 18 through Figure 21 plot the temperature versus impact energy for walls F70Lo, F70Hi, F80Lo, and F80Hi, respectively. Both  $1/2 T$  and  $1/4 T$  data are included for each wall. Five parameter sigmoid functions were also generated for the BD and DD  $1/2 T$  specimens for each wall using Yount et al.'s procedure [99]. The upper shelf of the sigmoid functions was set as 105 percent of the maximum impact energy value from each dataset and the lower shelf is forced to be positive, but minimal. Finally, all three minimum service temperatures are included from the AASHTO Table C6.6.2.1-1 requirements for Grade 50 non-fracture critical (NFC) and fracture critical (FC). All specimens tested exceed the AASHTO specifications.



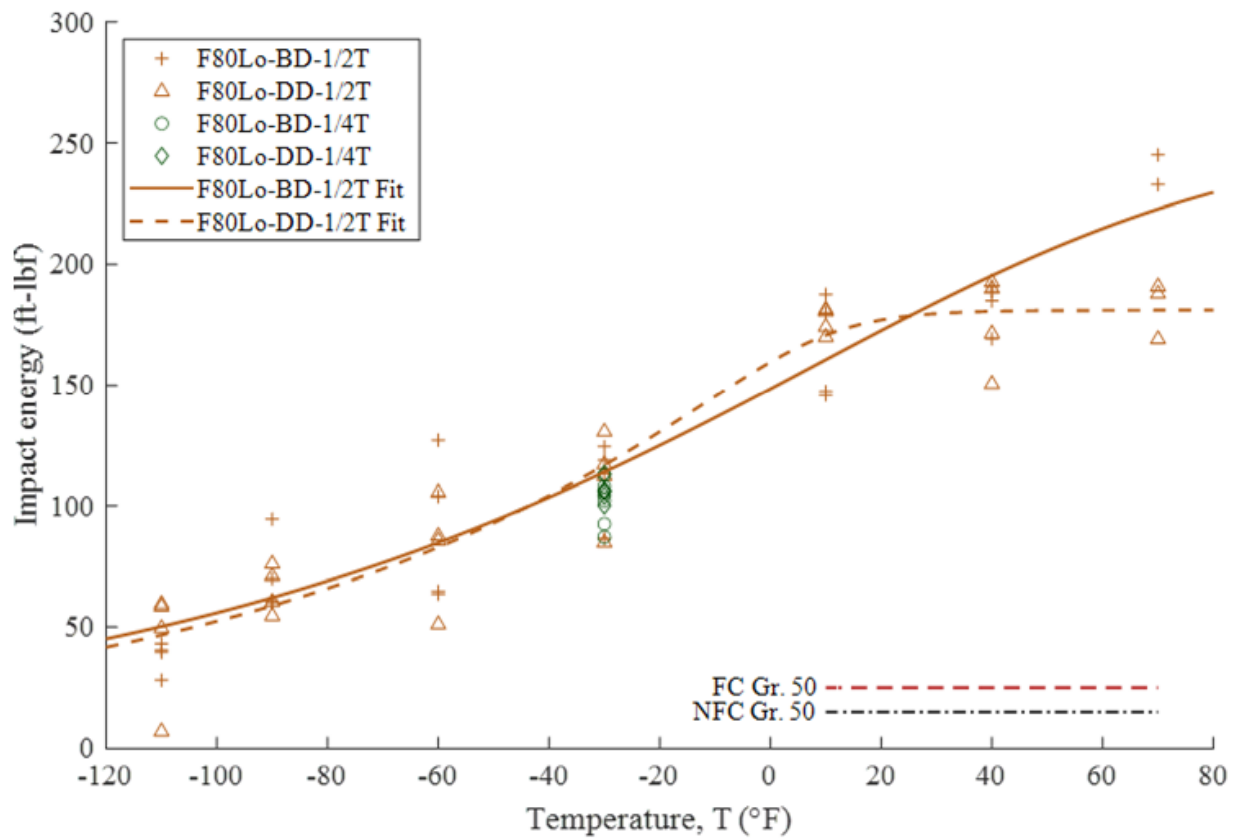
Source: FHWA.

**Figure 18. Graph. Temperature versus impact energy for all F70Lo specimens.**



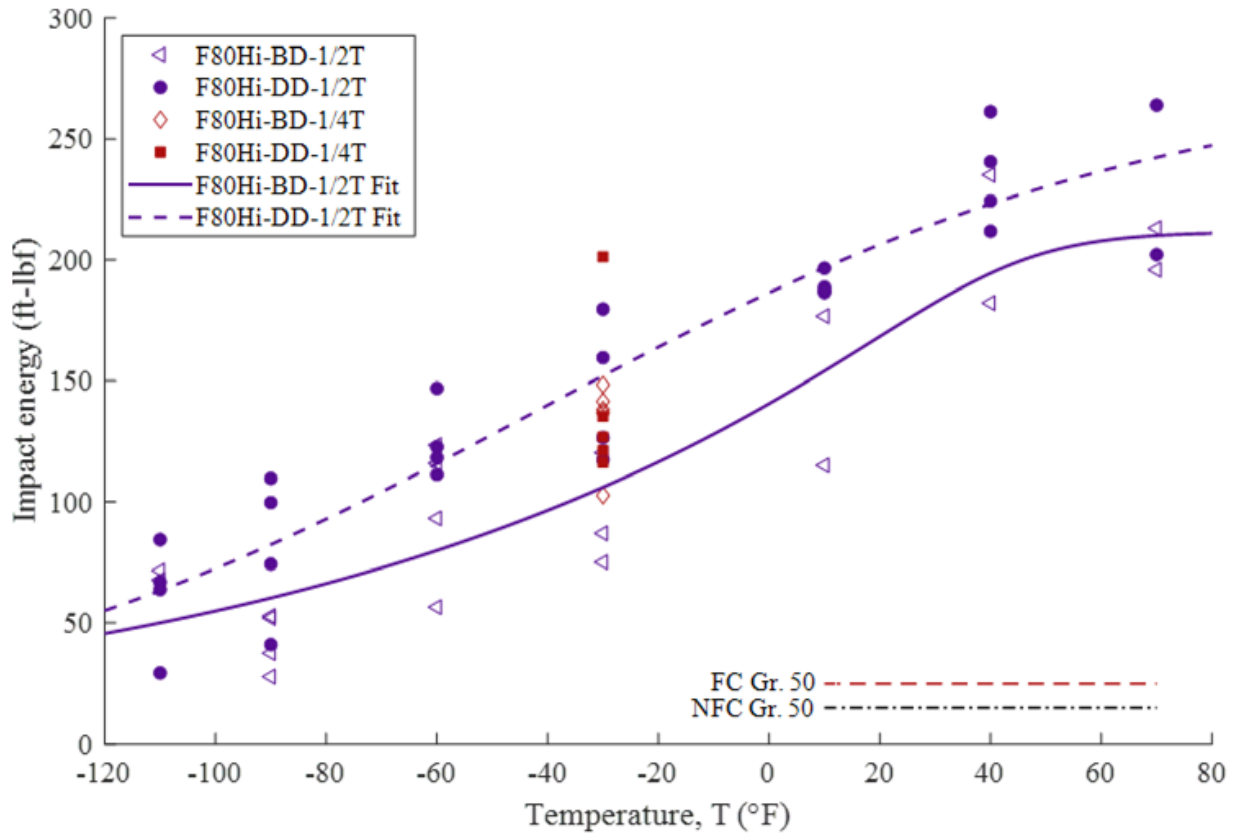
Source: FHWA.

**Figure 19. Graph. Temperature versus impact energy for all F70Hi specimens.**



Source: FHWA.

**Figure 20. Graph. Temperature versus impact energy for all F80Lo specimens.**



Source: FHWA.

**Figure 21. Graph. Temperature versus impact energy for all F80Hi specimens.**

### Fatigue Testing

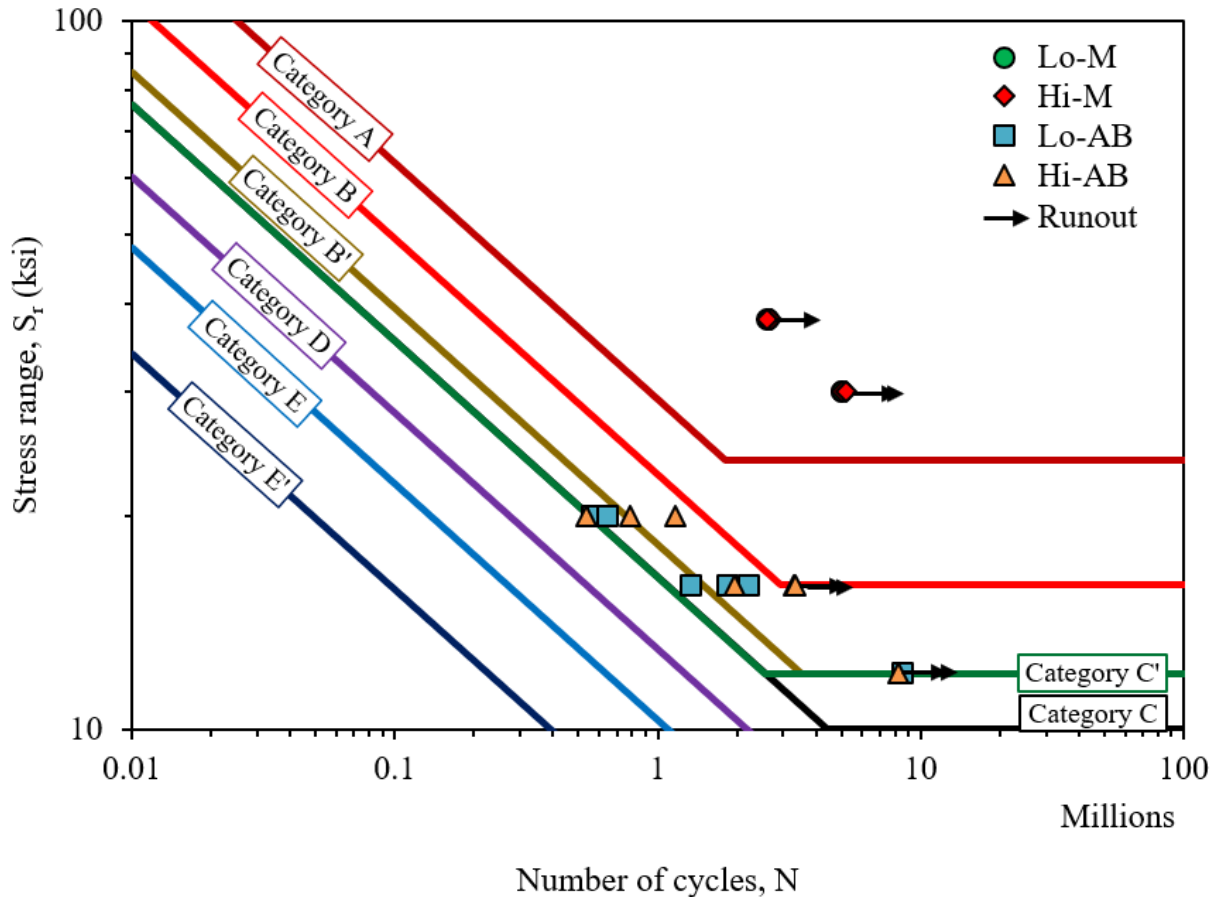
Specimens either fractured or were considered runouts after they exceeded the upper bound of a target AASHTO detail category. AASHTO Table 6.6.1.2.5-1 provides S-N curve parameters for design life (95 percent confidence limit per National Cooperative Highway Research Program (NCHRP) Report 286), and Strategic Highway Research Program Report S2-R19B-RW-1 provides parameters to adjust to mean life S-N curves (50 percent probability of failure) [100,101].

To determine if a specimen qualified as a runout upper bound curves for each detail category were calculated. These upper bound curves were determined by adding the difference between the number of cycles,  $N$ , for the design life and mean life to the value of  $N$  of the mean curves for a corresponding stress range,  $S_r$ . Revised detail category constants,  $A$ , were determined from power regressions. The upper bound curves had approximately a 95 percent probability of failure. Table 22 shows the number of cycles, stress range, and R-ratio for each specimen tested. Figure 22 plots the number of cycles versus stress range for each specimen tested compared to the design life design curves for AASHTO detail categories A-E'.

**Table 22. Number of cycles, stress range, and R-ratio for each specimen tested.**

<b>Specimen ID</b>	<b>Number of Cycles, N</b>	<b>Stress Range, S<sub>r</sub> (ksi)</b>	<b>R-ratio</b>
Hi-AB-4	8,200,000*	12	0.25
Lo-AB-1	8,524,000*	12	0.25
Hi-AB-1	3,300,000*	16	0.20
Hi-AB-5	3,334,623*	16	0.20
Hi-AB-7	1,951,212	16	0.20
Lo-AB-2	2,207,810	16	0.20
Lo-AB-5	1,329,223	16	0.20
Lo-AB-7	1,839,998	16	0.20
Hi-AB-3	1,163,333	20	0.18
Hi-AB-6	783,407	20	0.18
Hi-AB-8	538,821	20	0.18
Lo-AB-4	561,956	20	0.17
Lo-AB-6	589,588	20	0.17
Lo-AB-8	642,689	20	0.20
Hi-M-6	5,000,001*	30	0.25
Hi-M-7	5,187,253*	30	0.25
Lo-M-5	5,000,000*	30	0.25
Lo-M-6	5,000,001*	30	0.25
Hi-M-4	2,706,093*	38	0.10
Hi-M-8	2,613,893*	38	0.10
Lo-M-3	2,600,000*	38	0.10
Lo-M-4	2,628,123*	38	0.10

\*Runout.



Source: FHWA.

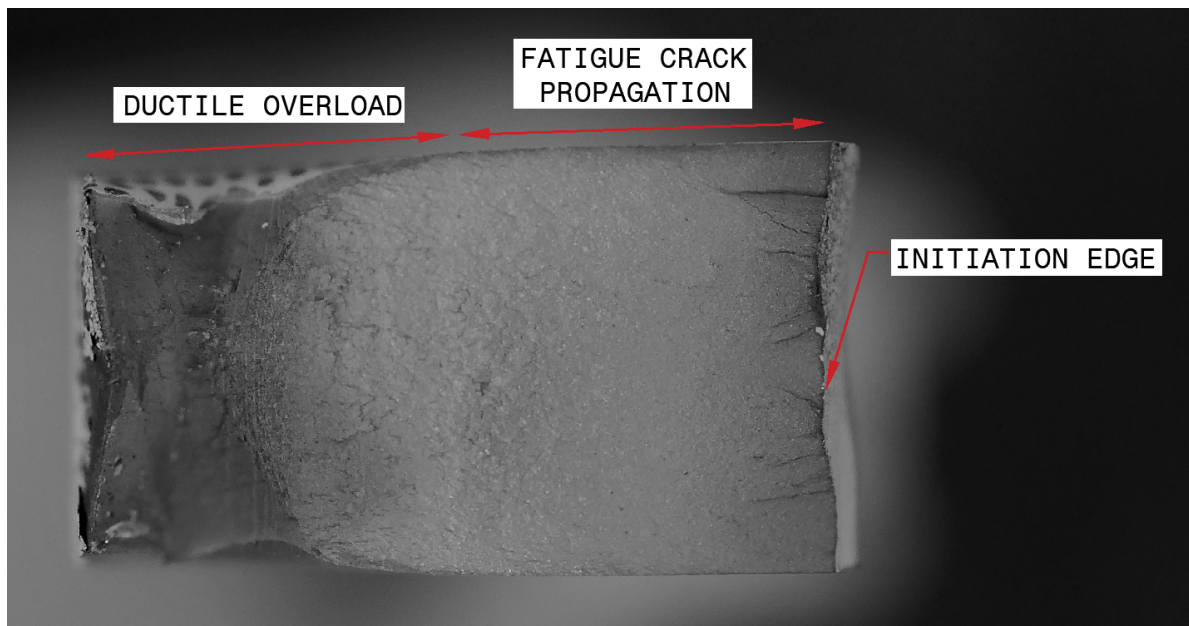
**Figure 22. Graph. S-N values for each specimen tested compared to design life AASHTO detail categories A-E'.**

All machined specimens tested ran out the number of cycles at the upper bound of AASHTO detail category A at both the 30 ksi and 38 ksi stress ranges. Specimens Hi-AB-4 and Lo-AB-1 ran out the number of cycles at upper bound of AASHTO detail category C at a stress range of 12 ksi. Specimens Hi-AB-1 and Hi-AB-5 ran out the number of cycles at upper bound of AASHTO detail category C at a stress range of 16 ksi. All specimens, except Hi-AB-8, exceeded the design life limit for category C at each corresponding stress range. All specimens considered runouts were checked for any fatigue crack initiation using magnetic particle inspection. No fatigue cracks were observed in any of the runout specimens.

Notably, all AB specimens that did not run out fractured within the gauge length, further suggesting that the undercut from the hand finishing did not influence the behavior. The typical fracture surface with initiation locations, fatigue crack propagation, and ductile overload indicated is shown in Figure 23. Figure 24 is a side view of the failure location. As expected, the initiation location for all specimens was in the valley between successive printed layers due to the local stress concentration.

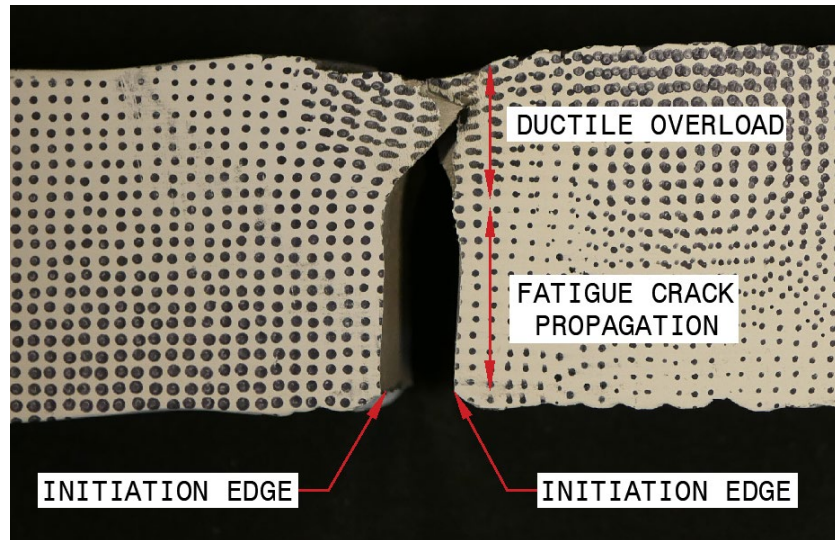
The average notch depth was determined for each specimen as the average peak-to-peak measurement minus the average valley-to-valley measurement divided by two. The failure notch depth was determined for each specimen as the largest peak-to-peak measurement adjacent to the failure notch minus the valley-to-valley measurement divided by two. The arithmetic mean height,  $R_a$ , and maximum height,  $R_t$ , for each AB specimen were determined with a digital profilometer after testing. The digital profilometer used a tip radius of 0.08 thousandths of an inch and an angle of 60 degrees, no noise filters were applied. Because  $R_a$  and  $R_t$  were determined after testing, it was only possible to measure across an evaluation length of 1 inch on one side of each specimen furthest away from the failure surface.  $R_t$  could not be determined exactly in accordance with Method B from ASTM D4417-21 because the tip radius is required to be 0.002 inches and only one reading could be taken in one location [102].

The average peak-to-peak, average valley-to-valley, average notch depth, failure notch depth measurements,  $R_a$ , and  $R_t$  are presented in Table 23. The Hi-AB and Lo-AB specimens had the same average notch depth of 0.014 inches. The values of  $R_a$  for the Hi-AB and Lo-AB specimens were similar at 7.06 and 7.07 thousandths of an inch, respectively. Similarly, the values of  $R_t$  for the Hi-AB and Lo-AB specimens were close at 35.93 and 37.98 thousandths of an inch, respectively. The failure notch depths for the Hi-AB and Lo-AB specimens were similar at 0.022 inches and 0.020 inches, respectively. All failure notch depths were deeper than the average notch depth, except for specimen Lo-AB-7.



Source: FHWA.

**Figure 23. Photo. Typical fracture surface and initiation locations, fatigue crack propagation, and fast fracture (view of failure surface).**



Source: FHWA.

**Figure 24. Photo. Typical fracture surface and initiation locations, fatigue crack propagation, and fast fracture (side view).**

**Table 23. Average notch and failure notch geometry for each specimen.**

Specimen ID	Avg. Peak-to-peak Width (in)	Avg. Valley-to-valley Width (in)	Avg. Notch Depth (in)	Failure Notch Depth (in)	Arithmetic Mean Height, $R_a$ (mils)	Max. Height, $R_t$ (mils)	Stress Range (ksi)	Number of Cycles
Hi-AB-1	0.989	0.964	0.013	—	4.89	22.38	16	3,300,000*
Hi-AB-3	0.978	0.952	0.013	0.017	5.33	27.74	20	1,163,333
Hi-AB-4	0.982	0.955	0.013	—	7.55	43.60	12	8,200,000*
Hi-AB-5	0.977	0.946	0.015	—	5.27	28.09	16	3,334,623*
Hi-AB-6	0.969	0.946	0.011	0.017	10.28	47.95	20	783,407
Hi-AB-7	0.971	0.939	0.016	0.032	9.09	43.04	16	1,951,212
Hi-AB-8	0.970	0.941	0.014	0.022	7.04	38.70	20	538,821
<i>Hi-AB Avg.</i>	<i>0.977</i>	<i>0.949</i>	<i>0.014</i>	<i>0.022</i>	<i>7.06</i>	<i>35.93</i>	<i>N/A</i>	<i>N/A</i>
Lo-AB-1	1.007	0.976	0.015	—	6.13	30.28	12	8,524,000*
Lo-AB-2	0.998	0.969	0.014	0.019	8.98	50.86	16	2,207,810
Lo-AB-4	1.000	0.971	0.015	0.024	6.49	36.40	20	561,956
Lo-AB-5	0.993	0.966	0.014	0.018	6.21	34.61	16	1,329,223
Lo-AB-6	0.996	0.970	0.013	0.019	9.49	50.27	20	589,588
Lo-AB-7	0.993	0.968	0.013	0.010	7.13	36.98	16	1,839,998
Lo-AB-8	1.000	0.971	0.014	0.027	5.08	26.42	20	642,689
<i>Lo-AB Avg.</i>	<i>0.998</i>	<i>0.970</i>	<i>0.014</i>	<i>0.020</i>	<i>7.07</i>	<i>37.98</i>	<i>N/A</i>	<i>N/A</i>

— specimen did not fracture (i.e. no failure notch).

\*Runout.

## **DISCUSSION**

### **Tension Testing**

#### ***Isotropy/Anisotropy in Results***

The ratios between each specimen direction (i.e., BD, DD, and 45) with respect to each of the other directions for the average tensile strength, average yield strength, and average percent elongation at fracture are presented in Table 24. Generally, difference between the three directions for ultimate and yield strength was low, with ratios ranging from 0.95 to 1.05. The difference between the three directions for percent elongation at fracture was more variable, with ratios ranging from 0.76 to 0.97. The smallest ratios of percent elongation at fracture for all walls were 45 over DD ratios. The largest ratios of percent elongation at fracture for walls F70Lo, F80Lo, and F80 high were 45 over BD ratios. The largest ratio of percent elongation at fracture for wall F70Hi was the BD over DD ratio.

**Table 24. Tensile result comparison between directions tested.**

<b>Wall ID</b>	<b>Ratio of Yield Strengths, BD/DD</b>	<b>Ratio of Yield Strengths, 45/BD</b>	<b>Ratio of Yield Strengths, 45/DD</b>	<b>Ratio of Tensile Strengths, BD/DD</b>	<b>Ratio of Tensile Strengths, 45/BD</b>	<b>Ratio of Tensile Strengths, 45/DD</b>	<b>Ratio of Elongation at Fracture, BD/DD</b>	<b>Ratio of Elongation at Fracture, 45/BD</b>	<b>Ratio of Elongation at Fracture, 45/DD</b>
F70Lo	0.96	1.05	1.00	0.99	1.02	1.00	0.86	0.91 <sup>^</sup>	0.79 <sup>^</sup>
F70Hi	0.95	1.01	0.96	0.99	1.00	0.99	0.96	0.88	0.85
F80Lo	0.96	1.04	0.99	0.99	1.01	1.00	0.86	0.88	0.76
F80Hi	0.98	1.00	0.98	1.00	1.00	1.00	0.94*	0.97	0.91*

<sup>^</sup>Elongation at fracture of specimen F70Lo-45-1 not reported because specimen was tested on an unaligned UTM. Average and standard deviation were calculated without this elongation value.

\*Average and standard deviation not including the elongation at fracture of specimen F80Hi-DD-2, which had an internal discontinuity in its gauge length.

### ***Comparison to Filler Metal Requirements***

The AWS A5.18 and A5.28 Specifications define the minimum requirements for deposited weld metal in terms of yield strength, tensile strength, and elongation. These cover the ER70S-6 and ER80S-Ni1 fillers used in the current project, respectively. Table 25 and Table 26 report the ratios between the average of the tensile results tested in the three directions to the AWS A5.18 and A5.28 minimum requirements, respectively. A ratio greater than 1.0 indicates that the tested value met the requirement and a ratio less than 1.0 indicates that the tested value did not meet the requirement. It should be noted that the gas compositions tested in the current study do not match that used in the classification; as such, deviations in strength and elongation at fracture can be expected.

The average DD and 45 specimens from F70Lo met the minimum requirement for minimum yield strength; however, the average BD specimen did not meet the minimum requirement. All of the average specimens from F70Lo met the minimum requirement for tensile strength. None of the average specimens from F70Hi met the minimum yield or tensile strength requirements. None of the average specimens from F80Lo met the minimum yield or tensile strength requirement. None of the average specimens from F80Hi met the minimum yield or tensile strength requirement. All average specimens from all directions and all walls met the minimum elongation requirement (not including specimen F70Lo-45-1 and F80Hi-DD-2, which were redacted from the dataset).

**Table 25. Average tensile result comparison between directions tested and AWS 5.18 requirements.**

Wall ID	Ratio of Yield	Ratio of Yield	Ratio of Yield	Ratio of Tensile	Ratio of Tensile	Ratio of Tensile	Ratio of	Ratio of	Ratio of
	Strength, BD/AWS 5.18	Strength, DD/AWS 5.18	Strength, 45/AWS 5.18	Strength, BD/AWS 5.18	Strength, DD/AWS 5.18	Strength, 45/AWS 5.18	Elongation, BD/AWS 5.18	Elongation, DD/AWS 5.18	Elongation, 45/AWS 5.18
F70Lo	0.97	1.01	1.02	1.04	1.06	1.06	1.61	1.86	1.47 <sup>^</sup>
F70Hi	0.79	0.83	0.80	0.93	0.94	0.93	1.98	2.05	1.74

Note: Ratios calculated using the minimum requirements in AWS 5.18 of 58 ksi yield strength, 70 ksi tensile strength, and 22 percent elongation at fracture.

<sup>^</sup>Elongation at fracture of specimen F70Lo-45-1 not reported because specimen was tested on an unaligned UTM. Average and standard deviation were calculated without this elongation value.

**Table 26. Average tensile result comparison between directions tested and AWS 5.28 requirements.**

Wall ID	Ratio of Yield	Ratio of Yield	Ratio of Yield	Ratio of Tensile	Ratio of Tensile	Ratio of Tensile	Ratio of	Ratio of	Ratio of
	Strength, BD/AWS 5.28	Strength, DD/AWS 5.28	Strength, 45/AWS 5.28	Strength, BD/AWS 5.28	Strength, DD/AWS 5.28	Strength, 45/AWS 5.28	Elongation, BD/AWS 5.28	Elongation, DD/AWS 5.28	Elongation, 45/AWS 5.28
F80Lo	0.87	0.91	0.90	0.96	0.97	0.97	1.40	1.62	1.49
F80Hi	0.76	0.77	0.76	0.89	0.89	0.89	1.66	1.77*	1.61

Note: Ratios calculated using the minimum requirements in AWS 5.28 of 68 ksi yield strength, 80 ksi tensile strength, and 24 percent elongation at fracture.

\*Average and standard deviation not including the elongation at fracture of specimen F80Hi-DD-2, which had an internal discontinuity in its gauge length.

### ***Comparison of ER70S-6 Results to Literature***

In addition to the results presented from the current study, the tensile properties of ER70S-6 WAAM steel have been quantified in 33 additional studies from the literature. Most studies evaluated tensile specimens in at least two directions of the build. These directions correspond to the longitudinal axis of the tensile specimen parallel to the BD and the longitudinal axis of the tensile specimen parallel to the DD (i.e., perpendicular to the BD). In addition, a small subset of studies tested specimens fabricated with their longitudinal axes oriented at a 45-degree angle between the build and deposition directions.

Various parameters of the welding process can influence the material properties of the as-fabricated WAAM material. The wire diameter, voltage, current range, wire feed rate, print travel speed, approximate heat input, and shielding gas mixture used in the studies from the literature are synthesized in Table 27. Additionally, process notes are included in the table describing any unique variables (e.g., bead oscillation pattern, surface finish, etc.) investigated in each study. Note, not all process parameters were reported for all studies, including the current study in which the specific details of the welding process are proprietary to the service provider. This limits the comparisons that can be drawn between the data. For example, the studies cannot be organized or grouped by voltage, a variable that some studies did not report. Comparisons may only be drawn broadly between the yield strength, ultimate strength, and elongation at fracture between all studies that used ER70S-6 as the feedstock material in the following sections.

Table 28 includes the number of specimens tested for each orientation of the fabrication. In the table, “BD” denotes specimens with the longitudinal axes parallel to the build direction, “DD” denotes specimens with the longitudinal axes parallel to the deposition direction, and “45” denotes specimens with the longitudinal axes at a 45-degree angle between the build and deposition directions. Note, all-weld metal specimens are created in the DD for the qualification of structural welds. Finally, the specimen thickness for each study is included.

The average yield, tensile strength, and percent elongation at fracture for each specimen type (i.e., specimen orientation) from the literature are presented in Table 29. Most studies did not report the strain rates of the specimens or the method for determining yield strength. As such, these items are not included in the summary tables but would influence the results. To quantify the extent of anisotropy observed in each of the studies, the average across all studies for yield strength, tensile strength, and percentage elongation at fracture for each specimen direction, along with the ratio between the yield strength, tensile strength, and elongation at fracture are also presented in Table 29. The average and standard deviations presented for the entire dataset available in the literature do not account for the different specimen counts tested by each study because not all studies reported individual specimen data or the number of specimens tested.

**Table 27. Welding process and specimen parameters for available tensile tests on WAAM ER70S-6 in the literature.**

Reference	Process Notes	Wire Diameter (in)	Voltage (V)	Current Range (A)	Wire Feed Rate (ft/min)	Print Travel Speed (in/min)	Welding Heat Input (kJ/in)	Shielding Gas Composition (Percent)
Haden et al. (2017) [31]	—	0.035	19.0	—	16.7	6.0	—	75 Ar / 25 CO2
Lu et al. (2017) [32]	—	0.031	20.0	132	23.9	23.6	6.7	95 Ar / 5 CO2
Sridharan et al. (2018) [33]	—	—	—	230-270	—	—	—	—
Corpus (2019) [34]	Cooled between layers	0.023	30.0	160	110.0	16.0	18.0	60 Ar / 40 CO2
Corpus (2019) [34]	Actively cooled	0.023	30.0	160	110.0	16.0	18.0	60 Ar / 40 CO2
Dirisu et al. (2019) [26]	CMT, oscillated	0.047	13.3	157	21.3	15.7	8.0	80 Ar / 20 CO2
Ghaffari et al. (2019) [35]	Machined	0.035	28.0	320	20.5	11.8	45.5	100 Ar
Ghaffari et al. (2019) [35]	As-built	0.035	28.0	320	20.5	11.8	45.5	100 Ar
Hu et al. (2019) [36]	—	—	—	—	—	—	—	—
Muller et al. (2019) [25]	GMAW	0.039	27.6	218	34.8	—	142.8**	82 Ar / 18 CO2
Muller et al. (2019) [25]	CMT standard	0.039	11.1	158	16.4	—	66.8**	82 Ar / 18 CO2
Muller et al. (2019) [25]	CMT cycle step	0.039	16.4	204	30.8	—	53.2**	82 Ar / 18 CO2
Rafieazad et al. (2019) [37]	—	0.035	28.0	320	20.5	11.8	45.5	100 Ar
Ron et al. (2019) [38]	—	0.047	23.9	210	20.0	5.5	54.6	98 Ar / 2 O2
Waqas et al. (2019) [39]	—	—	—	—	—	—	—	—
Aldalur et al. (2020) [40]	Overlapped	0.047	27.1	229	26.2	25.6	14.5	80 Ar / 20 CO2
Aldalur et al. (2020) [40]	Oscillated	0.047	26.6	244	26.2	7.9	49.5	80 Ar / 20 CO2
Ermakova et al. (2020) [30]	CMT	0.047	—	—	24.6	17.3	—	80 Ar / 20 CO2
Feucht et al. (2020) [41]	Manufactured at 45° angle, CMT cycle step	0.047	—	—	13.1	7.9-11.8	—	82 Ar / 18 CO2
Hassen et al. (2020) [42]	—	0.043	—	—	16.7	16.1	—	90 Ar / 10 CO2
Kotteman (2020) [43]	Thin, as-built	—	—	—	—	—	—	—
Kotteman (2020) [43]	Thick, machined	—	—	—	—	—	—	—
Kotteman (2020) [43]	Thin, as-built	—	—	—	—	—	—	—
Kotteman (2020) [43]	Thick, machined	—	—	—	—	—	—	—
Le et al. (2020) [44]	—	0.047	18.0	70	—	11.8	19.2	100 CO2
Nemani et al. (2020) [45]	—	0.035	28.0	135	20.5	—	19.2	—
Al-Nabulsi et al. (2021) [46]	Flat sheet, HAZ	0.047	—	—	—	—	—	—
Astarita et al. (2021) [47]	—	0.031	18.0	80	0.0	7.9	11.0	—
Ayan and Kahraman (2021) [48]	Fixed torch	0.047	23.0	90-100	6.6	3.9	31.5-35.1	86 Ar / 12 CO2 / 2 O2
Ayan and Kahraman (2021) [48]	Moveable torch	0.047	23.0	90-100	6.6	3.9	31.5-35.1	86 Ar / 12 CO2 / 2 O2
Douglass and Schaeffer (2021) [49]	Fast cooling rate	—	—	—	—	—	10.0	—
Douglass and Schaeffer (2021) [49]	Slow cooling rate	—	—	—	—	—	27.0	—
Nagasai et al. (2021) [50]	CMT	0.047	18.3	227	22.0	15.7	15.8	85 Ar / 15 CO2
Rafieazad et al. (2021) [51]	—	0.035	—	—	—	—	—	—
Silvestru et al. (2021) [52]	CMT cycle step, as-built	0.047	—	—	—	—	—	80 Ar / 20 CO2
Silvestru et al. (2021) [52]	CMT cycle step, machined	0.047	—	—	—	—	—	80 Ar / 20 CO2
Xin et al. (2021) [53]	—	0.039	—	—	—	—	—	—
Ayan and Kahraman (2022) [54]	—	0.047	17-19	105-120	6.6	5.9	217.7-278.0	86 Ar / 12 CO2 / 2 O2
Goviazin et al. (2022) [55]	—	—	—	—	—	—	—	—
Guo et al. (2022) [56]	Short-arc, as-built	0.031	14.8	54	9.8	18.9	2.5	80 Ar / 20 CO2
Guo et al. (2022) [56]	Short-arc, machined	0.031	14.8	54	9.8	18.9	2.5	80 Ar / 20 CO2
Guo et al. (2022) [56]	Pulsed, as-built	0.047	24.8	130	13.1	18.9	10.2	80 Ar / 20 CO2
Guo et al. (2022) [56]	Pulsed, machined	0.047	24.8	130	13.1	18.9	10.2	80 Ar / 20 CO2
Huang et al. (2022) [57]	Short-arc, as-built	0.031	14.8	54	9.8	18.9	2.5	82 Ar / 18 CO2
Huang et al. (2022) [57]	Short-arc, machined	0.031	14.8	54	9.8	18.9	2.5	82 Ar / 18 CO2
Huang et al. (2022) [57]	Pulsed, as-built	0.047	24.8	130	13.1	18.9	10.2	82 Ar / 18 CO2
Huang et al. (2022) [57]	Pulsed, machined	0.047	24.8	130	13.1	18.9	10.2	82 Ar / 18 CO2
Shamir et al. (2022) [58]	—	0.047	—	—	23.0	15.7	—	80 Ar / 20 CO2
Tankova et al. (2022) [59]	CMT, as-built	0.039	15.7	155	19.7	23.6	6.2	98 Ar / 2 CO2
Tankova et al. (2022) [59]	CMT, machined	0.039	15.7	155	19.7	23.6	6.2	98 Ar / 2 CO2
Tripathi et al. (2022) [60]	GTAW	0.031	—	95	—	31.5	—	99 Ar
Current Study	Lo interpass temperature	0.045	—	—	—	—	15.0*	90 Ar / 10 CO2
Current Study	Hi interpass temperature	0.045	—	—	—	—	14.5*	90 Ar / 10 CO2

— no data was reported.

\*Average of the heat inputs reported for the inner and outer beads.

\*\*Approximated based on energy per layer and layer thicknesses provided.

**Table 28. Summary of specimen of available tensile tests on WAAM ER70S-6 in the literature.**

Reference	Process Notes	Surface Finish	Tensile Specimen Type	Specimen Thickness or Diameter (in)	Gauge Length (in)	Number of BD Specimens	Number of DD Specimens	Number of 45 Specimens
Haden et al. (2017)	—	Machined	Flat bar	0.100	1.000	5	3	—
Lu et al. (2017)	—	Machined	Flat bar	0.020	0.197	3	3	—
Sridharan et al. (2018)	—	Machined	Flat bar	0.197	3.500	8	5	—
Corpus (2019)	Cooled between layers	Machined	Flat bar	0.375**	—	—	5	—
Corpus (2019)	Actively cooled	Machined	Flat bar	0.375**	—	—	5	—
Dirisu et al. (2019)	CMT, oscillated	Machined	Flat bar	0.118	1.260	3	3	—
Ghaffari et al. (2019)	Machined	Machined	Flat bar	0.197	—	—	—	—
Ghaffari et al. (2019)	As-built	As-built	Flat bar	0.197	—	—	—	—
Hu et al. (2019)	—	Machined	Flat bar	0.059	0.709	4	1	—
Muller et al. (2019)	GMAW	Machined	Round	0.354	1.181	1	—	—
Muller et al. (2019)	CMT standard	Machined	Round	0.354	1.181	1	—	—
Muller et al. (2019)	CMT cycle step	Machined	Round	0.354	1.181	1	—	—
Rafieezad et al. (2019)	—	Machined	Flat bar	0.197	0.984	5	5	—
Ron et al. (2019)	—	Machined	Round	0.150	1.000	—	—	—
Waqas et al. (2019)	—	Machined	Flat bar	0.157	0.984	2	2	—
Aldalur et al. (2020)	Overlapped	Machined	Round	0.157	0.866	6	6	—
Aldalur et al. (2020)	Oscillated	Machined	Round	0.157	0.866	6	6	—
Ermakova et al. (2020)	CMT	Machined	Round	0.315	—	2	2	—
Feucht et al. (2020)	Manufactured at 45° angle, CMT cycle step	Machined	Flat bar	0.118	1.181	—	7	—
Hassen et al. (2020)	—	Machined	Flat bar	0.186	—	5	5	5
Kotteman (2020)	Thin, as-built	As-built	Flat bar	0.118	2.283	7	7	7
Kotteman (2020)	Thick, machined	As-built	Flat bar	0.236	2.283	7	7	7
Kotteman (2020)	Thin, as-built	Machined	Flat bar	0.064	2.283	3	3	3
Kotteman (2020)	Thick, machined	Machined	Flat bar	0.144	2.283	3	3	3
Le et al. (2020)	—	—	—	—	—	—	—	—
Nemani et al. (2020)	—	Machined	Flat bar	0.197	3.937	5	5	0
Al-Nabulsi et al. (2021)	Flat sheet, HAZ	Machined	Flat bar	0.669	4.094	—	3	0
Astarita (2021)	—	Machined	Flat bar	0.118	0.787	2	2	—
Ayan and Kahraman (2021)	Fixed torch	Machined	Flat bar	0.079	2.126	2	2	2
Ayan and Kahraman (2021)	Moveable torch	Machined	Flat bar	0.079	2.126	2	2	2
Douglass and Schaeffer (2021)	Fast cooling rate	Machined	Round	—	—	—	—	—
Douglass and Schaeffer (2021)	Slow cooling rate	Machined	Round	—	—	—	—	—
Nagasai et al. (2021)	CMT	Machined	Flat bar	0.157	0.984	6	—	—
Rafieezad et al. (2021)	—	Machined	Flat bar	0.197	—	5*	5*	5*
Silvestru et al. (2021)	CMT cycle step, as-built	As-built	Round	0.315**	1.378	12	—	9
Silvestru et al. (2021)	CMT cycle step, machined	Machined	Round	0.315	1.181	21	—	—
Xin et al. (2021)	—	Machined	Flat bar	0.111	0.984	3	2	3
Ayan and Kahraman (2022)	—	Machined	Flat bar	0.098	1.260	6	6	—
Goviazin et al. (2022)	—	Machined	Round	0.236	1.181	—	—	—
Guo et al. (2022)	Short-arc, as-built	As-built	Flat bar	0.118**	—	4	4	5
Guo et al. (2022)	Short-arc, machined	Machined	Flat bar	0.118	—	1	1	1
Guo et al. (2022)	Pulsed, as-built	As-built	Flat bar	0.315**	—	3	2	3
Guo et al. (2022)	Pulsed, machined	Machined	Flat bar	0.315	—	1	1	1
Huang et al. (2022)	Short-arc, as-built	As-built	Flat bar	0.118**	3.937	8	3	3
Huang et al. (2022)	Short-arc, machined	Machined	Flat bar	0.118	3.937	3	3	3
Huang et al. (2022)	Pulsed, as-built	As-built	Flat bar	0.315**	3.937	16	10	9
Huang et al. (2022)	Pulsed, machined	Machined	Flat bar	0.315	3.937	12	9	9
Shamir et al. (2022)	—	Machined	—	—	—	3	3	—
Tankova et al. (2022)	CMT, as-built	As-built	Flat bar	0.197**	1.181	3	3	3
Tankova et al. (2022)	CMT, machined	Machined	Flat bar	0.197	1.181	3	3	3
Tripathi et al. (2022)	GTAW	Machined	Flat bar	0.157	0.787	3	3	—
Current Study	Lo interpass temperature	Machined	Flat bar	0.500	2.000	3	3	3
Current Study	Hi interpass temperature	Machined	Flat bar	0.500	2.000	3	3	3

— no data was reported.

\*\*Nominal thickness or diameter

Table 29. Summary of specimen tensile strengths of available tensile tests on WAAM ER70S-6 in the literature.

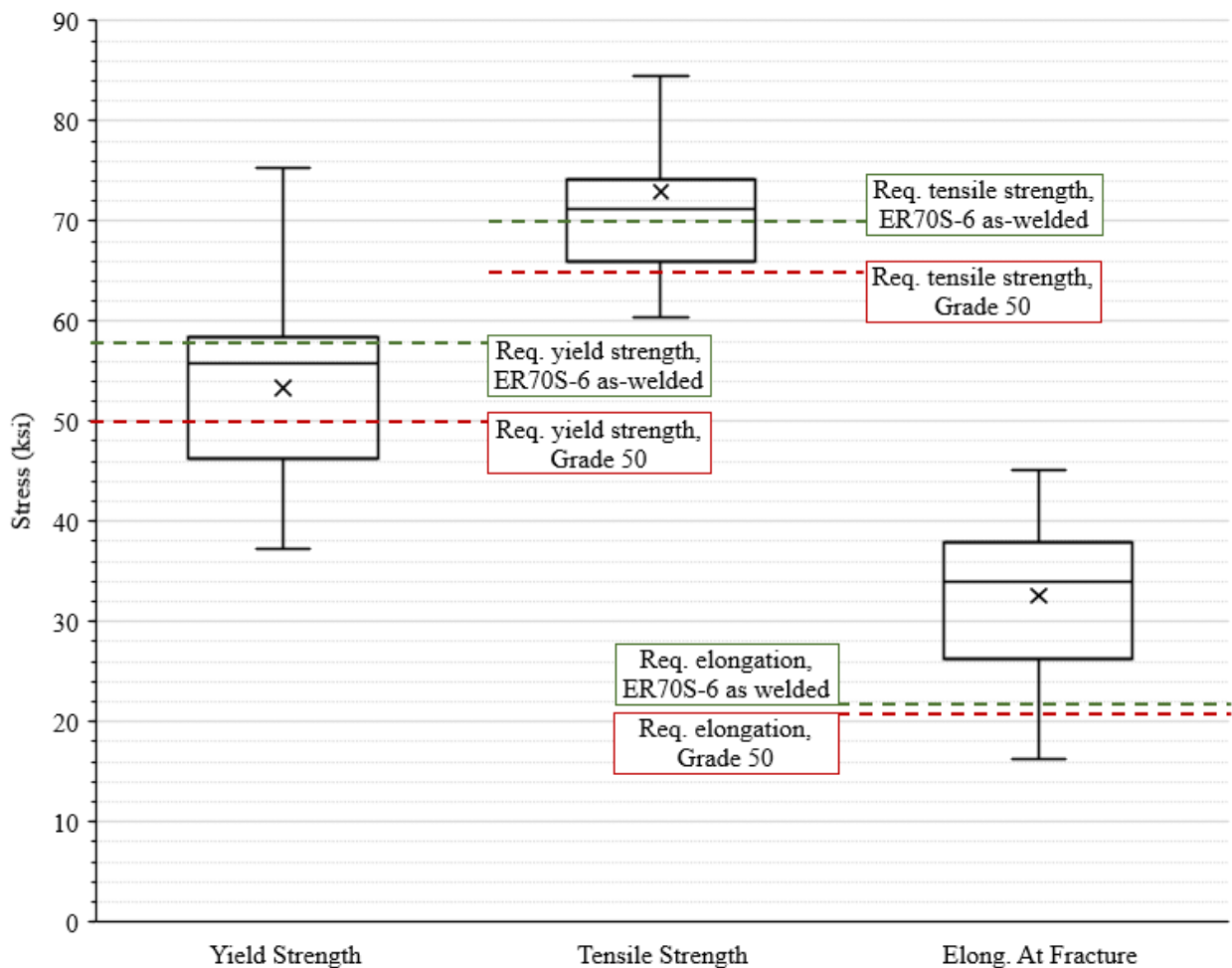
Reference	Process Notes	Yield Strength, BD (ksi)	Tensile Strength, BD (ksi)	Total Elongation at Fracture, BD (Percent)	Yield Strength, DD (ksi)	Tensile Strength, DD (ksi)	Total Elongation at Fracture, DD (Percent)	Yield Strength, 45 (ksi)	Tensile Strength, 45 (ksi)	Total Elongation at Fracture, 45 (Percent)	Yield Strength Ratio, BD/DD	Tensile Strength Ratio, BD/DD	Elongation at Fracture Ratio, BD/DD
Haden et al. (2017)	—	38.4	69.9	—	37.2	68.9	—	—	—	—	1.03	1.01	—
Lu et al. (2017) <sup>^</sup>	—	66.9	89.7	28.2	75.3	100.6	36.8	—	—	—	0.89	0.89	0.77
Sridharan et al. (2018)	—	56.6	72.4	21.9	63.8	72.5	24.6	—	—	—	0.89	1.00	0.89
Corpus (2019)	Cooled between layers	—	—	—	—	80.4	—	—	—	—	—	—	—
Corpus (2019) <sup>^</sup>	Actively cooled	—	—	—	—	144.8	—	—	—	—	—	—	—
Dirisu et al. (2019)	CMT, oscillated	52.8	74.3	34.3	53.5	74.7	32.8	—	—	—	0.99	0.99	1.05
Ghaffari et al. (2019)	Machined	—	71.1	12.0	—	72.9	35.0	—	—	—	—	0.97	0.34
Ghaffari et al. (2019)	As-built	—	66.3	29.0	—	68.6	34.0	—	—	—	—	0.97	0.85
Hu et al. (2019)	—	52.2	76.9	32.9	60.9	82.5	35.6	—	—	—	0.86	0.93	0.92
Muller et al. (2019)	GMAW	38.4	64.5	49.7	—	—	—	—	—	—	—	—	—
Muller et al. (2019)	CMT standard	59.5	80.6	46.3	—	—	—	—	—	—	—	—	—
Muller et al. (2019)	CMT cycle step	56.6	81.9	4.7	—	—	—	—	—	—	—	—	—
Rafieazad et al. (2019)	—	56.3	72.1	—	59.5	72.2	—	—	—	—	0.95	1.00	—
Ron et al. (2019)	—	53.1	69.0	34.6	—	—	—	—	—	—	—	—	—
Waqas et al. (2019)	—	43.0	69.5	12.5	47.4	84.6	30.0	—	—	—	0.91	0.82	0.42
Aldalur et al. (2020)	Overlapped	53.4	72.6	32.0	53.4	72.2	36.0	—	—	—	1.00	1.01	0.89
Aldalur et al. (2020)	Oscillated	49.0	68.7	36.0	51.3	69.3	38.0	—	—	—	0.95	0.99	0.95
Ermakova et al. (2020)	CMT	52.9	75.1	43.0	56.6	75.7	44.0	—	—	—	0.94	0.99	0.98
Feucht et al. (2020)	Manufactured at 45 angle, CMT cycle step	58.4	76.4	33.0	—	—	—	—	—	—	—	—	—
Hassen et al. (2020)	—	—	67.8	—	—	68.3	—	—	67.0	—	—	0.99	—
Kotteman (2020)	Thin, as-built	49.5	67.3	16.3	55.8	69.3	17.7	49.3	66.1	16.7	0.89	0.97	0.92
Kotteman (2020)	Thick, machined	38.9	58.3	14.0	45.8	62.4	19.2	40.9	59.5	17.5	0.85	0.93	0.73
Kotteman (2020)	Thin, as-built	60.3	74.1	18.1	58.0	72.4	16.3	57.0	70.2	16.9	1.04	1.02	1.11
Kotteman (2020)	Thick, machined	47.3	67.6	16.7	46.1	67.1	20.6	52.1	67.9	19.5	1.03	1.01	0.81
Le et al. (2020)	—	52.5	69.5	—	46.4	62.2	—	—	—	—	1.13	1.12	—
Nemani et al. (2020)	—	58.4	72.9	11.1	56.7	74.0	34.7	—	—	—	1.03	0.99	0.32
Al-Nabulsi et al. (2021)	Flat sheet, HAZ	—	—	—	57.6	68.7	29.7	—	—	—	—	—	—
Astarita (2021)	—	58.0	78.4	18.9	56.8	75.0	17.6	—	—	—	1.02	1.05	1.07
Ayan and Kahraman (2021)	Fixed torch	—	64.5	28.4	—	65.3	29.5	—	64.5	27.6	—	0.99	0.96
Ayan and Kahraman (2021)	Moveable torch	—	64.4	27.6	—	64.6	28.4	—	65.4	28.7	—	1.00	0.97
Douglass and Schaeffer (2021)	Fast cooling rate	58.0	74.0	22.0	—	—	—	—	—	—	—	—	—
Douglass and Schaeffer (2021)	Slow cooling rate	47.0	70.0	53.0	—	—	—	—	—	—	—	—	—
Nagasai et al. (2021)	CMT	49.5	63.4	55.4	—	—	—	—	—	—	—	—	—
Rafieazad et al. (2021)	—	56.0	58.7	10.0	58.9	76.0	37.0	58.9	76.0	37.0	0.95	0.77	0.27
Silvestru et al. (2021)	CMT cycle step, as-built	50.2	68.6	—	—	—	—	50.3	69.0	—	—	—	—
Silvestru et al. (2021)	CMT cycle step, machined	52.1	71.0	32.6	—	—	—	—	—	—	—	—	—
Xin et al. (2021)	—	60.8	84.5	32.5	56.9	82.6	28.7	60.0	83.2	31.9	1.07	1.02	1.13
Ayan and Kahraman (2022)	—	—	69.6	22.5	—	71.2	24.6	—	—	—	—	0.98	0.91
Goviazin et al. (2022)	—	50.8	—	—	—	—	—	—	—	—	—	—	—
Guo et al. (2022)	Short-arc, as-built	51.5	67.7	22.0	59.2	73.7	26.0	51.6	68.0	24.0	0.87	0.92	0.85
Guo et al. (2022)	Short-arc, machined	53.9	70.2	35.0	58.7	72.9	26.0	53.1	69.9	39.0	0.92	0.96	1.35
Guo et al. (2022)	Pulsed, as-built	40.3	59.3	24.0	44.4	60.3	36.0	44.1	61.9	27.0	0.91	0.98	0.67
Guo et al. (2022)	Pulsed, machined	46.3	64.4	30.0	42.3	62.9	40.0	47.7	63.8	38.0	1.09	1.02	0.75
Huang et al. (2022)	Short-arc, as-built	51.1	67.1	23.0	56.0	70.2	34.0	53.7	69.0	28.0	0.91	0.96	0.68
Huang et al. (2022)	Short-arc, machined	56.8	70.5	33.0	56.6	71.1	38.0	56.8	69.5	32.0	1.01	0.99	0.87
Huang et al. (2022)	Pulsed, as-built	40.6	58.1	26.0	44.0	60.9	34.0	41.3	58.6	0.3	0.92	0.95	0.76
Huang et al. (2022)	Pulsed, machined	44.3	60.9	34.0	44.7	61.5	41.3	45.5	61.2	36.7	0.99	0.99	0.82
Shamir et al. (2022)	—	49.4	68.0	37.4	51.6	69.9	38.9	—	—	—	0.96	0.97	0.96
Tankova et al. (2022)	CMT, as-built	48.7	66.3	22.7	44.1	62.6	26.9	46.3	64.1	29.7	1.11	1.06	0.84
Tankova et al. (2022)	CMT, machined	54.5	72.8	36.3	54.1	72.4	37.8	55.7	74.1	36.9	1.01	1.01	0.96
Tripathi et al. (2022) <sup>§</sup>	GTAW	—	63.4	64.0	—	65.3	58.0	—	—	—	—	0.97	1.10
Current Study	Lo interpass temperature	56.4	73.0	35.3	58.8	73.9	40.9	59.0	74.3	32.3	0.96	0.99	0.86
Current Study	Hi interpass temperature	45.8	65.1	43.5	48.1	66.1	45.1	46.4	65.2	38.2	0.95	0.98	0.96
Average	N/A	51.5	69.8	29.4	53.3	72.9	32.6	51.0	67.6	27.9	0.97	0.98	0.85
Standard Deviation	N/A	6.5	6.5	12.6	7.5	13.4	8.6	5.8	5.6	9.6	0.07	0.06	0.23

— no data was reported

<sup>^</sup>Tensile strengths considered outliers from statistical analysis

<sup>§</sup>Elongation at fracture considered outlier from statistical analysis

Figure 25 presents a box and whisker plot that includes the yield strength, tensile strength, and elongation at fracture of the DD specimens from the literature compared to the minimum yield and tensile strength requirements of AWS A5.18 for as-welded ER70S-6 and ASTM A709/A709M-21 for Grade 50 steel [7,8]. The bottom, middle, and upper lines of each box represent each dataset's lower quartile, median, and upper quartile, respectively. The lower and upper whiskers extend to each dataset's lower and upper extremes, not including points considered outliers. Outliers fell above the maximum whisker for their data type, calculated at the fourth quartile minus 1.5 times the interquartile range. The “x” within each box represents the mean of the corresponding dataset. The quartiles were calculated exclusive of the median and the upper outliers for tensile strength (i.e., Lu et al.’s specimens and Corpus’s actively cooled specimens) and elongation at fracture (Tripathi et al.) are not shown on the plot.



Source: FHWA.

**Figure 25. Graph. Yield strength, tensile strength, and elongation at fracture of DD specimens from the current study and the literature compared to the minimum requirements of AWS A5.18 for as-welded ER70S-6 and ASTM A709 for Grade 50 steel.**

On average, the yield strengths of tests from the literature and the current study exceeded the required minimum yield strength for Grade 50 steel (50 ksi) but did not exceed the required

minimum yield strength for as-welded ER70S-6 (58 ksi). The entire upper half of the data exceeded the requirement for Grade 50 steel, but only the upper quartile exceeded the requirement for as-welded ER70S-6.

On average, the tensile strengths of tests from the literature and the current study exceeded the required minimum tensile strength for Grade 50 steel (65 ksi) and the required minimum tensile strength for as-welded ER70S-6 (70 ksi). The entire upper three-quarters of the data exceeded the requirement for Grade 50 steel, but only the upper half exceeded the requirement for as-welded ER70S-6.

On average, the elongation at fracture of tests from the literature and the current study exceeded the required minimum elongation for Grade 50 steel (18 percent for plates, 21 percent for shapes) and the required minimum elongation for as-welded ER70S-6 (22 percent). The entire upper three-quarters of the data exceeded both the Grade 50 and as welded ER70S-6 requirements.

The lowest BD over DD ratios for yield strength, tensile strength, and elongation at fracture were 0.85, 0.77, and 0.27, respectively. The highest BD over DD ratios for yield strength, tensile strength, and elongation at fracture were 1.13, 1.12, and 1.35, respectively. Note that the highest ratios did not occur in the same study, and the lowest ratios did not occur in the same study. When averaging all studies, the BD over DD ratio was 0.97 for yield strength, 0.98 for tensile strength, and 0.85 for elongation at fracture. As previously noted, the average values do not entirely represent the actual statistics because different specimen counts were used from study-to-study. Instead, the average values are used to describe general data trends. The BD over DD ratios between the yield and tensile strengths of the specimens tested as a part of the current study support the conclusion by most of the authors that there is no significant anisotropy of the yield or ultimate tensile strengths of WAAM ER70S-6 steel [31,35–37,40,47,48,51,53].

### ***Effects of Interpass Temperature***

Interpass temperature had the most significant impact on the yield and tensile strengths of the evaluated WAAM material. Table 30 compares the average yield and tensile strengths and average percent elongation at fracture of the walls based on interpass temperature. The ER70S-6 and ER80S-Ni1 WAAM materials produced with a low interpass temperature had higher average yield and tensile strengths. Conversely, on average, the low interpass temperature materials had lower percent elongation at fracture (i.e., lower ductility).

**Table 30. Comparison of the average yield and tensile strengths and average percent elongation at fracture for all walls based on interpass temperature.**

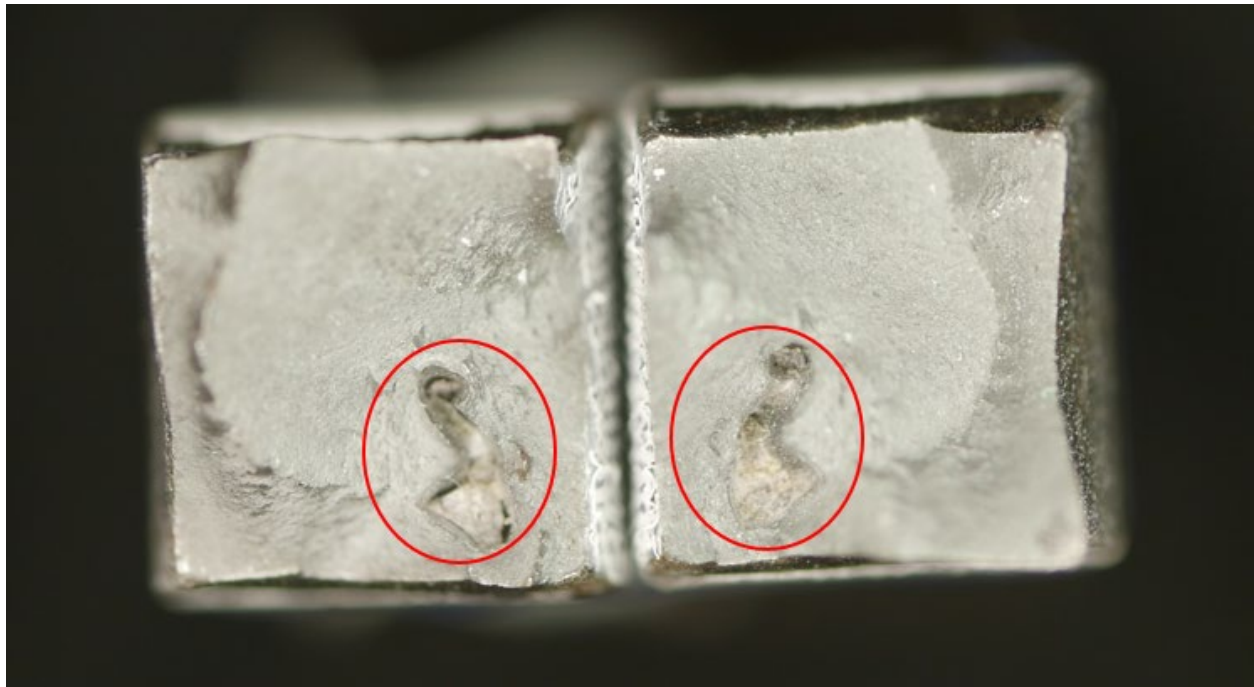
Wall ID	Interpass Temperature	Average Yield Stress (ksi)	Average Tensile Strength (ksi)	Average Elongation at Fracture (Percent)
F70Lo	Lo (250°F)	58.07	73.71	36.70 <sup>^</sup>
F70Hi	High (590°F)	46.78	65.48	42.28
<i>Difference</i>	<i>N/A</i>	<i>11.29</i>	<i>8.23</i>	<i>-5.58</i>
<i>F70Lo/F70Hi Ratio</i>	<i>N/A</i>	<i>1.24</i>	<i>1.13</i>	<i>0.87</i>
F80Lo	Lo (250°F)	60.24	77.35	32.21
F80Hi	High (710°F)	51.93	71.09	40.00*
<i>Difference</i>	<i>N/A</i>	<i>8.31</i>	<i>6.26</i>	<i>-7.79</i>
<i>F80Lo/F80Hi Ratio</i>	<i>N/A</i>	<i>1.16</i>	<i>1.09</i>	<i>0.81</i>

<sup>^</sup>Elongation at fracture of specimen F70Lo-45-1 not reported because specimen was tested on an unaligned UTM. Average and standard deviation were calculated without this elongation value.

\*Average and standard deviation not including the elongation at fracture of specimen F80Hi-DD-2, which had an internal discontinuity in its gauge length.

### *Effects of Internal Discontinuities*

Though specimens F80Lo-45-2, F80Hi-45-1, and F80Hi-45-2 all had visible discontinuities on the surfaces of the grip areas (Figure 5 through Figure 8), there was no significant difference between the yield and tensile strengths and percent elongation at fracture between these specimens and those without visible discontinuities. Specimen F80Hi-DD-2 was found to have an internal discontinuity in the gauge length (Figure 26). While the internal discontinuity was significantly sized, approximately 5.5 percent of the reduced section area at failure, the specimen yield and tensile strengths were still in close agreement with the other F80Hi-DD specimens. However, the percent elongation at fracture was significantly reduced compared to the other F80Hi-DD specimens, with a value of 30.1 percent compared to an average of F80Hi-DD-1 and F80Hi-DD-3 of 42.5 percent.

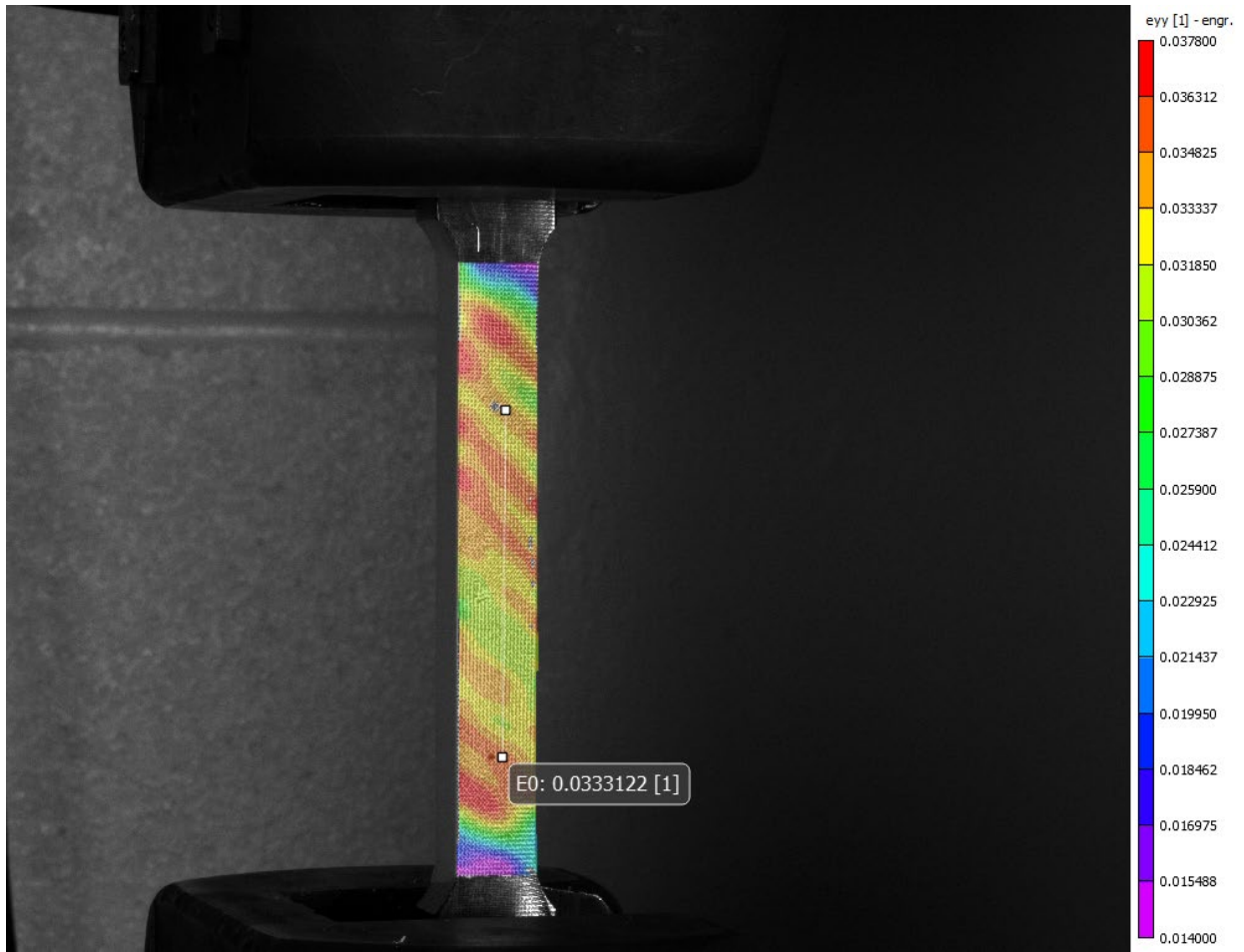


Source: FHWA.

**Figure 26. Photo. Internal discontinuity (circled) in gauge length of F80Hi-DD-2.**

### *Other Observations*

After yield, the layers of the 45 and BD specimens were visible in the strain field captured by the DIC. Figure 27 shows layers visible in the strain field of specimen F80Hi-45-2 and Figure 28 shows layers visible in the strain field of specimen F80Lo-BD-3.



Source: FHWA.

**Figure 27. Graph. Contours of specimen F80Hi-45-2 showing the AM layers visible in the engineering  $e_{yy}$  (vertical direction of figure) strain field.**



Source: FHWA.

**Figure 28. Graph. Contours of specimen F80Lo-BD-3 showing the AM layers visible in the engineering  $e_{yy}$  (vertical direction of photo) strain field.**

### Impact Testing (Charpy V-Notch)

#### *Isotropy/Anisotropy in Results*

The DD specimens generally had greater predicted absorbed energies from the sigmoid fits than their BD counterparts, except wall F80Lo at temperatures greater than 10 degrees F.

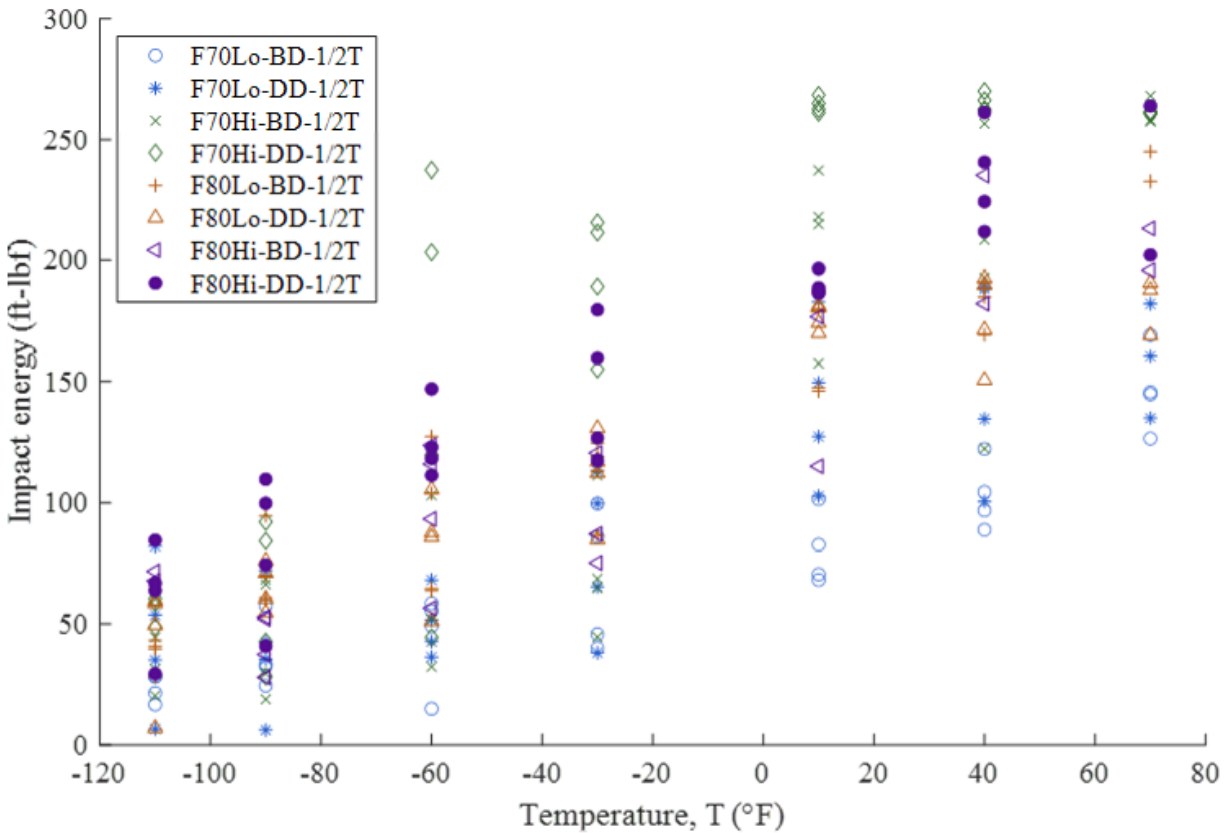
Table 31 summarizes the ratios between the average absorbed energies in the BD and DD. Most of the ratios for the F70Lo, F70Hi, and F80Hi specimens are less than 1.0, meaning that the impact energy in the BD was less than that in the DD. The majority of the ratios for these walls were less than 0.9, indicating that the behavior may be anisotropic. Most of the ratios for the F80Lo wall were greater than 1.0, meaning that the impact energy in the BD was greater than that in the DD. The majority of the ratios for this wall were between 0.9 and 1.1, indicating more isotropic behavior.

**Table 31. Ratios between the average absorbed energies of the BD and DD specimens for each wall.**

Wall ID	Temperature (°F)	Average Impact Energy Ratio, BD/DD
F70Lo	-110	0.53
F70Lo	-90	0.95
F70Lo	-60	0.90
F70Lo	-30	0.86
F70Lo	10	0.57
F70Lo	40	0.67
F70Lo	70	0.92
F70Hi	-110	0.70
F70Hi	-90	0.74
F70Hi	-60	0.49
F70Hi	-30	0.37
F70Hi	10	0.78
F70Hi	40	0.74
F70Hi	70	1.00
F80Lo	-110	0.87
F80Lo	-90	1.09
F80Lo	-60	1.09
F80Lo	-30	1.00
F80Lo	10	0.94
F80Lo	40	1.04
F80Lo	70	1.31
F80Hi	-110	1.14
F80Hi	-90	0.52
F80Hi	-60	0.78
F80Hi	-30	0.65
F80Hi	10	0.77
F80Hi	40	0.89
F80Hi	70	0.88

***Comparison of Interpass Temperature Effects Between ER70S-6 and ER80S-Ni1***

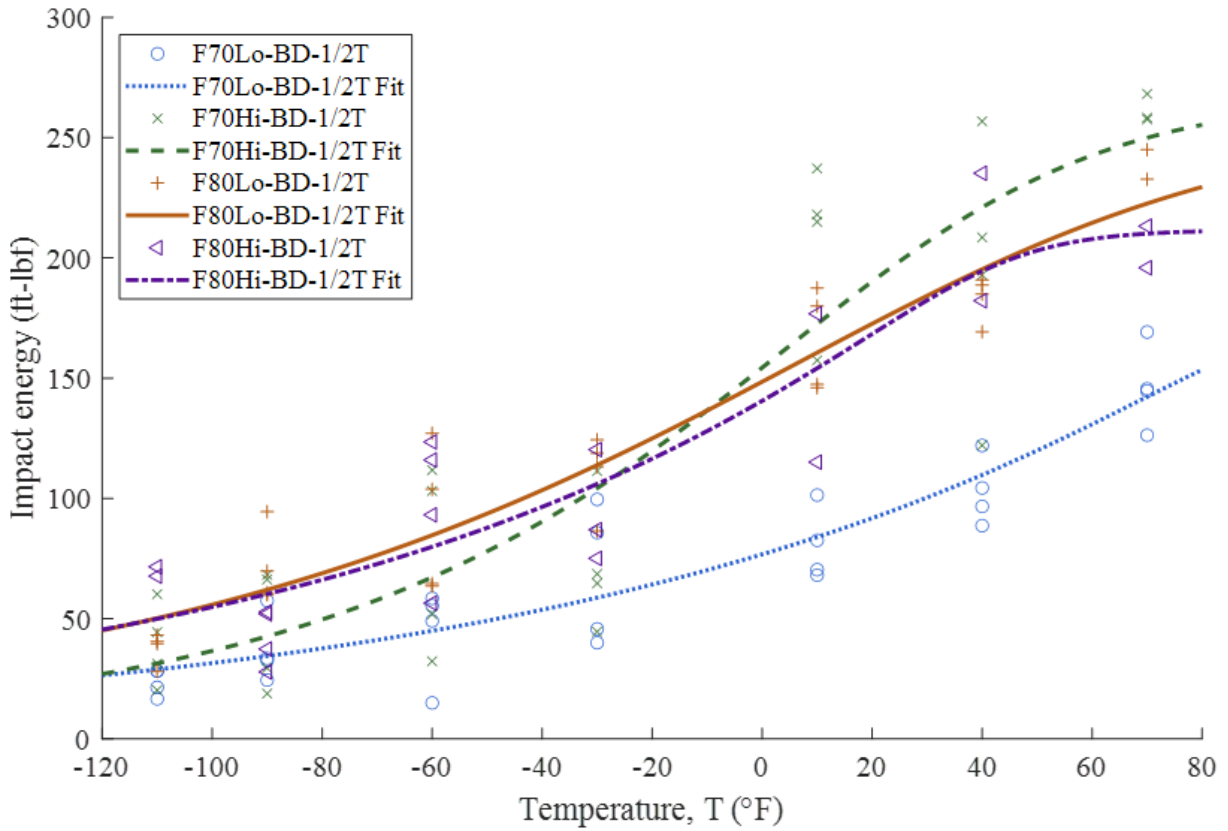
Figure 29 plots the temperature versus absorbed energy for all  $1/2 T$  specimens from all walls. The lowest temperature tested, -110 degrees F, had the lowest scatter between all walls and all directions with a range of 77.8 ft-lbf. The highest scatter was observed at -60 degrees F with a range of 222.4 ft-lbf. In general, the F70Lo-BD specimens had the lowest absorbed energies overall and F70Hi-DD had the highest absorbed energies. The F80 walls typically had absorbed energies between the two F70 walls.



Source: FHWA.

**Figure 29. Graph. Temperature versus impact energy for all  $1/2 T$  specimens from all walls.**

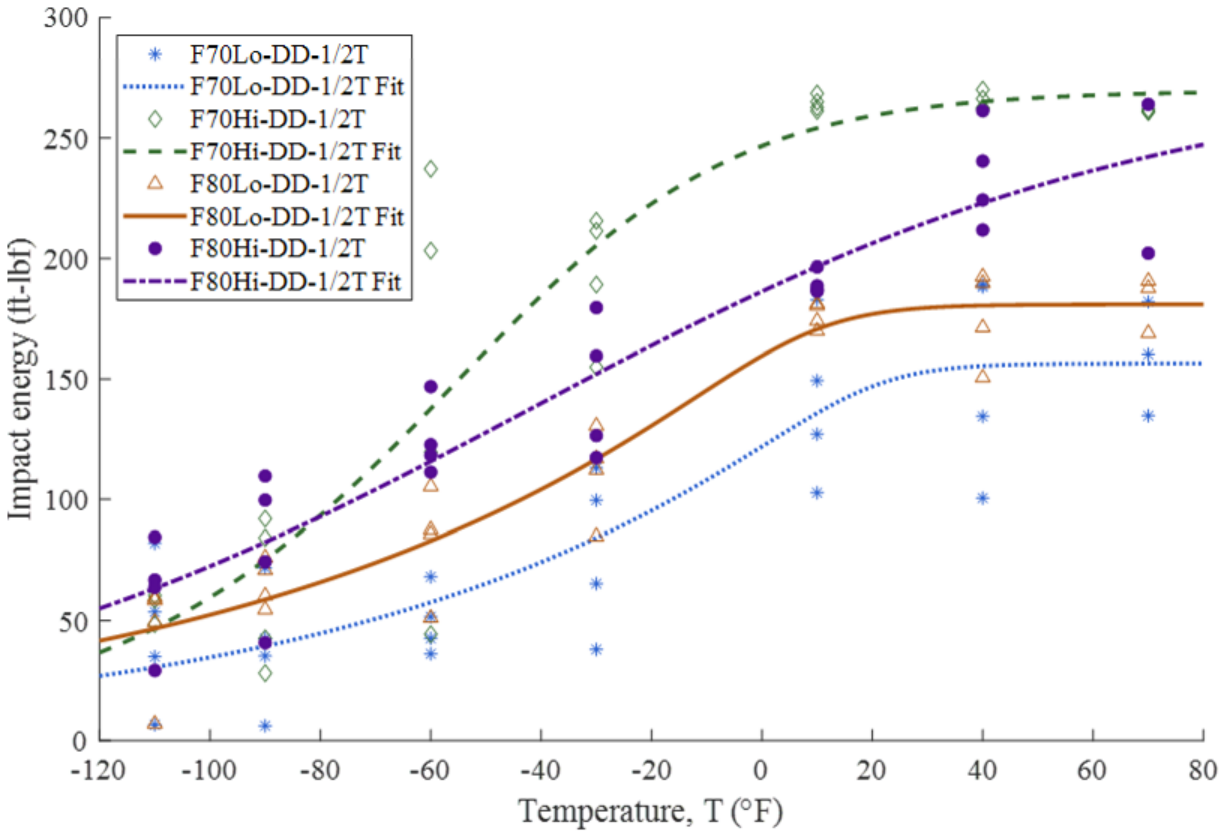
Figure 30 and Figure 31 show the temperature versus absorbed energy for BD  $1/2 T$  and DD  $1/2 T$  specimens and their sigmoid fits, respectively. The sigmoid fits of the DD specimens from walls F70Lo, F70Hi, and F80Lo show similar trends to each other. They have the distinct upper and lower shelves expected from body centered cubic metals and all appear to have a ductile-to-brittle transition temperature between -90 degrees F and 10 degrees F. The sigmoid fits of the BD specimens from walls F70Lo, F70Hi, and F80Lo also show similar trends to each other. They do not have distinct upper shelves over the range of temperatures tested and do not have an obvious ductile-to-brittle transition temperature. Wall F80Hi demonstrates the opposite behavior, a distinct upper shelf is not observed in the DD specimens over the range of temperatures tested but is observed in the BD specimens. The DD specimens do not demonstrate any clear trend regarding the F70 versus F80 specimens resulting in higher absorbed energies. Generally, the F80 DD specimens have absorbed energies between the absorbed energies of the F70Lo and F70Hi DD specimens.



Source: FHWA.

**Figure 30. Graph. Temperature versus impact energy for BD  $1/2 T$  specimens from all walls.**

The higher interpass temperature generally yielded higher impact energies than the corresponding lower interpass temperature. For the BD specimens, both high interpass temperature sets of specimens showed distinct upper shelves, whereas the low interpass temperature sets of specimens did not. For the DD specimens, the same correlation between the interpass temperature and the presence of an upper shelf does not exist.



Source: FHWA.

**Figure 31. Graph. Temperature versus impact energy for DD  $1/2$  T specimens from all walls.**

### *Comparison to Literature*

In addition to the results presented in this report, 11 additional studies from the literature were identified that quantified the impact properties of ER70S-6 WAAM steel. Most studies evaluated tensile specimens in at least two directions of the build. These directions correspond to the longitudinal axis of the notch parallel to the BD and the longitudinal axis of the notch parallel to the DD (i.e., perpendicular to the BD).

As previously stated, the welding process parameters can influence the material properties of the as-fabricated WAAM material. The wire diameter, voltage, current range, wire feed rate, print travel speed, approximate heat input, and shielding gas mixture used in the studies from the literature are synthesized in Table 32. Note, not all process parameters were reported for all studies including the current study in which the specific details of the welding process are proprietary to the service provider. The table also describes any unique variables (e.g., bead oscillation pattern, surface finish, etc.) investigated in each study.

**Table 32. Welding process parameters for CVN tests on WAAM ER70S-6 from the literature.**

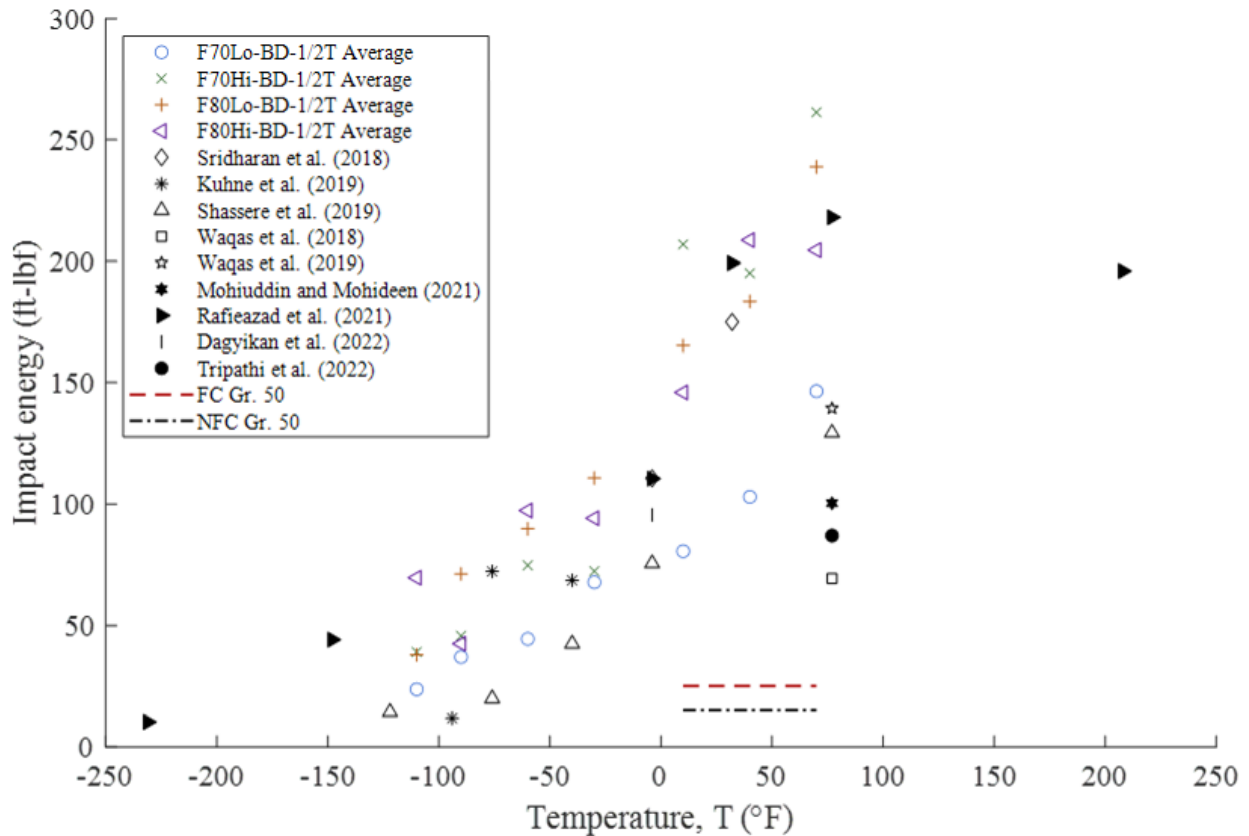
Reference	Process Notes	Wire Diameter (in)	Voltage (V)	Current Range (A)	Wire Feed Rate (ft/min)	Print Travel Speed (in/min)	Welding Heat Input (kJ/in)	Shielding Gas Composition (percent)
Sridharan et al. (2018) [33]	—	—	—	230-270	—	—	—	—
Kuhne et al. (2019) [61]	—	0.039	27	255	—	15.7	26.3	92 Ar / 8 CO2
Shassere et al. (2019) [62]	—	—	15.7	160	16.7	16.0	9.4	95 Ar / 5 CO2
Waqas et al. (2018) [63]	—	—	—	—	—	—	—	—
Waqas et al. (2019)^ [39]	—	0.047	19	120	—	8.27	16.5	—
Douglass and Schaeffer (2021)* [49]	Fast Cooling Rate	—	—	—	—	—	10.0	—
Douglass and Schaeffer (2021)* [49]	Slow Cooling Rate	—	—	—	—	—	27.0	—
Mohiuddin and Mohideen (2021) [64]	—	0.047	26-28	130-150	8.2	9.8-11.8	20.6-21.4	100 CO2
Nagasai et al. (2021) [50]	—	—	18.3	227	22.0	15.7	15.8	85 Ar / 15 CO2
Rafiezzad et al. (2021) [51]	—	0.035	—	—	—	—	—	—
Dagyikan et al. (2022) [65]	—	0.047	18	185	15.4	20.1	9.9	82 Ar / 18 CO2
Tripathi et al. (2022) [60]	GTAW	0.031	—	80	2.6	—	—	99 Ar
Current Study	Lo interpass temperature	0.045	—	—	—	—	15.0*	90 Ar / 10 CO2
Current Study	Hi interpass temperature	0.045	—	—	—	—	14.5*	90 Ar / 10 CO2

— no data was reported.

^Subsize specimens of one-half thickness were tested.

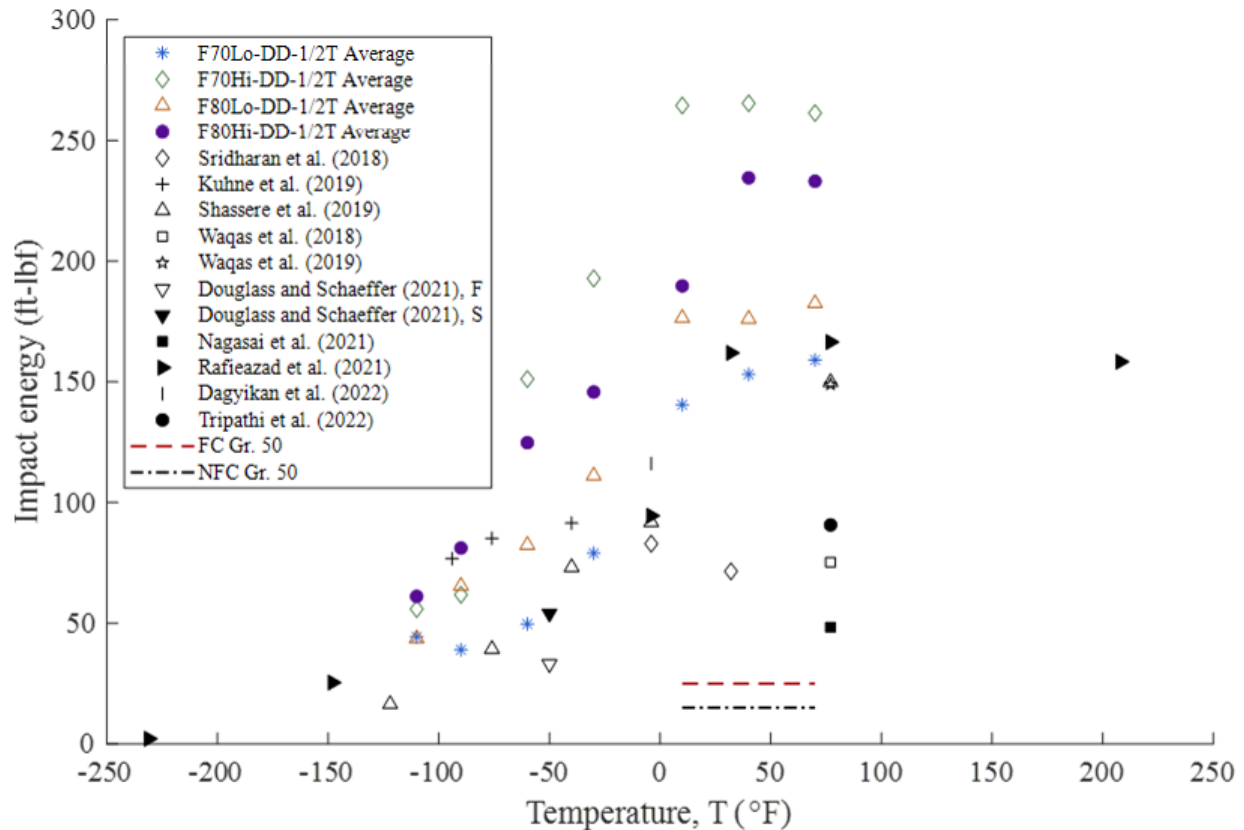
\*Specimens were one-third of full size. Impact energies were not adjusted to equivalent full-size impact energies.

Figure 32 and Figure 33 show the temperature versus average absorbed energy for DD  $1/2 T$  and BD  $1/2 T$  specimens, respectively, compared to the data available from the literature. BD specimen averages from the literature from 40 degrees F and lower fell closely outside or within the range of specimen averages from the current study. At higher than 40 degrees F the averages from the literature were lower than what would be expected from an extrapolation of the specimen averages from the current study. DD specimen averages from the literature from 10 degrees F and lower fell closely outside or within the range of specimen averages from the current study. At higher than 10 degrees F the averages from the literature were lower than what would be expected from an extrapolation of the specimen averages from the current study. All specimens from the literature tested above 0 degrees F exceeded the AASHTO requirements.



Source: FHWA.

**Figure 32. Graph. Temperature versus average impact energy for all BD  $1/2 T$  specimens from all walls compared to BD specimens from the literature.**



Source: FHWA.

Note: Both types of specimens tested by Douglass and Schaeffer were one-third size. Their impact energies have not been converted to equivalent full-size impact energies.

**Figure 33. Graph. Temperature versus average impact energy for all DD  $1/2 T$  specimens from all walls compared to DD specimens from the literature.**

## Fatigue Testing

### *Impact of Surface Roughness*

The as-built specimens demonstrated lower fatigue performance than the machined specimens compared to the AASHTO detail category S-N curves. All machined specimens exceeded AASHTO fatigue detail category A, with all tested specimens considered runouts. Conversely, except for one specimen, the tested values of the as-built specimens exceeded the design life design curve for detail category C.

The Lo-AB specimens demonstrated slightly lower fatigue performance than the Hi-AB specimens. However, the small number of specimens evaluated could not quantify the marginal difference. Additionally, the average notch depth for both types of specimens was the same and the failure notch depth for both types of specimens were similar (Table 23). In general, there does not appear to be a difference in surface finish or performance that would warrant a change in the fatigue category based on the interpass temperature; therefore, regression analyses were performed that treated both Hi- and Lo-AB specimens as part of one dataset.

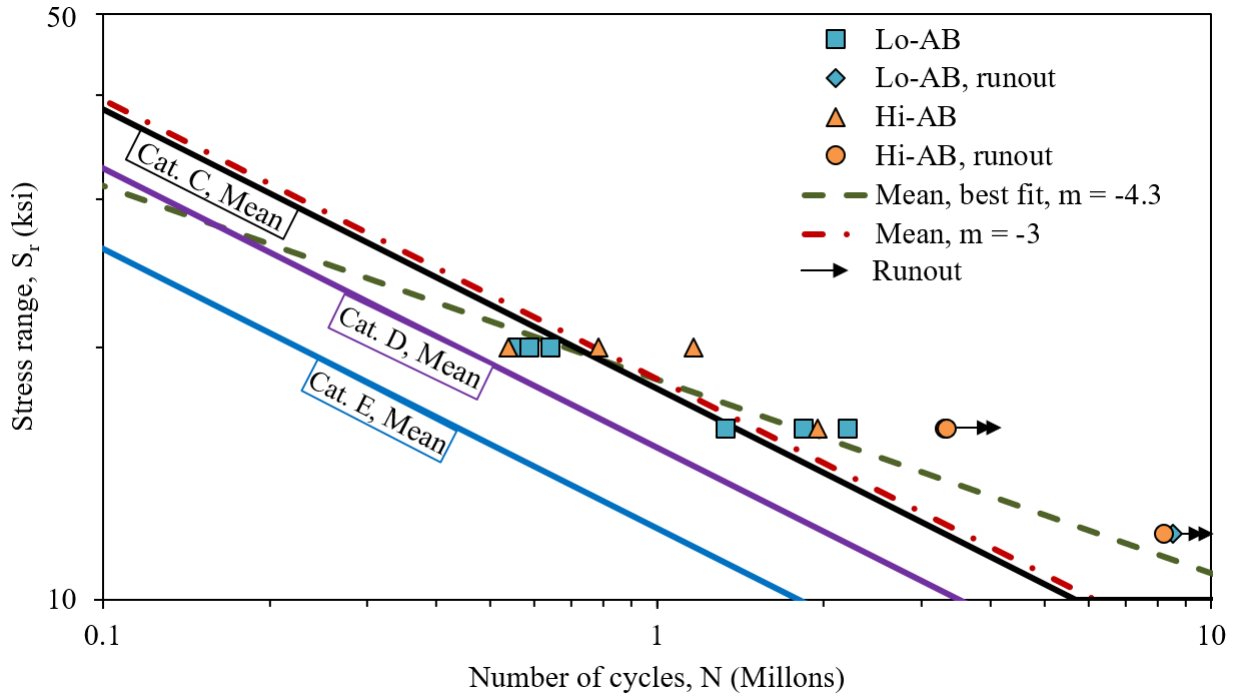
A best fit log-log regression for the mean of the AB specimens tested was determined by a linear least squares approach excluding all runouts in keeping with previous studies and the form of AASHTO Equation 6.6.1.2.5-2 [103]. The best fit regression was adjusted to a two tailed 95 percent confidence limit (CL) by shifting the value of the detail constant,  $A$ , down by 1.96 standard deviations (SD). It has been shown by regression analysis that as the sample size for a detail category increases, the slope of the S-N curve,  $m$ , tends to converge to a value of -3.0 [104]. For this reason, and for direct comparison to the AASHTO detail category S-N curves, a best fit log-log regression was also performed with  $m$  fixed to a value of -3.0. The slope fixed regression was also adjusted down to a 95 percent CL. The 95 percent CL regression with a slope of -3.0 falls between the design life regressions for category C and category D, thus the AM AB finish would be a category D detail. Table 33 presents the  $A$ ,  $m$ , and  $R^2$  values for each regression generated. Figure 34 presents the S-N values for all tested AB specimens and experimental regressions compared to mean life AASHTO detail categories. Figure 35 presents the S-N values for all tested AB specimens and experimental regressions compared to design life AASHTO detail categories.

A similar regression for the M specimens was unnecessary as the specimens were considered runouts shortly after they exceeded the adjusted maximum life for category A. As a result, the slope,  $m$ , was forced to equal -3.0 and the mean of the tested specimens to fall on the design life curve for detail category A (Figure 36). The design life curve for detail category A has a detail constant,  $A$ , of  $250 \times 10^8$ .

**Table 33. Detail constants, slope, and  $R^2$  value for fatigue regressions for AB specimens.**

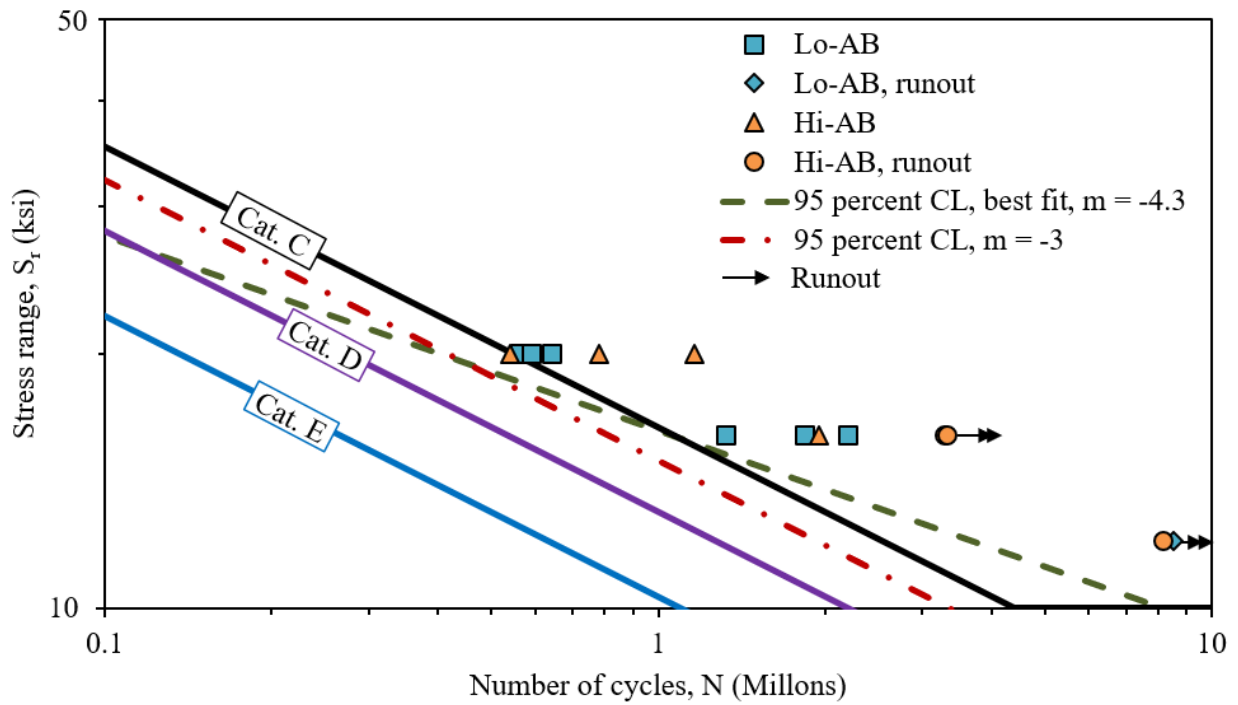
Regression Type	Slope, $m$	Detail constant, $A$	$R^2$
Best fit, mean	-4.3	$2,900 \times 10^8$	0.80
Best fit, 95 percent CL	-4.3	$1,730 \times 10^8$	N/A
Slope fixed, mean	-3	$61.8 \times 10^8$	0.72
Slope fixed, 95 percent CL	-3	$33.6 \times 10^8$	N/A

“N/A” indicates an  $R^2$  value was not applicable for the given regression type.



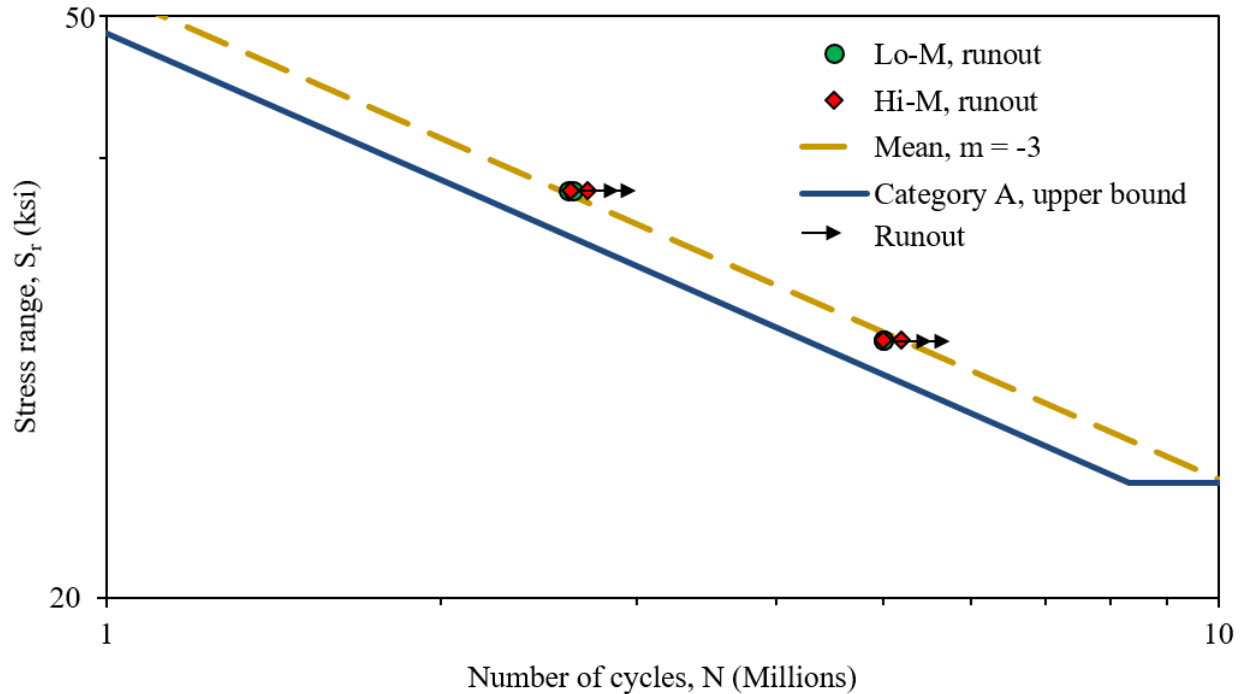
Source: FHWA.

**Figure 34. Graph. S-N plot of as-built specimen data and corresponding mean regressions compared to mean life AASHTO detail categories.**



Source: FHWA.

**Figure 35. Graph. S-N plot of as-built specimen data and corresponding 95 percent confidence interval regressions compared to design life AASHTO detail categories.**



Source: FHWA.

**Figure 36. Graph. S-N plot of machined specimen data and mean regression compared to the upper bound of AASHTO detail category A.**

### *Comparison of Results to Literature*

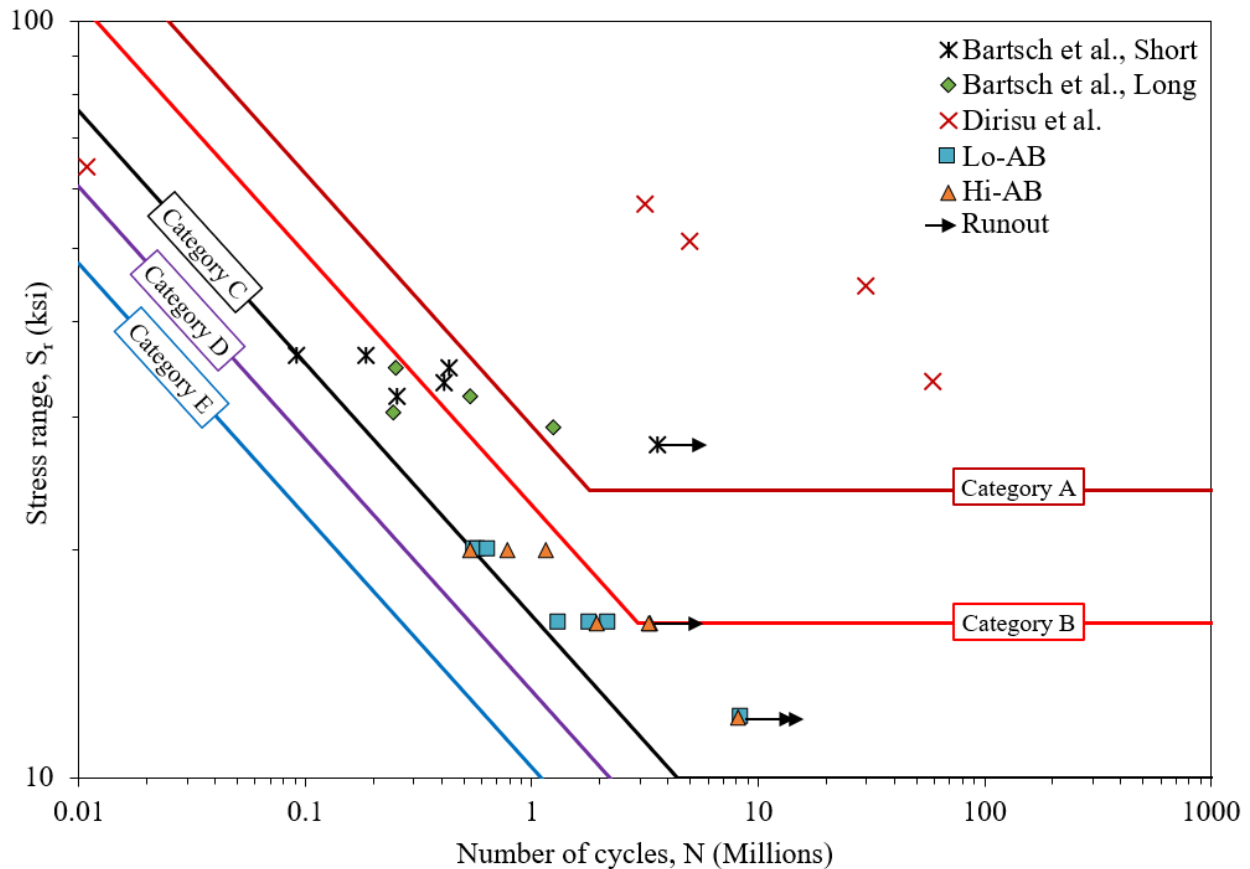
Table 34 shows the welding process and test parameters for fatigue tests from the available literature compared to the parameters of the current study, note that only mode I load cases were included. Figure 37 shows the stress range and number of cycles for each as-built specimen tested in the current study compared to the results of as-built tests conducted by Bartsch et al. (2021) and Dirisu et al. (2020), including the AASHTO detail categories A-E. Figure 38 shows the stress range and number of cycles for each machined specimen tested in the current study compared to the results of machined tests conducted by Dirisu et al. (2020), Ron et al. (2020), Smismans et al. (2021), Ayan and Kahraman (2022), and Ermakova et al. (2023). Note, Dirisu et al. (2020) tested at some stress ranges that exceeded the 43.5 ksi and 50.8 ksi yield strengths reported for their as-built and machined materials. The R-ratio reported was 0.1; as such, the specimens tested at stress ranges above the reported yield strengths would have been continually yielded during the fatigue testing.

**Table 34. Welding process and specimen parameters for available fatigue tests on WAAM ER70S-6 in the literature.**

Reference	Process Notes	Voltage (V)	Wire Diameter (in)	Current Range (A)	Wire Feed Rate (ft/min)	Print Travel Speed (in/min)	Welding Heat Input (kJ/in)	Shielding Gas Composition	Type of Test	Specimen Surface Finish	R-Ratio
Ron et al. (2020) [66]	—	24	0.047	210	20.0	5.5	54.6	98 Ar / 2 O <sub>2</sub>	Rotating beam	Machined	—
Dirisu et al. (2020) [67]	Cold metal transfer	—	0.039	—	13.1	1.3	—	80 Ar / 20 CO <sub>2</sub>	Uniaxial tension	As-built and Machined	0.1
Bartsch et al. (2021) [68]	—	27	0.039	255	—	15.7	26.3	92 Ar / 8 CO <sub>2</sub>	Uniaxial tension	As-built	0.1
Smismans et al. (2021) [69]	—	19	0.047	174	14.8	13.4	14.8	85 Ar / 15 CO <sub>2</sub>	Rotating beam	Machined	—
Ayan and Kahraman (2022) [54]	—	17-19	0.047	105-120	6.6	0.5	217.7-278.0	86 Ar / 12 CO <sub>2</sub> / 2 O <sub>2</sub>	Bending	Machined	—
Ermakova et al. (2023) [70]	Cold metal transfer	—	0.047	—	24.6	1.4	—	80 Ar / 20 CO <sub>2</sub>	Uniaxial	Machined	0.1
Current Study	Low interpass temperature	—	0.045	—	—	—	15.0*	90 Ar / 10 CO <sub>2</sub>	Uniaxial tension	Machined	0.1-0.25
Current Study	High interpass temperature	—	0.045	—	—	—	14.5*	90 Ar / 10 CO <sub>2</sub>	Uniaxial tension	Machined	0.1-0.25

— no data was reported.

\*Average of heat inputs from inner and outer beads of each layer

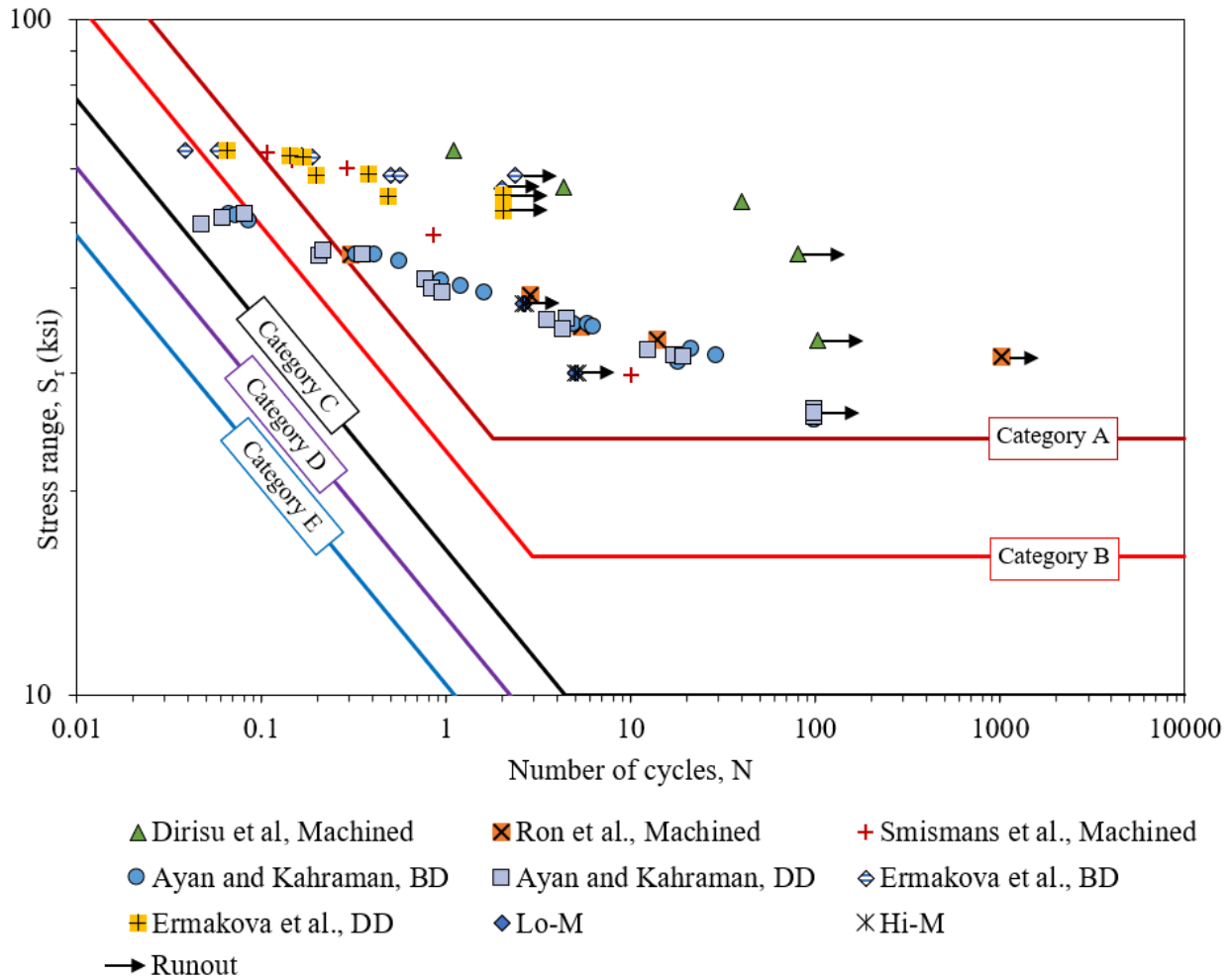


Source: FHWA.

**Figure 37. Graph. S-N values for each as-built specimen tested compared to as-built surface finish specimens from the literature and AASHTO detail categories A-E.**

In general, the results of the as-built fatigue tests from the literature satisfied the minimum number of cycles of AASHTO detail category C for their corresponding stress ranges, except for Dirisu et al.'s specimens tested at a stress range of 64.0 ksi and one of Bartsch et al.'s specimens tested at a stress range 36.3 ksi. Bartsch et al.'s specimens performed similarly to an extrapolation of the results from the current study. The performance of Dirisu et al.'s specimens was much greater than expected if the slope of the Lo and Hi specimen results of the current study were extrapolated, which may be due to the yielding of the specimens during fatigue testing.

Similar to all Lo and Hi specimens of the current study, all machined specimens from the literature tested at or below a stress range of 40 ksi exceeded the minimum number of cycles of AASHTO detail category A. The worst-performing specimens from the literature were tested between a 40 and 70 ksi stress range, exceeding the minimum number of cycles of AASHTO detail category C.



Source: FHWA.

**Figure 38. Graph. S-N values for each machined specimen tested compared to machined surface finish specimens from the literature and AASHTO detail categories A-E.**

### *Effects of Internal Discontinuities*

Fatigue performance exceeding the minimum of detail category A was observed in all machined specimens included in Figure 22 and Table 22. Specimen Lo-M-7 (Figure 39), which was not included in the dataset, broke in the grip length due to an internal pore discontinuity in that region at 702,071 cycles at a nominal stress range of 38 ksi in the gauge length. No other tested specimens were observed to have any effects from internal discontinuities.



Source: FHWA.

**Figure 39. Photo. Failure surface of specimen Lo-M-7 showing pores at the initiation edge.**

## CHAPTER 5: WAAM APPLICATIONS IN TRANSPORTATION SECTOR

As previously stated, some of the benefits of WAAM are that it is capable of producing complex geometries that can result from structural optimization, creating small runs of unique components, and fabricating large-scale parts. One other distinct advantage of WAAM is that the designer can modify the geometry (e.g., selectively thicken, radius gussets, etc.) to control the cyclic stress range. As such, if a WAAM design exceeds category D for fatigue, designers may be able to change the geometry to reduce the stress range and maintain the as-built surface finish. However, there may be instances where the geometry cannot be sufficiently altered; in such cases, machining the as-built surface finish may be necessary to achieve the appropriate fatigue performance.

Several potential WAAM applications were identified within the transportation sector based on the advantages of WAAM and the results of the tension, impact, and fatigue testing conducted in the current study. This list of components or applications (Table 35) was created by considering a variety of factors, including current state of WAAM technology, perceived risk by owners, loading scenario complexity, benefits to optimization, fabrication difficulty by traditional means, uniqueness, and component repetition. The opportunities and challenges for each application are included along with a score (i.e., 1, 2, or 3) for traditional fabrication difficulty and for benefit to optimize. Scores of 1, 2, and 3 represent low, medium, and high traditional fabrication difficulty or benefit to optimize, respectively. The components or applications listed in Table 35 are ordered by the sum of the fabrication and optimization scores.

**Table 35. List of potential components or applications for WAAM in the transportation sector.**

Component or Application	Opportunities	Challenges	Traditional Fab. Difficulty Score*	Benefit to Optimize Score*	Sum
Cable saddle (suspension bridge)	<ul style="list-style-type: none"> <li>• A limited number of unique saddles are required for each bridge</li> <li>• Stiffener size/spacing can be fully optimized</li> <li>• Time-intensive traditional fabrication</li> </ul>	<ul style="list-style-type: none"> <li>• May be difficult to gain owner approval given the importance of each component, even considering the requirement of Post-Tensioning Institute (PTI) DC45.1 that a design must consider the loss of one cable</li> <li>• Good long-term opportunity, may be too big of a leap for a first step given complexity and rarity of the structure type</li> </ul>	3	3	6
Rapid prototyping	<ul style="list-style-type: none"> <li>• Test fully optimized WAAM component geometry prior to creating a casting; avoid the need for a large quantity of parts with casting initially</li> </ul>	<ul style="list-style-type: none"> <li>• The performance of WAAM has not been compared to the performance of castings; this would be necessary to show that the WAAM and cast components have similar performance</li> </ul>	3	3	6
Stay cable anchorage	<ul style="list-style-type: none"> <li>• Angle between cable and deck at intersection can be small, leading to tight access for welder and inspector</li> <li>• Each connection can be unique (depending on cable layout)</li> <li>• Stiffener size/spacing can be fully optimized</li> <li>• Time-intensive traditional fabrication</li> </ul>	<ul style="list-style-type: none"> <li>• May be difficult to gain owner approval given the importance of each component, even considering the requirement of PTI DC45.1 that a design must consider the loss of one cable</li> <li>• Good long-term opportunity, may be too big of a leap for a first step given complexity and rarity of the structure type</li> </ul>	3	3	6
Stiffened steel (waffle) hanger connection	<ul style="list-style-type: none"> <li>• Stiffeners can be spaced closely together, leading to tight access for the welder</li> <li>• Each hanger can be unique (depending on cable layout)</li> <li>• Stiffener size/spacing can be fully optimized</li> <li>• Use of selective web and/or stiffener thickening can optimize overall design</li> <li>• Time-intensive traditional fabrication</li> </ul>	<ul style="list-style-type: none"> <li>• May be difficult to gain owner approval given the importance of each component, even considering the requirement of PTI DC45.1 that a design must consider the loss of one cable</li> <li>• Good long-term opportunity, may be too big of a leap for a first step given complexity and rarity of the structure type</li> </ul>	3	3	6

Component or Application	Opportunities	Challenges	Traditional Fab. Difficulty Score*	Benefit to Optimize Score*	Sum
TKY connection (tubular members)	<ul style="list-style-type: none"> <li>Member connection angles can be small, leading to tight access for the welder and inspector</li> <li>Time-intensive traditional fabrication</li> <li>Ability to connect to a node rather than directly to other members</li> <li>Enables automated circumferential welding of connection members</li> </ul>	<ul style="list-style-type: none"> <li>Traditional fabrication is not as difficult as some other applications</li> </ul>	2	3	5
Movable bridge casting replacement	<ul style="list-style-type: none"> <li>WAAM replacement part lead times can be faster than casting lead times</li> <li>WAAM may be more cost-effective for small numbers of parts (like a replacement scenario) than casting</li> </ul>	<ul style="list-style-type: none"> <li>Loading scenario may not be complex (e.g., sheave hard facing), may not demonstrate the ability of WAAM to optimize</li> <li>Hard-facing electrodes have not yet been used for WAAM</li> </ul>	3	2	5
Cross-frame	<ul style="list-style-type: none"> <li>Fabricate one integrated structure with WAAM rather than joining traditional members</li> <li>Time-intensive traditional fabrication</li> </ul>	<ul style="list-style-type: none"> <li>Traditional fabrication is not as difficult as some other applications</li> <li>More repetition of components than other applications</li> </ul>	2	2	4
Functionally-graded bearing	<ul style="list-style-type: none"> <li>Construct a bearing that uses corrosion-resistant steel on the outside and mild steel on the inside</li> <li>Improve wear resistance through use of hard-facing material</li> <li>Can demonstrate how the two materials behave together</li> </ul>	<ul style="list-style-type: none"> <li>Loading scenario is not complex and may not demonstrate the ability of WAAM to optimize</li> <li>Limited material characterization for functionally-graded materials</li> <li>Bearings for new bridges tend to be “off the shelf” components</li> </ul>	2	2	4
Traffic structure base plate to tube wall connection	<ul style="list-style-type: none"> <li>Subject to frequent fatigue failures</li> <li>Stress flow can be optimized to minimize the stress concentration at the base through selective thickening and integrated stiffeners</li> <li>Unique retrofit solutions possible for existing structures.</li> </ul>	<ul style="list-style-type: none"> <li>Large quantity of structures in service</li> <li>WAAM may only be needed for prototyping, it may be more cost-effective to produce subsequent components by castings</li> <li>Traditional fabrication is not difficult</li> </ul>	1	3	4

Component or Application	Opportunities	Challenges	Traditional Fab. Difficulty Score*	Benefit to Optimize Score*	Sum
Truss node (non-tubular members)	<ul style="list-style-type: none"> <li>Member orientations can be varied more than traditional construction because WAAM is capable of producing many unique parts</li> <li>Move the connection between the node and the member (welded or bolted) out of the center of the connection by extending the node elements</li> <li>Thickness can be varied with force demand</li> </ul>	<ul style="list-style-type: none"> <li>These types of nodes are currently uncommon; only one known gusset-less bridge (Memorial Bridge, NH, USA)</li> </ul>	2	2	4
Bearing replacement	<ul style="list-style-type: none"> <li>Shim height can range from several inches to multiple feet</li> <li>Multiple shim heights can be required on a single bridge</li> </ul>	<ul style="list-style-type: none"> <li>Loading scenario is not complex and may not demonstrate the ability of WAAM to optimize</li> <li>Traditional fabrication is not as difficult as some other applications</li> </ul>	2	1	3
In-situ damage repair	<ul style="list-style-type: none"> <li>In-situ, customized WAAM damage repair (e.g., corrosion, impact, etc.) could provide an innovative alternative to existing approaches (e.g., UHPC, heat straightening, etc.)</li> <li>May not need to remove traffic from the structure during a repair</li> </ul>	<ul style="list-style-type: none"> <li>WAAM in-situ performance has not yet been demonstrated</li> <li>Development required for WAAM fabrication on an uneven surface</li> <li>Loading scenario is not complex and may not demonstrate the ability of WAAM to optimize</li> </ul>	2	1	3
Beam Cladding	<ul style="list-style-type: none"> <li>Clad the end of mild steel beam with corrosion-resistant steel</li> </ul>	<ul style="list-style-type: none"> <li>Loading scenario is not complex and may not demonstrate the ability of WAAM to optimize</li> <li>Traditional fabrication and coating systems are not difficult and can exhibit reasonable performance if maintained properly</li> </ul>	1	1	2

\*Scores of 1, 2, and 3 represent low, medium, and high traditional fabrication difficulty or benefit to optimize, respectively.

## CHAPTER 6: CONCLUSIONS AND SUGGESTIONS

### CONCLUSIONS

The following sections outline the conclusions drawn through the work described within this report.

#### Tension Testing

- No significant anisotropy was observed in the yield and tensile strengths of the WAAM material resulting from both wire types and both interpass temperatures. The existing literature on WAAM ER70S-6 further supports this conclusion.
- Percent elongation at fracture is significantly influenced by the specimen and load orientation with respect to the build (BD) and deposition (DD) directions. The specimens with gauge lengths and loading parallel to the deposition direction generally had higher percent elongations at fracture than those with gauge lengths and loading parallel to the build direction and those at a 45-degree angle between the build and deposition directions.
- The minimum yield and tensile strength requirements of AWS A5.18 for ER70S-6 were met by most of the F70Lo specimens but none of the F70Hi specimens. The minimum yield and tensile strength requirements of AWS A5.28 for ER80S-Ni1 were not met by any of the F80Lo or F80Hi specimens.
- The ER70S-6 and ER80S-Ni1 WAAM materials produced with a low interpass temperature had higher yield and tensile strengths than their counterparts with high interpass temperatures. However, as in the above elongation at fracture results, the lower interpass temperature specimens were less ductile than the high interpass temperature specimens on average.
- Internal discontinuities outside of a section's critical area may not impact the yield and tensile strength and percent elongations at fracture of WAAM material. An internal discontinuity of 5.5 percent of the reduced area at failure did not appear to influence the yield and tensile strength properties of ER80S-Ni1 WAAM material. However, the elongation at fracture was reduced by approximately 23 percent. It should be noted that only one specimen was tested that failed with a discontinuity on the fracture surface; therefore, the results may not be representative of a larger sample size of specimens containing defects. The walls fabricated for the current study were the first that fabricator used ER80S-Ni1 weld wire for WAAM.

## Impact Testing (Charpy V-Notch)

- All impact specimens tested exceeded the AASHTO Grade 50 fracture critical and non-fracture critical limits for all service temperatures.
- The BD over DD impact energy ratios for the F70Lo, F70Hi, and F80Hi walls were generally less than 0.9 for the majority of temperatures, suggesting that their impact energy behavior may be anisotropic. The BD over DD impact energy ratios for the F80Lo wall were generally between 0.9 and 1.1, suggesting that this wall had more isotropic behavior.
- There was less scatter between the results for all walls at lower temperatures, with the lowest range of 73 ft-lbf observed at -110 degrees F. The highest range of 222.4 ft-lbf was observed at -60 degrees F. Generally, the F70Lo-BD specimens had the lowest absorbed energies, and the F70Hi-DD had the highest absorbed energies.
- The F70Lo, F70Hi, and F80Hi BD specimens did not show a distinct upper shelf over the range of temperatures tested. The F70Lo, F70Hi, and F80Hi DD specimens did show distinct upper and lower shelves. This trend is reversed for the F80Lo specimens.
- Tests from the literature fell within or close to the range of the tests from the current study at temperatures less than 40 degrees F.

## Fatigue Testing

- The as-built specimens demonstrated lower fatigue performance as compared to the machined specimens. All but one as-built specimen tested exceeded the AASHTO detail category C design life. The tested machined specimens exceeded the AASHTO detail category A design life and ran out the upper bound life.
- The notch depth and performance of the Lo-AB and Hi-AB specimens were similar.
- The slope of the best-fit regression of the combined AB dataset was equal to 4.3, different than what AASHTO Equation 6.6.1.2.5-2 prescribes.
- When the 95 percent confidence interval regression slope was fixed to 3.0 to strictly follow AASHTO, the regression fell between AASHTO detail categories C and D. Thus, these would be categorized as Category D fatigue details. For this research, this fatigue resistance was attained with a surface roughness measured at  $R_a=7$  mils or  $R_t=36$  mils.
- The as-built fatigue tests from the literature do not conclusively agree or disagree with the AASHTO detail categories met by the tests from the current study.
- The machined fatigue tests from the literature tested below a stress range of 40 ksi exceed the minimum number of cycles of AASHTO detail category A, in agreement

with the tests from the current study. Above a stress range of 40 ksi, the minimum number of cycles of AASHTO detail category A was not always exceeded in the literature.

- Internal discontinuities, even in machined specimens, may result in a reduction in fatigue performance.

## **SUGGESTED FUTURE WORK**

A list of potential components and applications of WAAM in the transportation sector was generated based on the conclusions of the current study and the various advantages of WAAM. The components and applications (Table 35) balance a variety of considerations when selecting a WAAM demonstration (i.e., current state of WAAM technology, perceived risk by owners, loading scenario complexity, benefits to optimization, fabrication difficulty by traditional means, uniqueness, and component repetition). Evaluating any of the components or applications for steel bridge and highway structures would provide insights regarding the as-fabricated structural performance for large-format WAAM in the transportation sector. Once a component or application of WAAM for steel bridge or highway structures has been selected, topology optimization of the component or application should be performed to evaluate the unique opportunities afforded by AM. The results of this optimization could be used to inform a future full-scale component or member testing program.

While the results presented in the current study establish the potential of WAAM as a structural engineering material, further research is required to establish codes and guidance for in-service implementation. For example, future research is needed to establish the quality control quality assurance (QAQC) process for the manufacture of WAAM structural components, including allowable inspection techniques and inspection frequency. This research would need to include guidance regarding the use of nondestructive evaluation (NDE) on WAAM components. Future research could also expand the dataset size and explore the use of adjustment factors to the resistance factors used for design to account for the differences in WAAM properties as compared to traditional rolled material. Additionally, future research could explore the corrosion resistance of WAAM ER70S-6 and ER80S-Ni1 in its uncoated and coated conditions. Consideration would need to be given to preparing the as-built WAAM surface finish so that it could effectively receive various coatings.

## REFERENCES

- [1] T. DebRoy, H.L. Wei, J.S. Zuback, T. Mukherjee, J.W. Elmer, J.O. Milewski, A.M. Beese, A. Wilson-Heid, A. De, W. Zhang, Additive manufacturing of metallic components – Process, structure and properties, *Progress in Materials Science*. 92 (2018) 112–224. <https://doi.org/10.1016/j.pmatsci.2017.10.001>.
- [2] M. Douglass, *Addressing Production Challenges and Go-to-Market Limitations with Established Additive Manufacturing Service Providers*, 2020.
- [3] ADDere, *Getting Structural Scale Metal Parts to Market Faster: How ADDere Manufacturing dramatically reduced time and material cost by 3D printing large, high mass components*, Midwest Engineered Systems, 2021.
- [4] T. Lehmann, D. Rose, E. Ranjbar, M. Ghasri-Khouzani, M. Tavakoli, H. Henein, T. Wolfe, A. Jawad Qureshi, Large-scale metal additive manufacturing: a holistic review of the state of the art and challenges, *International Materials Reviews*. 67 (2022) 410–459. <https://doi.org/10.1080/09506608.2021.1971427>.
- [5] A. Nycz, A.I. Adediran, M.W. Noakes, L.J. Love, Large scale metal additive techniques review, in: *Proceedings of the 27th Annual International Solid Freeform Fabrication Symposium*, 2016.
- [6] American Welding Society, *AASHTO/AWS D1.5M/D1.5:2020 Bridge Welding Code*, American National Standards Institute, 2020.
- [7] ASTM International, *ASTM A709/A709M-21: Standard Specification for Structural Steel for Bridges*, 2021.
- [8] American Welding Society, *A5.18/A5.18M:2021: Specification for Carbon Steel Electrodes and Rods for Gas Shielded Arc Welding*, American National Standards Institute, 2021.
- [9] American Welding Society, *A5.28/A5.28M:2022: Specification for Low-Alloy Steel Electrodes and Rods for Gas Shielded Arc Welding*, 2020.
- [10] ASTM International, *ASTM A370-22: Standard Test Methods and Definitions for Mechanical Testing of Steel Products*, 2022.
- [11] AASHTO, *LRFD Bridge Design Specifications*, American Association of State Highway and Transportation Officials, 2020.
- [12] ASTM International, *ASTM E466-21: Standard of Practice for Conducting Force Controlled Constant Amplitude Axial Fatigue Tests of Metallic Materials*, 2021.
- [13] ISO/ASTM International, *ISO/ASTM 52900: Additive Manufacturing-General Principles, Fundamentals, and Vocabulary*, 2021.
- [14] E. Herderick, *Additive Manufacturing of Metals: A Review*, *Materials Science and Technology*. (2011).
- [15] V. Bhavar, P. Kattire, V. Patil, S. Khot, K. Gujar, R. Singh, A review on powder bed fusion technology of metal additive manufacturing, in: 2014: pp. 251–253. <https://doi.org/10.1201/9781315119106-15>.
- [16] *Technology Overview Metal Additive Manufacturing*, AMPOWER. (2019). <https://ampower.eu/infographics/metal-additive-manufacturing/> (accessed August 25, 2023).
- [17] W.E. Frazier, *Metal Additive Manufacturing: A Review*, *J. of Materi Eng and Perform*. 23 (2014) 1917–1928. <https://doi.org/10.1007/s11665-014-0958-z>.
- [18] J.J. Lewandowski, M. Seifi, *Metal Additive Manufacturing: A Review of Mechanical Properties*, *Annu. Rev. Mater. Res*. 46 (2016) 151–186. <https://doi.org/10.1146/annurev-matsci-070115-032024>.

- [19] S.W. Williams, F. Martina, A.C. Addison, J. Ding, G. Pardal, P. Colegrove, *Wire + Arc Additive Manufacturing, Materials Science and Technology*. 32 (2016) 641–647. <https://doi.org/10.1179/1743284715Y.0000000073>.
- [20] D. Ding, Z. Pan, D. Cuiuri, H. Li, *Wire-feed additive manufacturing of metal components: technologies, developments and future interests*, *Int J Adv Manuf Technol*. 81 (2015) 465–481. <https://doi.org/10.1007/s00170-015-7077-3>.
- [21] L. Yuan, Z. Pan, D. Ding, Z. Yu, S. Van Duin, H. Li, W. Li, J. Norrish, *Fabrication of metallic parts with overhanging structures using the robotic wire arc additive manufacturing*, *Journal of Manufacturing Processes*. 63 (2021) 24–34. <https://doi.org/10.1016/j.jmapro.2020.03.018>.
- [22] C.R. Cunningham, J.M. Flynn, A. Shokrani, V. Dhokia, S.T. Newman, *Invited review article: Strategies and processes for high quality wire arc additive manufacturing*, *Additive Manufacturing*. 22 (2018) 672–686. <https://doi.org/10.1016/j.addma.2018.06.020>.
- [23] B. Wu, Z. Pan, D. Ding, D. Cuiuri, H. Li, J. Xu, J. Norrish, *A review of the wire arc additive manufacturing of metals: properties, defects and quality improvement*, *Journal of Manufacturing Processes*. 35 (2018) 127–139. <https://doi.org/10.1016/j.jmapro.2018.08.001>.
- [24] C. Xia, Z. Pan, J. Polden, H. Li, Y. Xu, S. Chen, Y. Zhang, *A review on wire arc additive manufacturing: Monitoring, control and a framework of automated system*, *Journal of Manufacturing Systems*. 57 (2020) 31–45. <https://doi.org/10.1016/j.jmsy.2020.08.008>.
- [25] J. Müller, M. Grabowski, C. Müller, J. Hensel, J. Unglaub, K. Thiele, H. Kloft, K. Dilger, *Design and Parameter Identification of Wire and Arc Additively Manufactured (WAAM) Steel Bars for Use in Construction*, *Metals*. 9 (2019) 725. <https://doi.org/10.3390/met9070725>.
- [26] P. Dirisu, S. Ganguly, A. Mehmanparast, F. Martina, S. Williams, *Analysis of fracture toughness properties of wire + arc additive manufactured high strength low alloy structural steel components*, *Materials Science and Engineering: A*. 765 (2019) 138285. <https://doi.org/10.1016/j.msea.2019.138285>.
- [27] S. Selvi, A. Vishvakshnan, E. Rajasekar, *Cold metal transfer (CMT) technology - An overview*, *Defence Technology*. 14 (2018) 28–44. <https://doi.org/10.1016/j.dt.2017.08.002>.
- [28] L.J. Love, A. Nycz, M. Noakes, B. Post, A. Roschli, S. Babu, *Development and demonstration of large-scale metal additive manufacturing for military vehicle applications - final report*, Oak Ridge National Laboratory, 2016.
- [29] T. Feucht, B. Waldschmitt, J. Lange, M. Erven, *3D-Printing with Steel: Additive Manufacturing of a Bridge in situ*, in: *Proceedings of Eurosteel 2021*, 2021: pp. 1695–1701. <https://doi.org/10.1002/cepa.1475>.
- [30] A. Ermakova, A. Mehmanparast, S. Ganguly, N. Razavi, F. Berto, *Investigation of mechanical and fracture properties of wire and arc additively manufactured low carbon steel components*, *Theoretical and Applied Fracture Mechanics*. 109 (2020) 102685. <https://doi.org/10.1016/j.tafmec.2020.102685>.
- [31] C.V. Haden, G. Zeng, F.M. Carter, C. Ruhl, B.A. Krick, D.G. Harlow, *Wire and arc additive manufactured steel: Tensile and wear properties*, *Additive Manufacturing*. 16 (2017) 115–123. <https://doi.org/10.1016/j.addma.2017.05.010>.
- [32] X. Lu, Y.F. Zhou, X.L. Xing, L.Y. Shao, Q.X. Yang, S.Y. Gao, *Open-source wire and arc additive manufacturing system: formability, microstructures, and mechanical properties*, *Int J Adv Manuf Technol*. 93 (2017) 2145–2154. <https://doi.org/10.1007/s00170-017-0636-z>.

- [33] N. Sridharan, M.W. Noakes, A. Nycz, L.J. Love, R.R. Dehoff, S.S. Babu, On the toughness scatter in low alloy C-Mn steel samples fabricated using wire arc additive manufacturing, *Materials Science and Engineering: A*. 713 (2018) 18–27. <https://doi.org/10.1016/j.msea.2017.11.101>.
- [34] A. Corpus, Manipulation of Mechanical Properties of WAAM Deposited ER70S-6 Through Active Cooling, University of Idaho, 2019.
- [35] M. Ghaffari, A. Vahedi Nemani, M. Rafieazad, A. Nasiri, Effect of solidification defects and HAZ softening on the anisotropic mechanical properties of a wire arc additive-manufactured low-carbon low-alloy steel part, *JOM*. 71 (2019) 4215–4224. <https://doi.org/10.1007/s11837-019-03773-5>.
- [36] X. Hu, A. Nycz, Y. Lee, B. Shassere, S. Simunovic, M. Noakes, Y. Ren, X. Sun, Towards an integrated experimental and computational framework for large-scale metal additive manufacturing, *Materials Science and Engineering: A*. 761 (2019) 138057. <https://doi.org/10.1016/j.msea.2019.138057>.
- [37] M. Rafieazad, M. Ghaffari, A. Vahedi Nemani, A. Nasiri, Microstructural evolution and mechanical properties of a low-carbon low-alloy steel produced by wire arc additive manufacturing, *Int J Adv Manuf Technol*. 105 (2019) 2121–2134. <https://doi.org/10.1007/s00170-019-04393-8>.
- [38] Ron, Levy, Dolev, Leon, Shirizly, Aghion, Environmental behavior of low carbon steel produced by a wire arc additive manufacturing process, *Metals*. 9 (2019) 888. <https://doi.org/10.3390/met9080888>.
- [39] A. Waqas, Q. Xiansheng, X. Jiangtao, W. Hongbo, M. Muzamil, A. Majeed, Directional Tensile properties of steel structure manufactured by robotic assisted GMAW additive manufacturing, in: *Proceedings of 2019 16th International Bhurban Conference on Applied Sciences and Technology (IBCAST)*, IEEE, Islamabad, Pakistan, 2019: pp. 239–242. <https://doi.org/10.1109/IBCAST.2019.8667262>.
- [40] E. Aldalur, F. Veiga, A. Suárez, J. Bilbao, A. Lamikiz, High deposition wire arc additive manufacturing of mild steel: Strategies and heat input effect on microstructure and mechanical properties, *Journal of Manufacturing Processes*. 58 (2020) 615–626. <https://doi.org/10.1016/j.jmapro.2020.08.060>.
- [41] T. Feucht, J. Lange, M. Erven, C.B. Costanzi, U. Knaack, B. Waldschmitt, Additive manufacturing by means of parametric robot programming, *Constr Robot*. 4 (2020) 31–48. <https://doi.org/10.1007/s41693-020-00033-w>.
- [42] A.A. Hassen, M. Noakes, P. Nandwana, S. Kim, V. Kunc, U. Vaidya, L. Love, A. Nycz, Scaling up metal additive manufacturing process to fabricate molds for composite manufacturing, *Additive Manufacturing*. 32 (2020) 101093. <https://doi.org/10.1016/j.addma.2020.101093>.
- [43] G. Kotteman, Steel 3D printing for structures, Technical University of Delft, 2020.
- [44] V.T. Le, T.L. Banh, D.T. Nguyen, V.T. Le, Wire arc additive manufacturing of thin-wall low-carbon steel parts: Microstructure and mechanical properties, *Int. J. Mod. Phys. B*. 34 (2020) 2040154. <https://doi.org/10.1142/S0217979220401542>.
- [45] A.V. Nemani, M. Ghaffari, A. Nasiri, On the Post-Printing Heat Treatment of a Wire Arc Additively Manufactured ER70S Part, *Materials*. 13 (2020) 2795. <https://doi.org/10.3390/ma13122795>.
- [46] Z. Al-Nabulsi, J.T. Mottram, M. Gillie, N. Kourra, M.A. Williams, Mechanical and X ray computed tomography characterisation of a WAAM 3D printed steel plate for structural

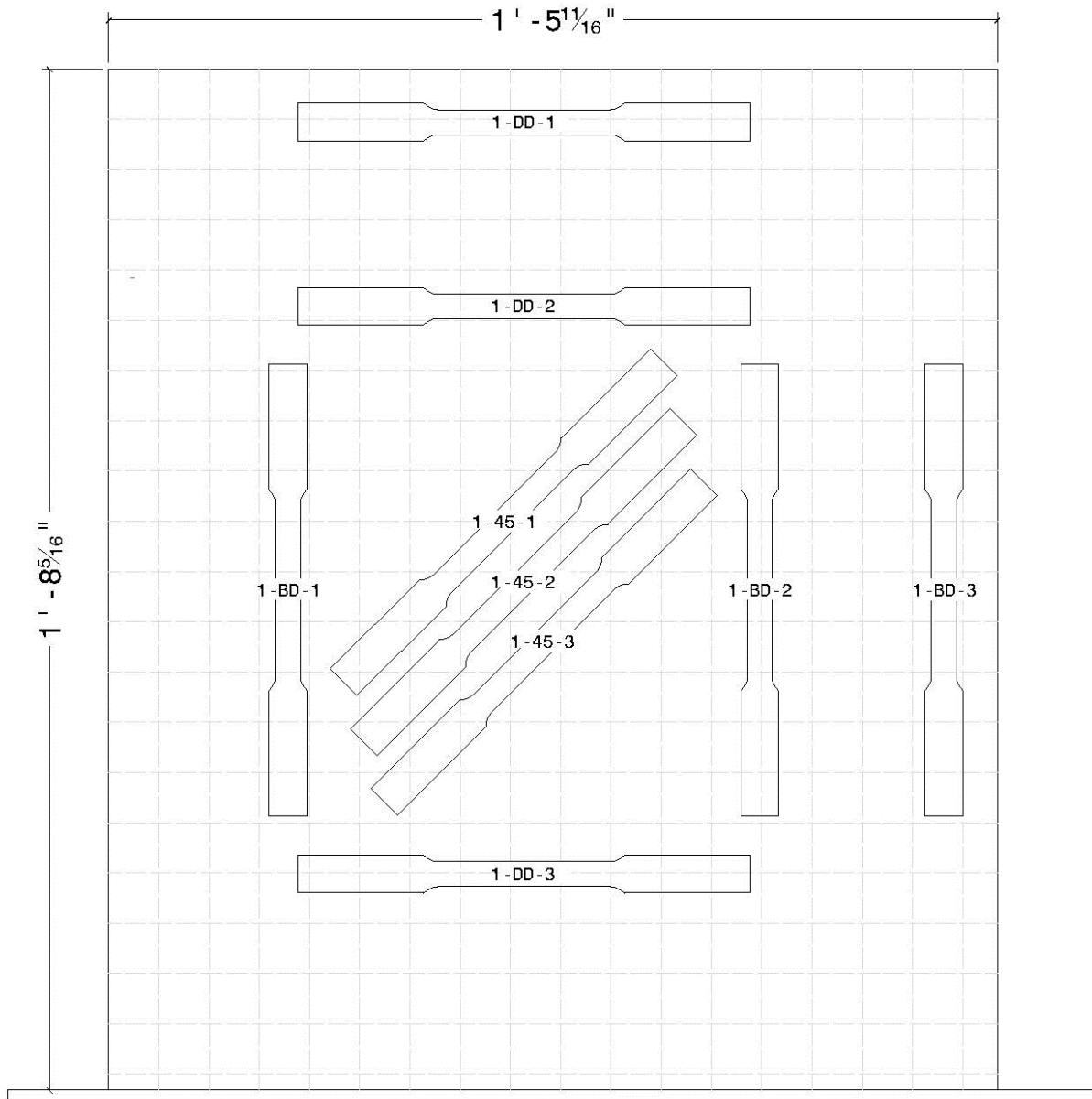
- engineering applications, *Construction and Building Materials*. 274 (2021) 121700. <https://doi.org/10.1016/j.conbuildmat.2020.121700>.
- [47] A. Astarita, G. Campatelli, P. Corigliano, G. Epasto, F. Montevecchi, F. Scherillo, G. Venturini, Microstructure and mechanical properties of specimens produced using the wire-arc additive manufacturing process, *Proceedings of the Institution of Mechanical Engineers, Part C: Journal of Mechanical Engineering Science*. 235 (2021) 1788–1798. <https://doi.org/10.1177/0954406219883324>.
- [48] Y. Ayan, N. Kahraman, Wire arc additive manufacturing of low-carbon mild steel using two different 3D printers, *Phys. Metals Metallogr.* 122 (2021) 1521–1529. <https://doi.org/10.1134/S0031918X21140039>.
- [49] M. Douglass, B. Schaeffer, Leveraging Layers: Additive Manufacturing with Robotic GMAW, *Welding Journal*. (2021) 44–47.
- [50] B.P. Nagasai, S. Malarvizhi, V. Balasubramanian, Mechanical properties of wire arc additive manufactured carbon steel cylindrical component made by gas metal arc welding process, *Journal of the Mechanical Behavior of Materials*. 30 (2021) 188–198. <https://doi.org/10.1515/jmbm-2021-0019>.
- [51] M. Rafieazad, A.V. Nemani, M. Ghaffari, A. Nasiri, On Microstructure and Mechanical Properties of a Low-Carbon Low-Alloy Steel Block Fabricated by Wire Arc Additive Manufacturing, *J. of Materi Eng and Perform.* 30 (2021) 4937–4945. <https://doi.org/10.1007/s11665-021-05568-9>.
- [52] V.-A. Silvestru, I. Ariza, J. Vienne, L. Michel, A.M. Aguilar Sanchez, U. Angst, R. Rust, F. Gramazio, M. Kohler, A. Taras, Performance under tensile loading of point-by-point wire and arc additively manufactured steel bars for structural components, *Materials & Design*. 205 (2021) 109740. <https://doi.org/10.1016/j.matdes.2021.109740>.
- [53] H. Xin, I. Tarus, L. Cheng, M. Veljkovic, N. Persem, L. Lorch, Experiments and numerical simulation of wire and arc additive manufactured steel materials, *Structures*. 34 (2021) 1393–1402. <https://doi.org/10.1016/j.istruc.2021.08.055>.
- [54] Y. Ayan, N. Kahraman, Bending fatigue properties of structural steel fabricated through wire arc additive manufacturing (WAAM), *Engineering Science and Technology, an International Journal*. 35 (2022) 101247. <https://doi.org/10.1016/j.jestch.2022.101247>.
- [55] G.G. Goviazin, A. Shirizly, D. Rittel, Static and dynamic mechanical properties of wire and arc additively manufactured SS316L and ER70S6, *Mechanics of Materials*. 164 (2022) 104108. <https://doi.org/10.1016/j.mechmat.2021.104108>.
- [56] X. Guo, P. Kyvelou, J. Ye, L.H. Teh, L. Gardner, Experimental investigation of wire arc additively manufactured steel single-lap shear bolted connections, *Thin-Walled Structures*. 181 (2022) 110029. <https://doi.org/10.1016/j.tws.2022.110029>.
- [57] C. Huang, P. Kyvelou, R. Zhang, T. Ben Britton, L. Gardner, Mechanical testing and microstructural analysis of wire arc additively manufactured steels, *Materials & Design*. 216 (2022) 110544. <https://doi.org/10.1016/j.matdes.2022.110544>.
- [58] M. Shamir, V. Igwemezie, S. Lotfian, R. Jones, H. Asif, S. Ganguly, A. Mehmanparast, Assessment of mechanical and fatigue crack growth properties of wire + arc additively manufactured mild steel components, *Fatigue Fract Eng Mat Struct*. 45 (2022) 2978–2989. <https://doi.org/10.1111/ffe.13797>.
- [59] T. Tankova, D. Andrade, R. Branco, C. Zhu, D. Rodrigues, L. Simões Da Silva, Characterization of robotized CMT-WAAM carbon steel, *Journal of Constructional Steel Research*. 199 (2022) 107624. <https://doi.org/10.1016/j.jcsr.2022.107624>.

- [60] U. Tripathi, N. Saini, R.S. Mulik, M.M. Mahapatra, Effect of build direction on the microstructure evolution and their mechanical properties using GTAW based wire arc additive manufacturing, *CIRP Journal of Manufacturing Science and Technology*. 37 (2022) 103–109. <https://doi.org/10.1016/j.cirpj.2022.01.010>.
- [61] R. Kühne, M. Feldmann, S. Citarelli, U. Reisingen, R. Sharma, L. Oster, 3D printing in steel construction with the automated Wire Arc Additive Manufacturing, in: *Proceedings of the 14th Nordic Steel Construction Conference*, 2019: pp. 577–583. <https://doi.org/10.1002/cepa.1103>.
- [62] B. Shassere, A. Nycz, M. Noakes, C. Masuo, N. Sridharan, Correlation of microstructure and mechanical properties of metal big area additive manufacturing, *Applied Sciences*. 9 (2019) 787. <https://doi.org/10.3390/app9040787>.
- [63] A. Waqas, Q. Xiansheng, X. Jiangtao, Y. Chaoran, L. Fan, Impact toughness of components made by GMAW based additive manufacturing, *Procedia Structural Integrity*. 13 (2018) 2065–2070. <https://doi.org/10.1016/j.prostr.2018.12.207>.
- [64] M.D. Mohiuddin, S.R. Mohideen, Toughness property evaluation of additive welded low carbon steel weldments, in: *Advances in Design and Thermal Systems*, Springer Singapore, Singapore, 2021: pp. 431–439. [https://doi.org/10.1007/978-981-33-6428-8\\_35](https://doi.org/10.1007/978-981-33-6428-8_35).
- [65] K. Dağyikan, U. Gürol, M. Koçak, Characterization and fracture toughness evaluation of the thick-walled wire arc additively manufactured low alloy steels, *Weld World*. 67 (2023) 1009–1019. <https://doi.org/10.1007/s40194-022-01424-z>.
- [66] T. Ron, G.K. Levy, O. Dolev, A. Leon, A. Shirizly, E. Aghion, The effect of microstructural imperfections on corrosion fatigue of additively manufactured ER70S-6 alloy produced by wire arc deposition, *Metals*. 10 (2020) 98. <https://doi.org/10.3390/met10010098>.
- [67] P. Dirisu, G. Supriyo, F. Martina, X. Xu, S. Williams, Wire plus arc additive manufactured functional steel surfaces enhanced by rolling, *International Journal of Fatigue*. 130 (2020) 105237. <https://doi.org/10.1016/j.ijfatigue.2019.105237>.
- [68] H. Bartsch, R. Kühne, S. Citarelli, S. Schaffrath, M. Feldmann, Fatigue analysis of wire arc additive manufactured (3D printed) components with unmilled surface, *Structures*. 31 (2021) 576–589. <https://doi.org/10.1016/j.istruc.2021.01.068>.
- [69] T. Smismans, N. Chernovol, B. Lauwers, P. Van Rymenant, R. Talemi, Influence of post-heat treatments on fatigue response of low-alloyed carbon-manganese steel material manufactured by Direct Energy Deposition-Arc technique, *Materials Letters*. 302 (2021) 130465. <https://doi.org/10.1016/j.matlet.2021.130465>.
- [70] A. Ermakova, N. Razavi, F. Berto, A. Mehmanparast, Uniaxial and multiaxial fatigue behaviour of wire arc additively manufactured ER70S-6 low carbon steel components, *International Journal of Fatigue*. 166 (2023) 107283. <https://doi.org/10.1016/j.ijfatigue.2022.107283>.
- [71] ASTM International, ASTM E1820-20: Standard Test Method for Measurement of Fracture Toughness, 2020.
- [72] A. Ermakova, A. Mehmanparast, S. Ganguly, N. Razavi, F. Berto, Fatigue crack growth behaviour of wire and arc additively manufactured ER70S-6 low carbon steel components, *Int J Fract*. 235 (2022) 47–59. <https://doi.org/10.1007/s10704-021-00545-8>.
- [73] ASTM International, ASTM E647-15: Standard Test Method for Measurement of Fatigue Crack Growth Rates, 2015.
- [74] British Standards Institution, BS 7910 Guide to Methods for Assessing the Acceptability of Flaws in Metallic Structures, 2015.

- [75] S. M. Adinarayanappa, S. Simhambhatla, Twin-wire welding based additive manufacturing (TWAM): manufacture of functionally gradient objects, *RPJ*. 23 (2017) 858–868. <https://doi.org/10.1108/RPJ-09-2015-0126>.
- [76] Q. Wu, T. Mukherjee, C. Liu, J. Lu, T. DebRoy, Residual stresses and distortion in the patterned printing of titanium and nickel alloys, *Additive Manufacturing*. 29 (2019) 100808. <https://doi.org/10.1016/j.addma.2019.100808>.
- [77] S. Chandrasekaran, S. Hari, M. Amirthalingam, Wire arc additive manufacturing of functionally graded material for marine risers, *Materials Science and Engineering: A*. 792 (2020) 139530. <https://doi.org/10.1016/j.msea.2020.139530>.
- [78] E. Tenuta, A. Nycz, M. Noakes, S. Simunovic, M.H.A. Piro, Material properties and mechanical behaviour of functionally graded steel produced by wire-arc additive manufacturing, *Additive Manufacturing*. 46 (2021) 102175. <https://doi.org/10.1016/j.addma.2021.102175>.
- [79] A. Nycz, M.W. Noakes, B. Richardson, A. Messing, B. Post, J. Paul, J. Flamm, L. Love, Challenges in making complex metal large-scale parts for additive manufacturing: a case study based on the additive manufacturing excavator, in: *Proceedings of the 28th Annual International Solid Freeform Fabrication Symposium*, 2017.
- [80] S. Simunovic, A. Nycz, M.W. Noakes, C. Chin, V. Oancea, Metal big area additive manufacturing: process modeling and validation, in: 2017.
- [81] B. Post, C. Atkins, A. Jackson, P. Chesser, A. Roschli, A. Barnes, A. Nycz, L. Meyer, P. Jensen, M. Vcelka, S. Carron, A comparative study of direct and indirect additive manufacturing approaches for the production of a wind energy component, Oak Ridge National Laboratory, 2021. <https://doi.org/10.2172/1809969>.
- [82] RAMLAB, RAMLAB unveils world's first class approved 3D printed ship's propeller, RAMLAB. (2017). <https://www.ramlab.com/updates/ramlab-unveils-worlds-first-class-approved-3d-printed-ships-propeller/> (accessed August 25, 2023).
- [83] S. Saunders, After Successful Testing and Verification, 3D Printed WAAMPeller is Introduced to the Public, 3DPrint.Com. (2017). <https://3dprint.com/195791/3d-printed-waampeller-verified/> (accessed August 25, 2023).
- [84] C. Buchanan, V.-P. Matilainen, A. Salminen, L. Gardner, Structural performance of additive manufactured metallic material and cross-sections, *Journal of Constructional Steel Research*. 136 (2017) 35–48. <https://doi.org/10.1016/j.jcsr.2017.05.002>.
- [85] P. Kyvelou, C. Huang, L. Gardner, C. Buchanan, Structural Testing and Design of Wire Arc Additively Manufactured Square Hollow Sections, *J. Struct. Eng.* 147 (2021) 04021218. [https://doi.org/10.1061/\(ASCE\)ST.1943-541X.0003188](https://doi.org/10.1061/(ASCE)ST.1943-541X.0003188).
- [86] C. Huang, X. Meng, L. Gardner, Flexural behavior of wire arc additively manufactured tubular sections, in: *Proceedings of the Annual Stability Conference Structural Stability Research Council*, Charlotte, North Carolina, USA, 2023.
- [87] X. Guo, P. Kyvelou, J. Ye, L.H. Teh, L. Gardner, Experimental study of DED-arc additively manufactured steel double-lap shear bolted connections, *Engineering Structures*. 281 (2023) 115736. <https://doi.org/10.1016/j.engstruct.2023.115736>.
- [88] G.S. van Bolderen, Exploration of stability of 3D-printed steel members, Technical University of Delft, n.d.
- [89] L. Gardner, P. Kyvelou, G. Herbert, C. Buchanan, Testing and initial verification of the world's first metal 3D printed bridge, *Journal of Constructional Steel Research*. 172 (2020) 106233. <https://doi.org/10.1016/j.jcsr.2020.106233>.

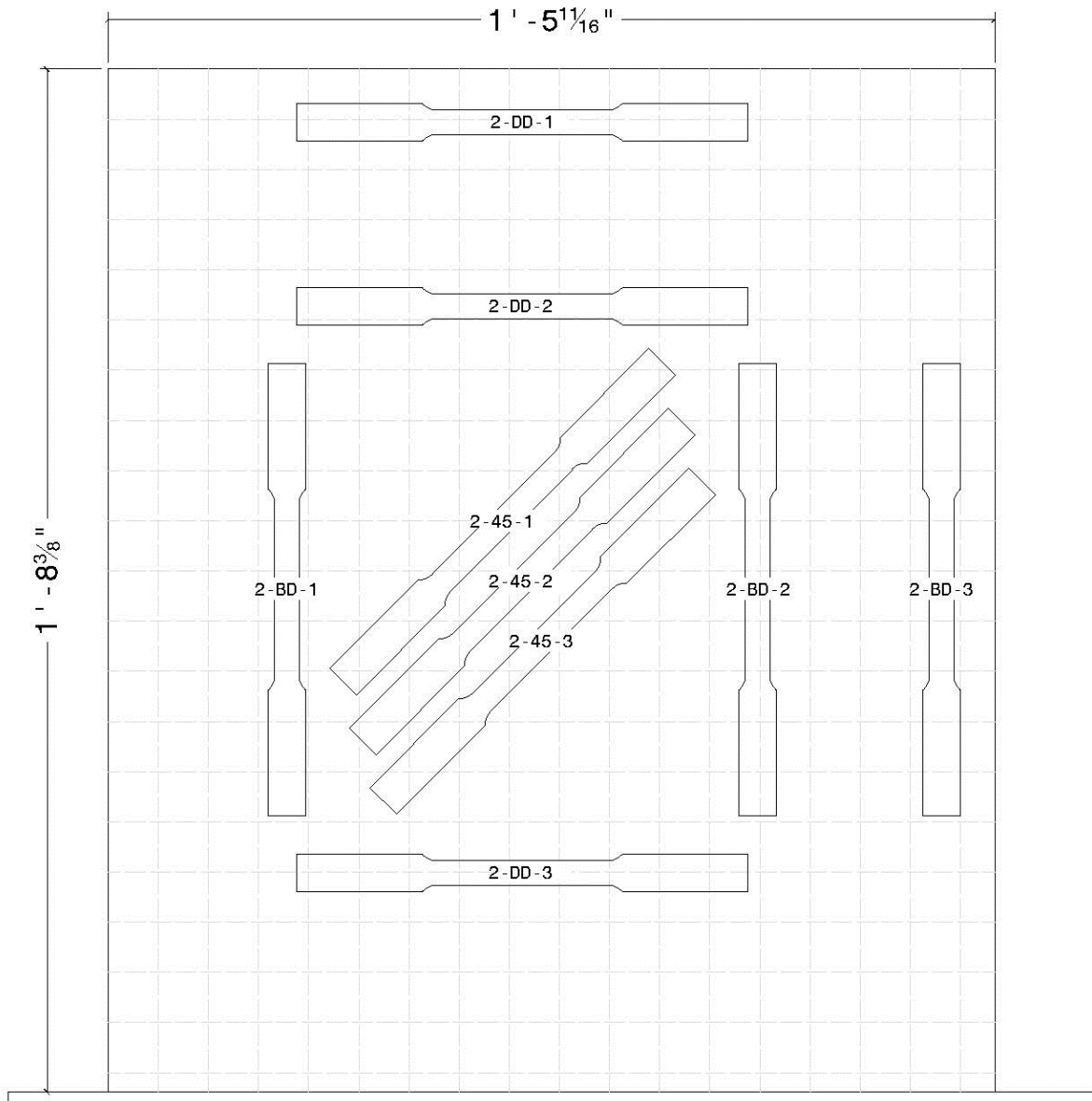
- [90] J. Parkes, Long-awaited 3D-printed stainless steel bridge opens in Amsterdam, Dezeen. (2021). <https://www.dezeen.com/2021/07/19/mx3d-3d-printed-bridge-stainless-steel-amsterdam/> (accessed August 25, 2023).
- [91] Merlin, MX3D bridge, smart bridge passed the final load test!, MX3D. (2020). <https://mx3d.com/timeline/we-have-past-the-load-test-next-up-sensor-placement/> (accessed August 25, 2023).
- [92] MX3D, Use Case - Connector For Takenaka, MX3D. (n.d.). <https://mx3d.com/industries/construction/connector-for-takenaka/> (accessed August 25, 2023).
- [93] MX3D, Lunar Floor for European Space Agency, MX3D. (n.d.). <https://mx3d.com/industries/construction/lunar-floor-for-esa/> (accessed August 25, 2023).
- [94] J. Lange, T. Feucht, M. Erven, 3D printing with steel: Additive Manufacturing for connections and structures, *Steel Construction*. 13 (2020) 144–153. <https://doi.org/10.1002/stco.202000031>.
- [95] M. Erven, J. Lange, T. Feucht, 3D-Printing with steel of a bolted connection, in: *Proceedings of Eurosteel 2021*, 2021: pp. 825–832. <https://doi.org/10.1002/cepa.1367>.
- [96] D. Mann, ASME Section III, SG-MF&E Materials, Fabrication and Examination, TG-AM Task Group Advanced Mfg., (2021).
- [97] J.B. Schaeffer, B. Barnhart, T. Melfi, A statistical study of mechanical properties from mild steel welds deposited via gas metal arc additive manufacturing (GMAAM), in: *Proceedings of the ASME 2022 Pressure Vessels & Piping Conference*, American Society of Mechanical Engineers, Las Vegas, Nevada, USA, 2022: p. V04AT06A006. <https://doi.org/10.1115/PVP2022-84056>.
- [98] J.P. Kruth, Bleys, P., Measuring residual stress caused by Wire EDM of tool steel, *International Journal of Electrical Machining*. (2000).
- [99] T. Yount, T. Sorensen, W. Collins, M. Maguire, Investigating the mechanical properties and fracture behavior of welded-wire reinforcement, *J. Mater. Civ. Eng.* 33 (2021) 04021023. [https://doi.org/10.1061/\(ASCE\)MT.1943-5533.0003622](https://doi.org/10.1061/(ASCE)MT.1943-5533.0003622).
- [100] P.B. Keating, J.W. Fisher, NCHRP Report 286: Evaluation of fatigue tests and design criteria on welded details, Transportation Research Board, Washington, DC, 1986.
- [101] Strategic Highway Research Program, Bridges for Service Life Beyond 100 Years: Service Limit State Design, Transportation Research Board, Washington, D.C., 2014. <https://doi.org/10.17226/22441>.
- [102] ASTM International, ASTM D4417-21: Test Methods for Field Measurement of Surface Profile of Blast Cleaned Steel, ASTM International, n.d. <https://doi.org/10.1520/D4417-21>.
- [103] J.T. Provines, J.M. Ocel, K. Zmetra, FHWA-HRT-20-005: Strength and fatigue resistance of clustered shear stud connectors in composite steel girders, Federal Highway Administration, 2019.
- [104] P.B. Keating, J.W. Fisher, Review of fatigue tests and design criteria on welded details, final report, Lehigh University, 1986.

**APPENDIX A: TENSION SPECIMEN LOCATIONS IN EACH WALL**



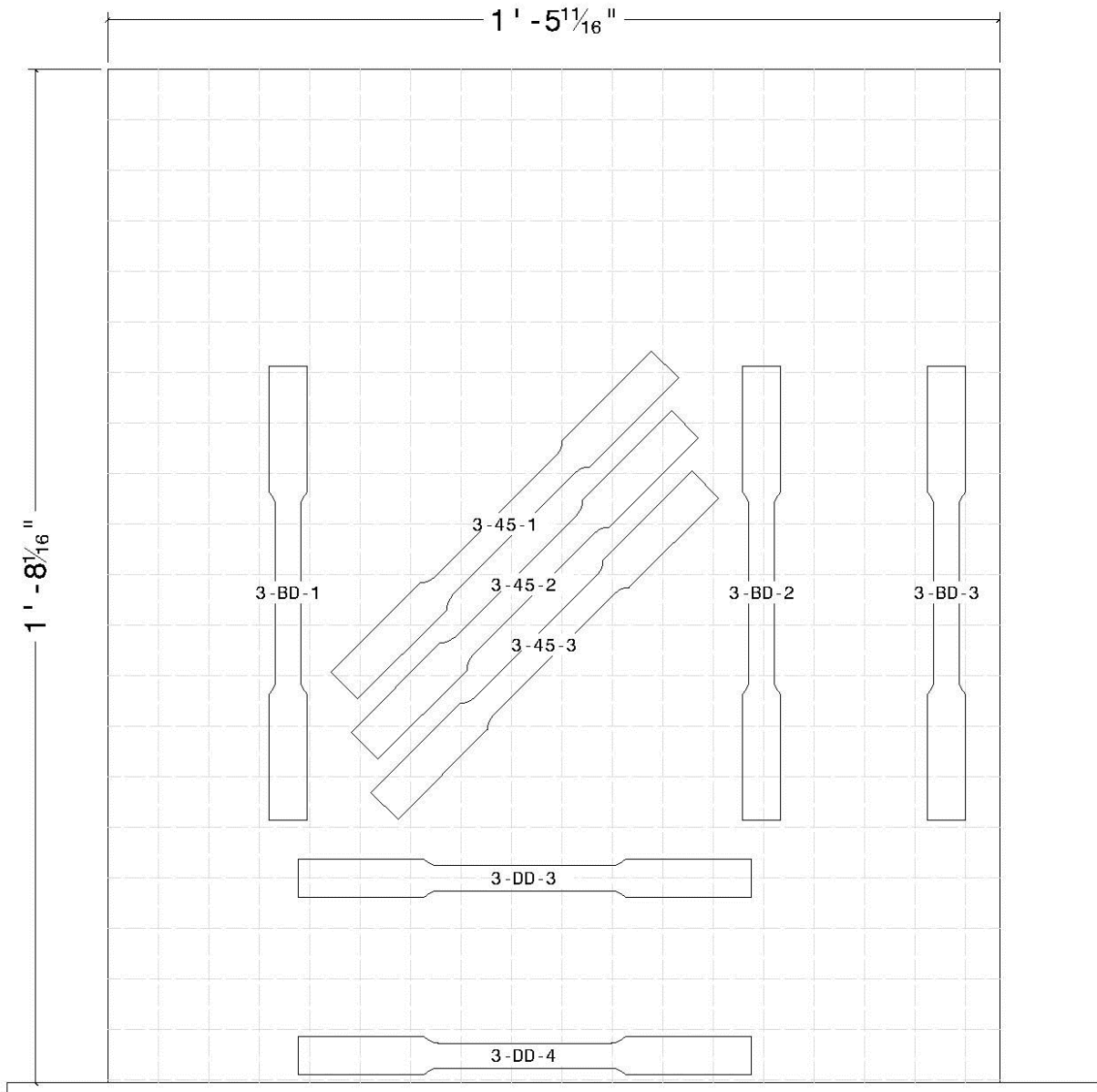
Source: FHWA.

**Figure 40. Drawing. Approximate locations from which tension specimens were removed from F70Lo.**



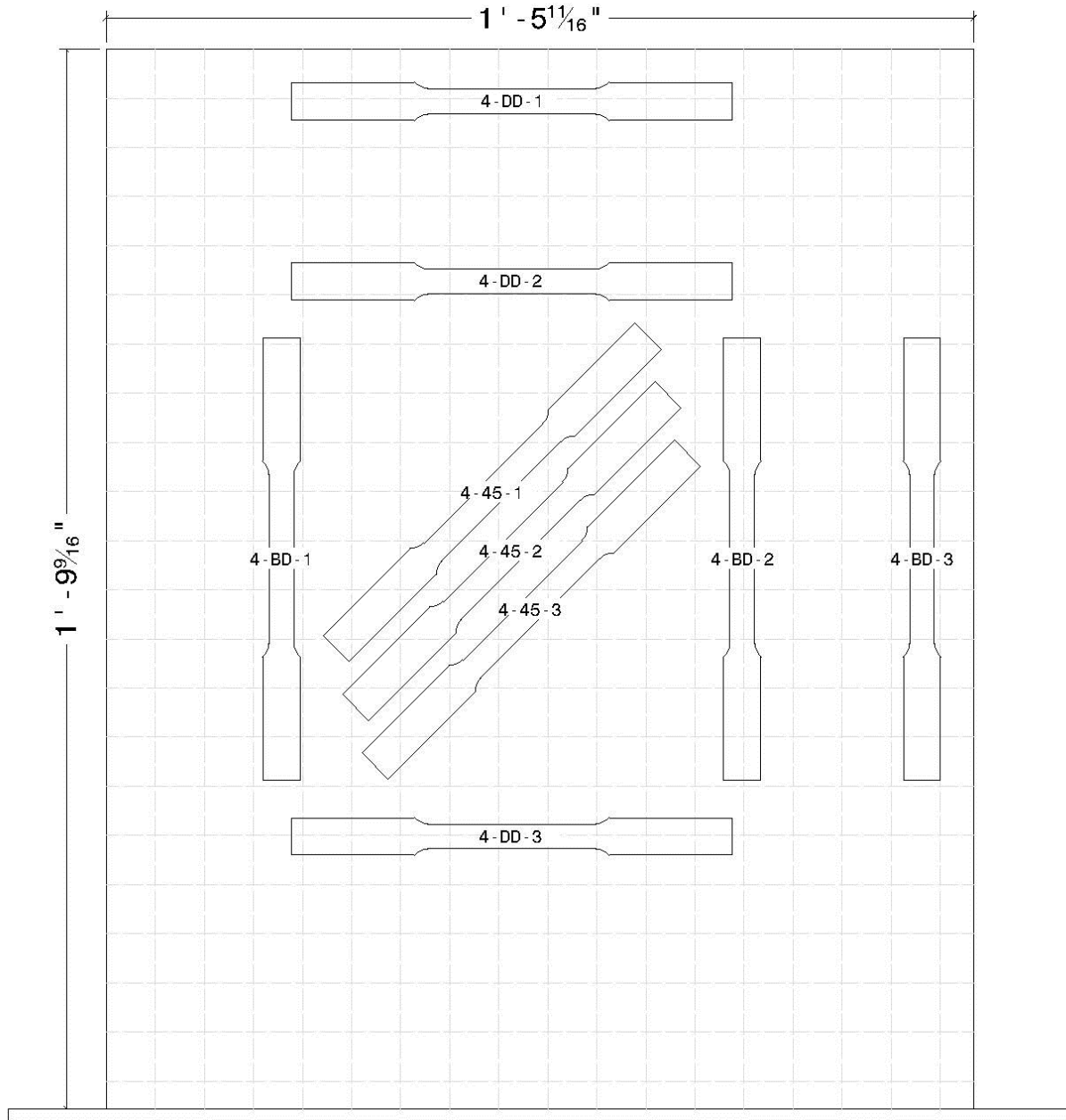
Source: FHWA.

**Figure 41. Drawing. Approximate locations from which tension specimens were removed from F70Hi.**



Source: FHWA.

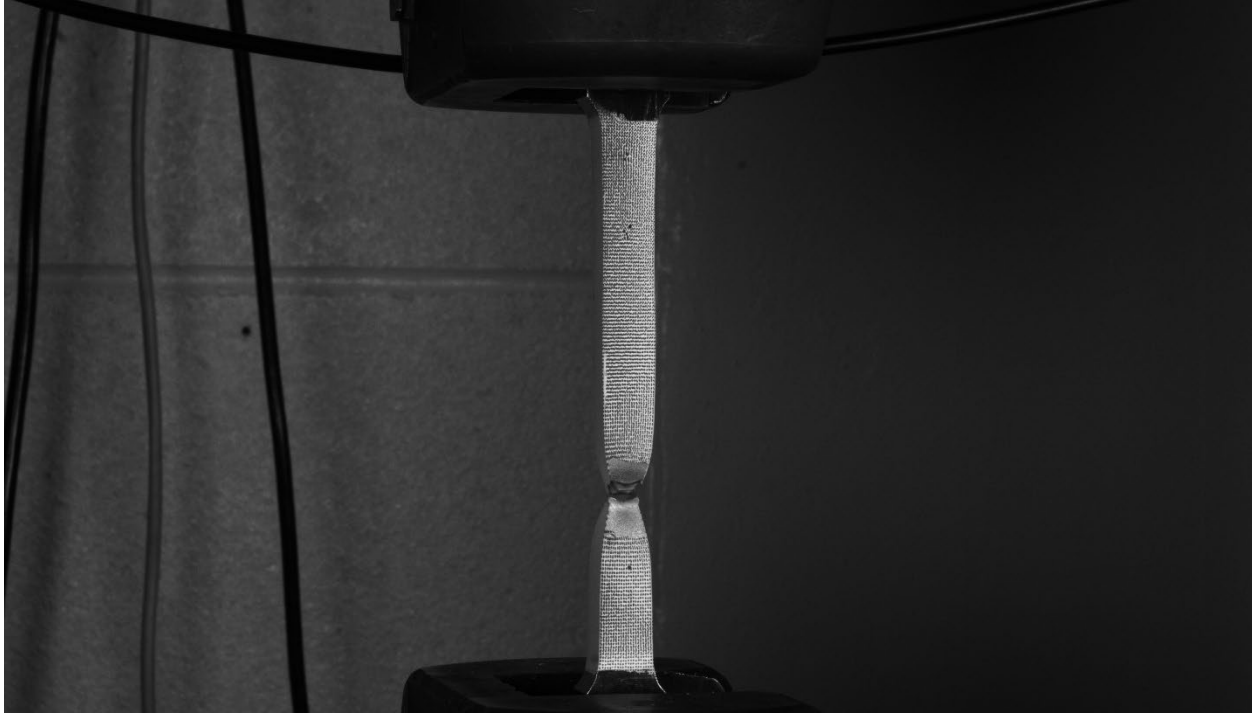
**Figure 42. Drawing. Approximate locations from which tension specimens were removed from F80Lo.**



Source: FHWA.

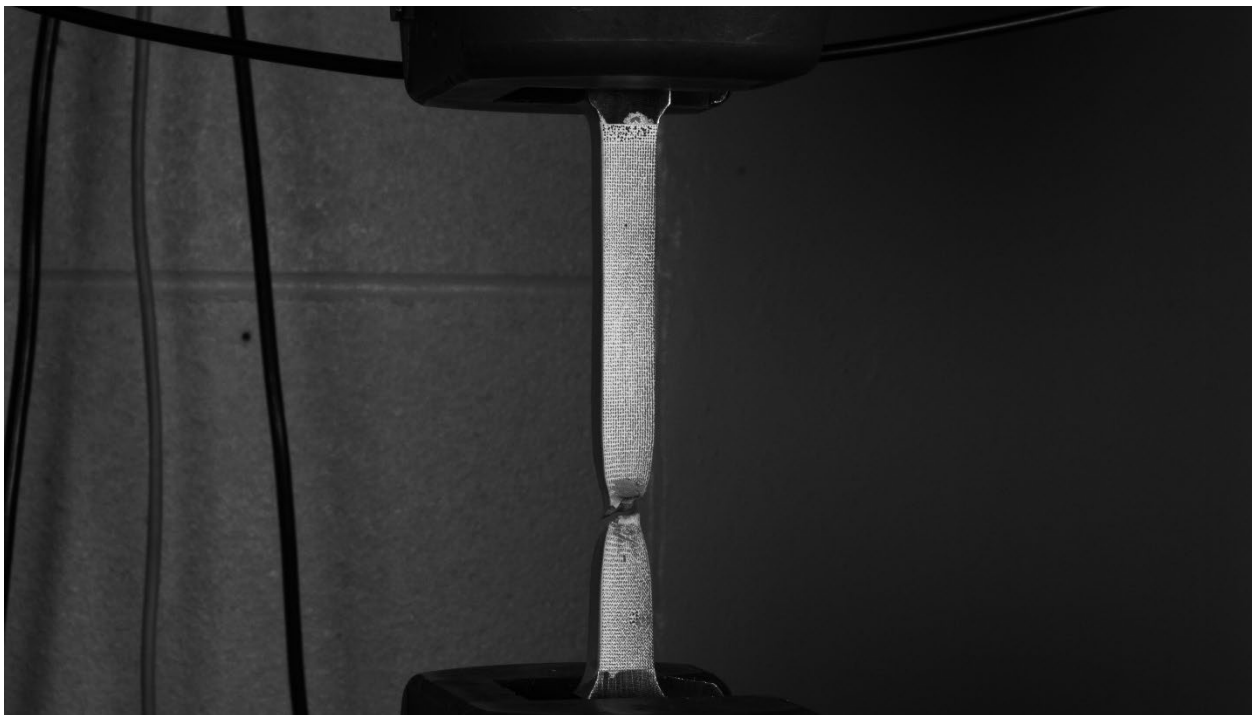
**Figure 43. Drawing. Approximate locations from which tension specimens were removed from F80Hi.**

**APPENDIX B: PHOTOS OF TENSION SPECIMENS POST FRACTURE**



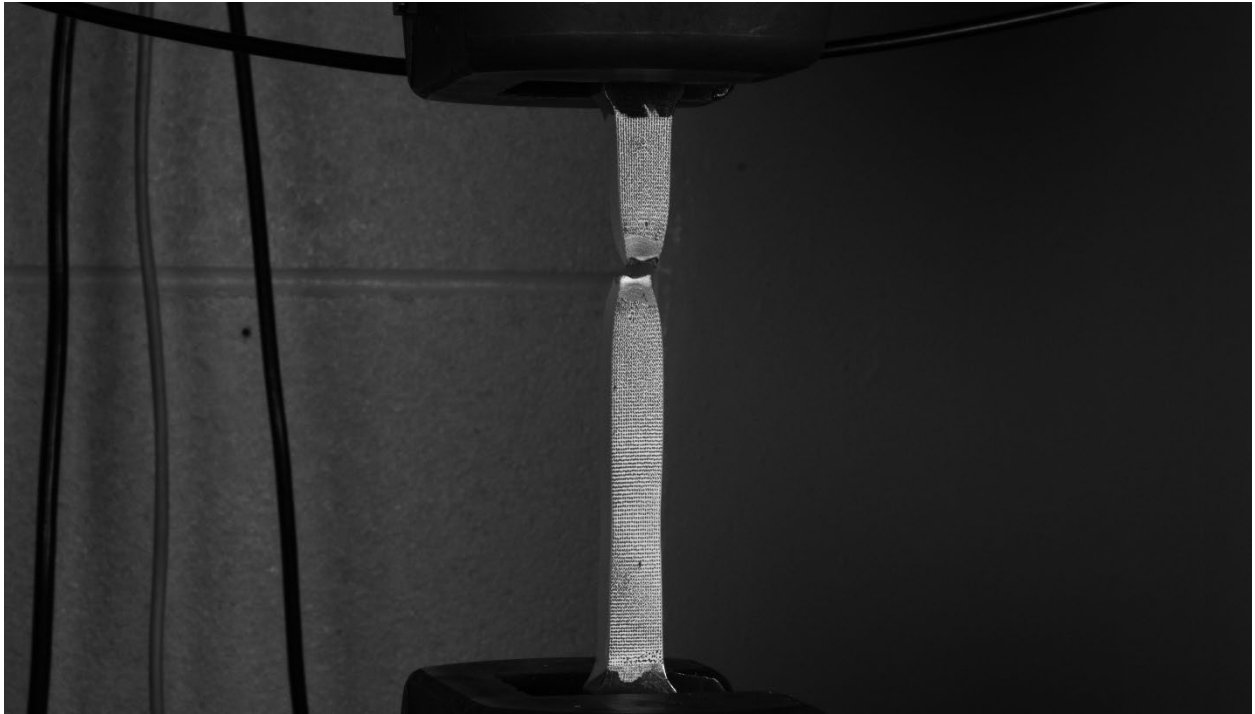
Source: FHWA.

**Figure 44. Photo. Specimen F70Lo-BD-1 in UTM grips post fracture.**



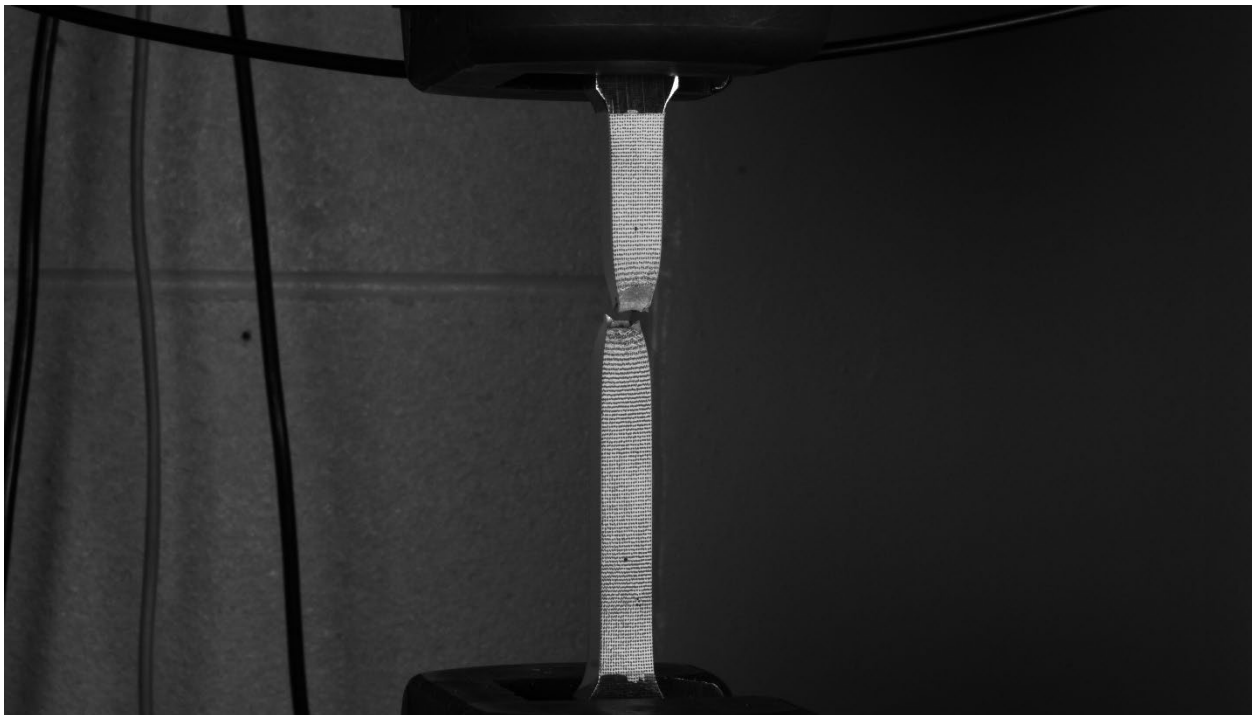
Source: FHWA.

**Figure 45. Photo. Specimen F70Lo-BD-2 in UTM grips post fracture.**



Source: FHWA.

**Figure 46. Photo. Specimen F70Lo-BD-3 in UTM grips post fracture.**



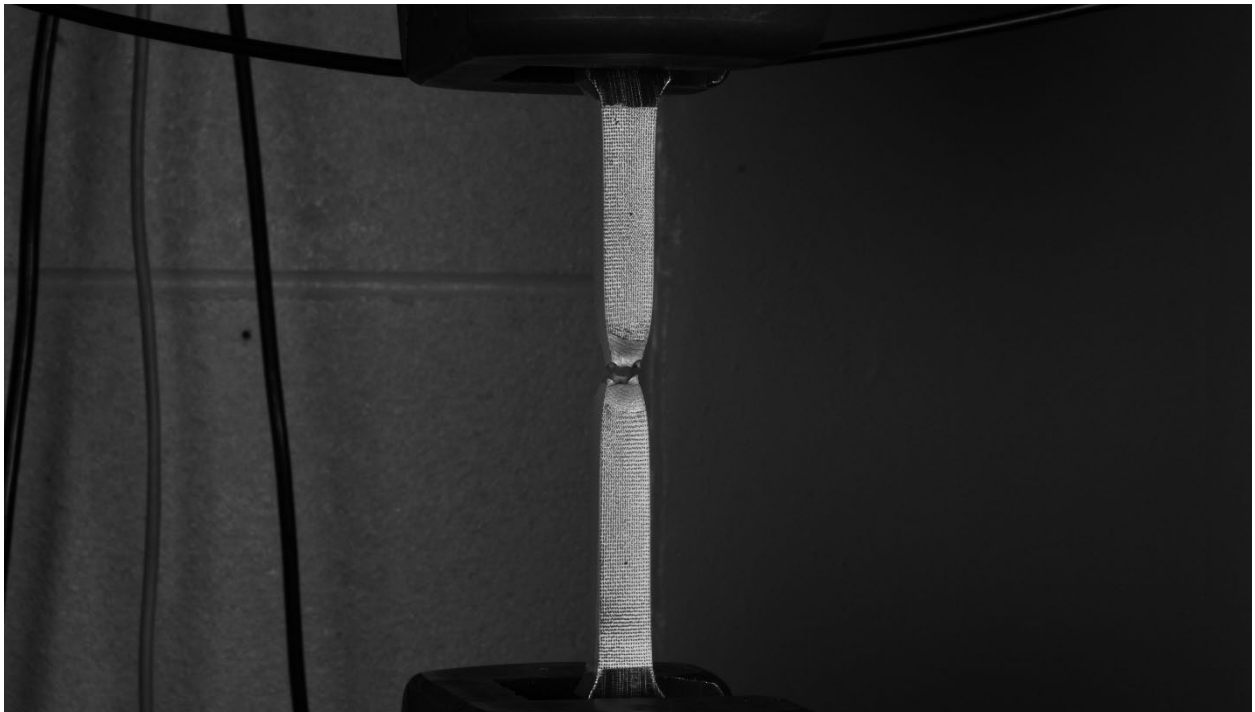
Source: FHWA.

**Figure 47. Photo. Specimen F70Lo-DD-1 in UTM grips post fracture.**



Source: FHWA.

**Figure 48. Photo. Specimen F70Lo-DD-2 in UTM grips post fracture.**



Source: FHWA.

**Figure 49. Photo. Specimen F70Lo-DD-3 in UTM grips post fracture.**



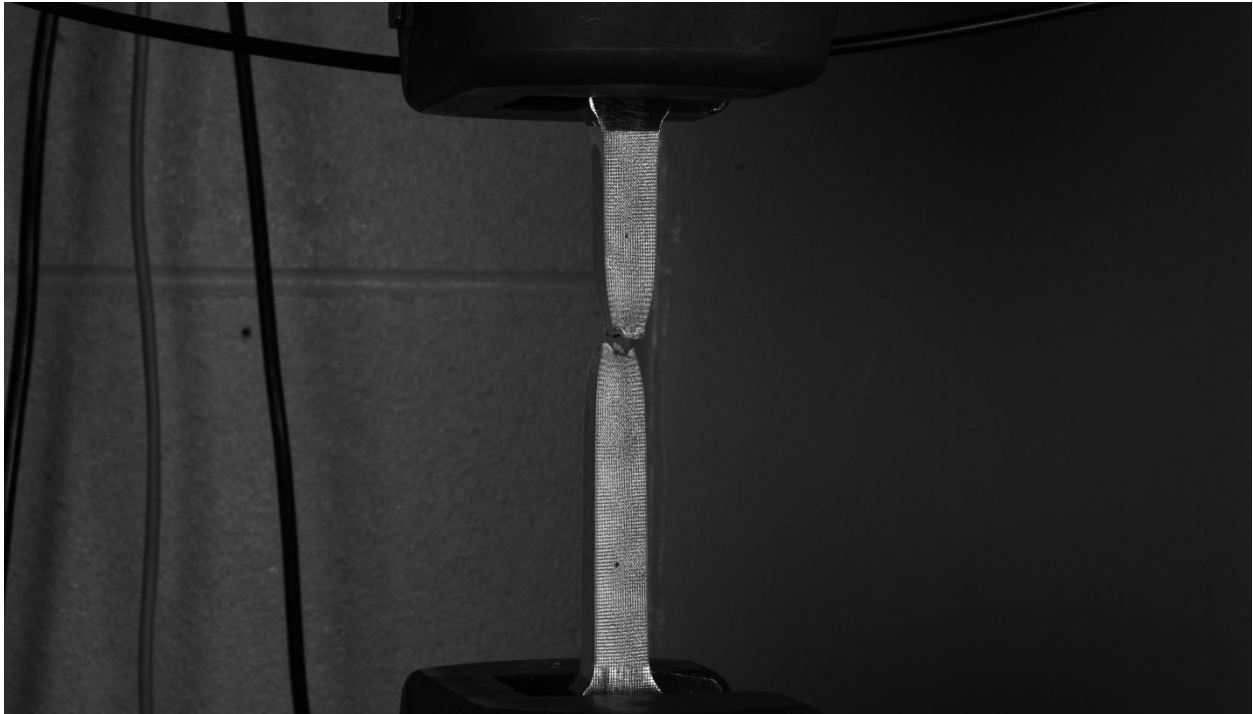
Source: FHWA.

**Figure 50. Photo. Specimen F70Lo-45-1 post fracture.**



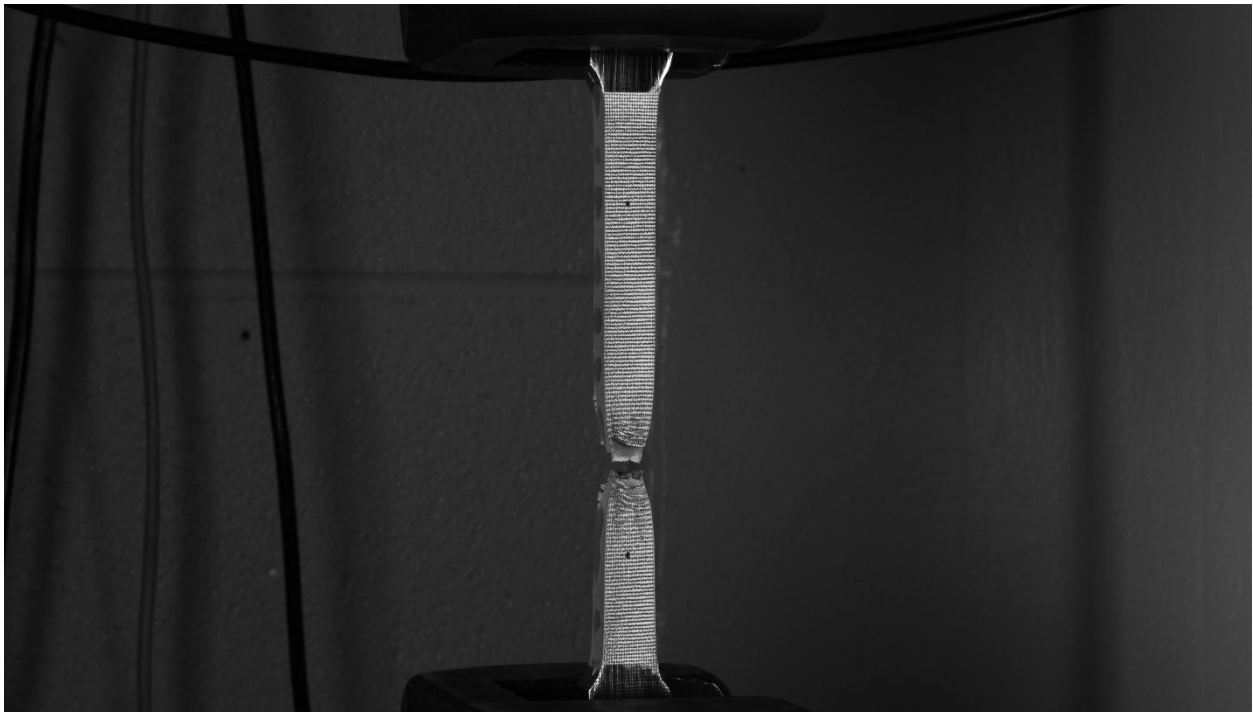
Source: FHWA.

**Figure 51. Photo. Specimen F70Lo-45-2 in UTM grips post fracture.**



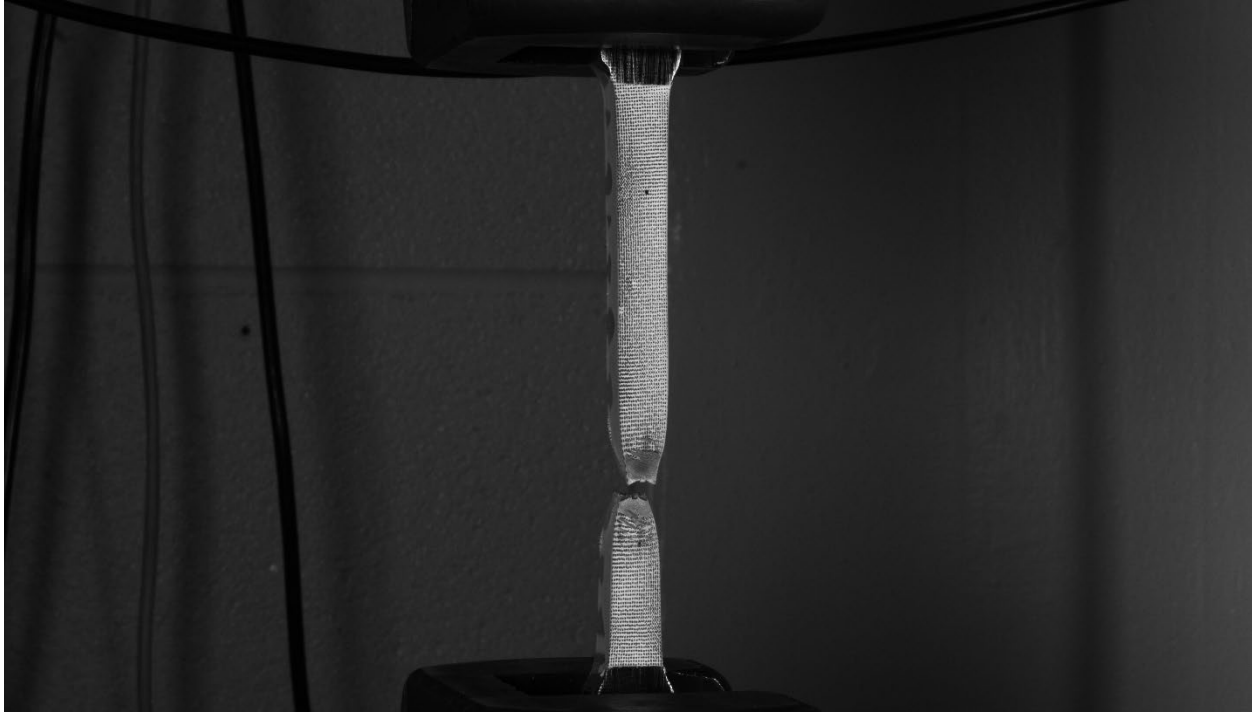
Source: FHWA.

**Figure 52. Photo. Specimen F70Lo-45-3 in UTM grips post fracture.**



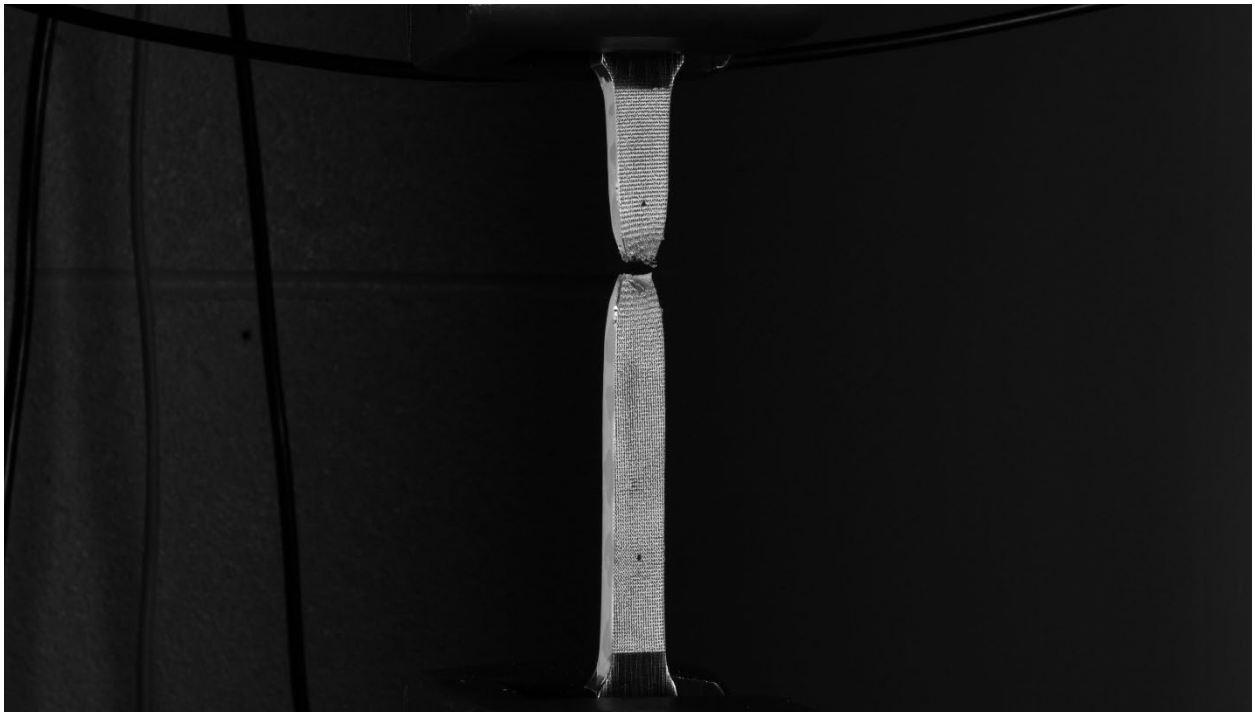
Source: FHWA.

**Figure 53. Photo. Specimen F70Hi-BD-1 in UTM grips post fracture.**



Source: FHWA.

**Figure 54. Photo. Specimen F70Hi-BD-2 in UTM grips post fracture.**



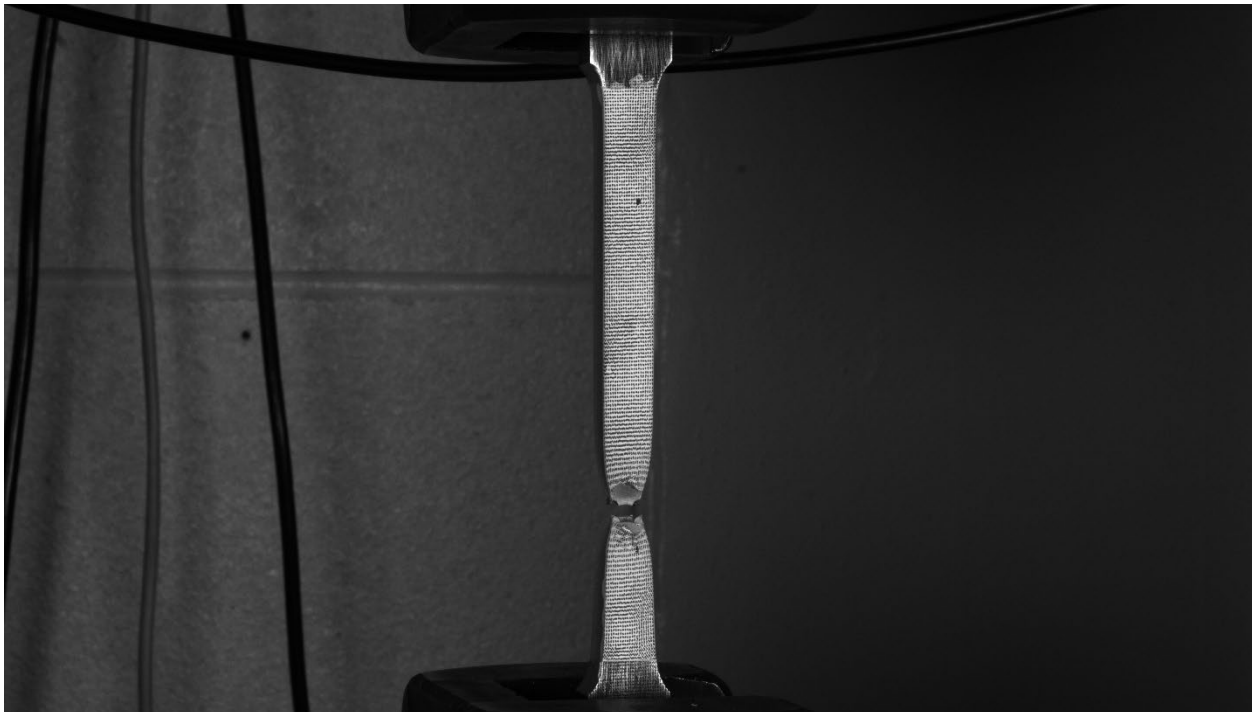
Source: FHWA.

**Figure 55. Photo. Specimen F70Hi-BD-3 in UTM grips post fracture.**



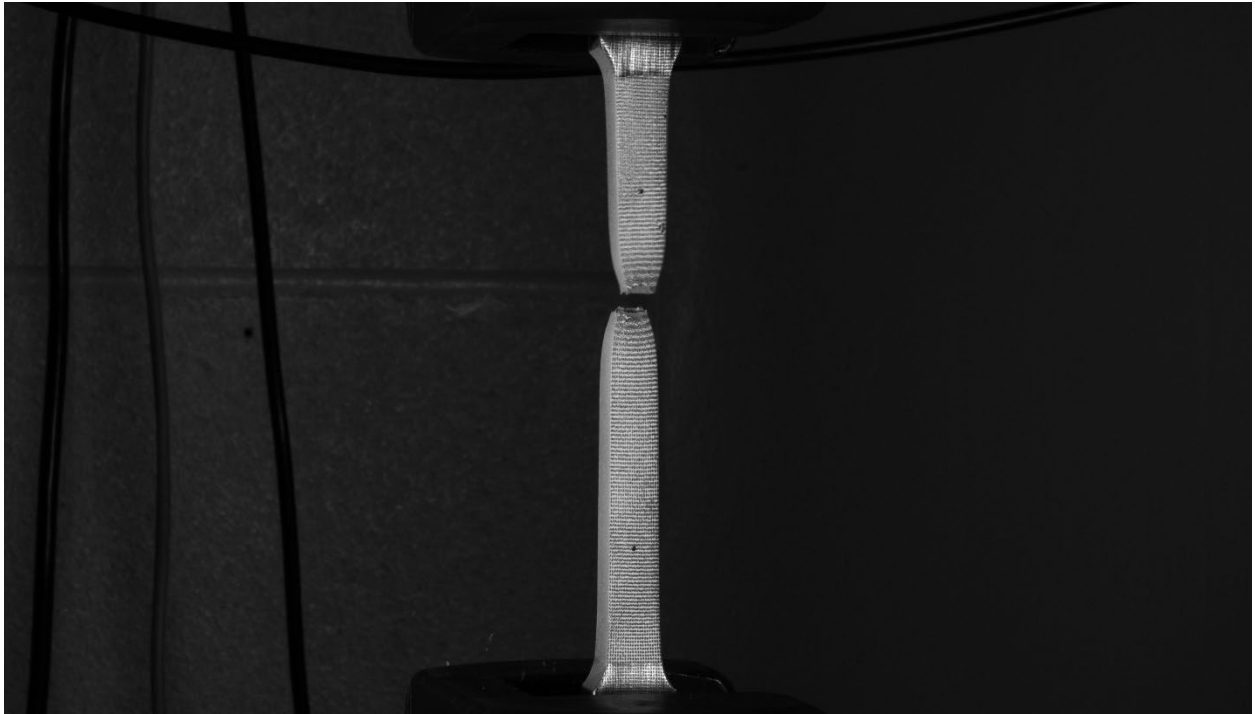
Source: FHWA.

**Figure 56. Photo. Specimen F70Hi-DD-1 in UTM grips post fracture.**



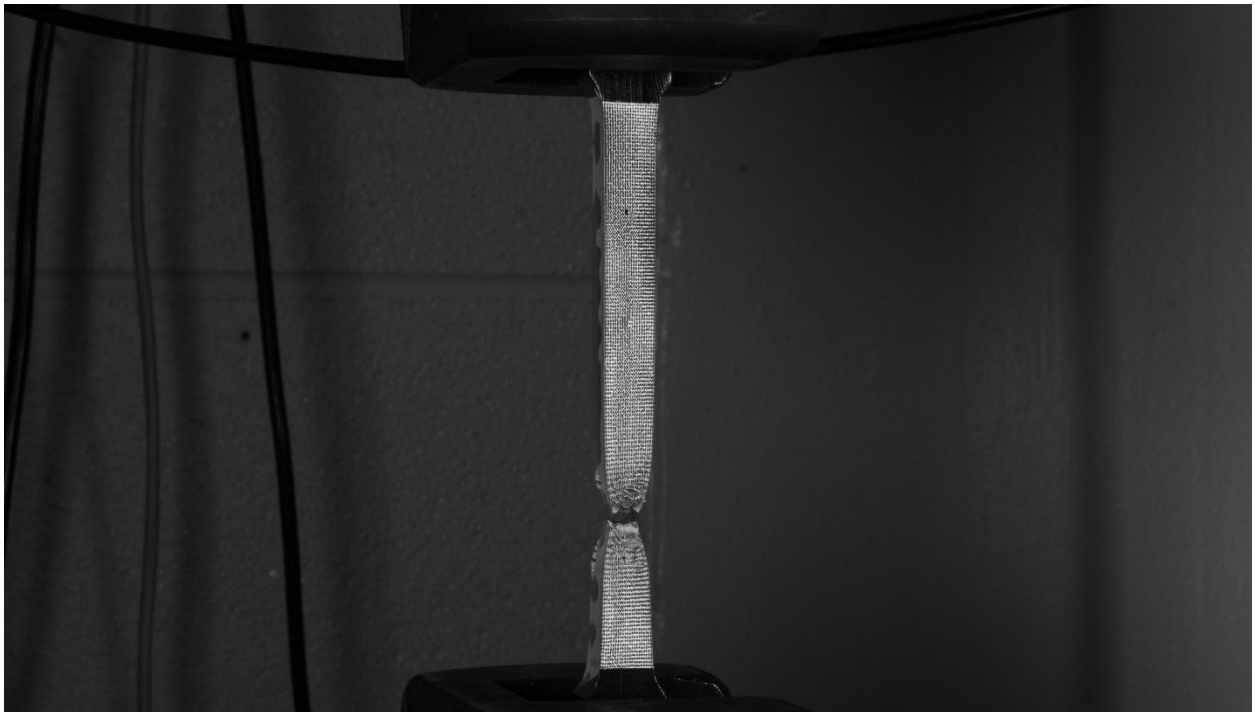
Source: FHWA.

**Figure 57. Photo. Specimen F70Hi-DD-2 in UTM grips post fracture.**



Source: FHWA.

**Figure 58. Photo. Specimen F70Hi-DD-3 in UTM grips post fracture.**



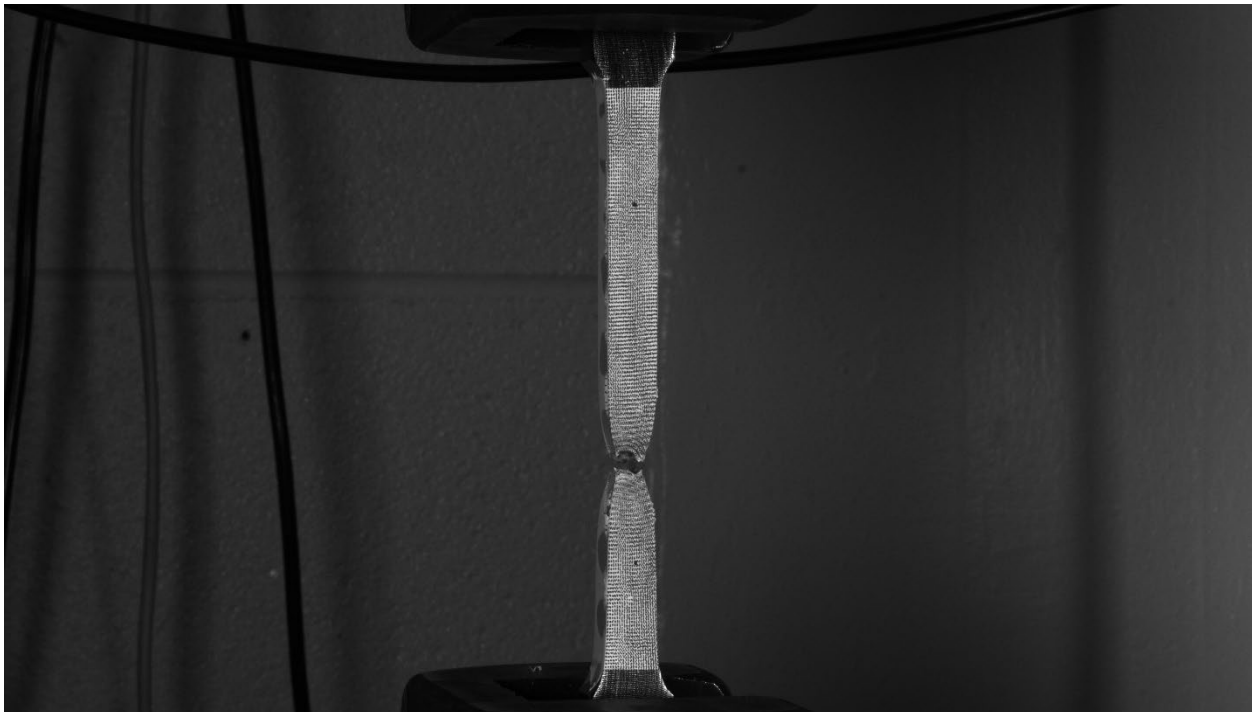
Source: FHWA.

**Figure 59. Photo. Specimen F70Hi-45-1 in UTM grips post fracture.**



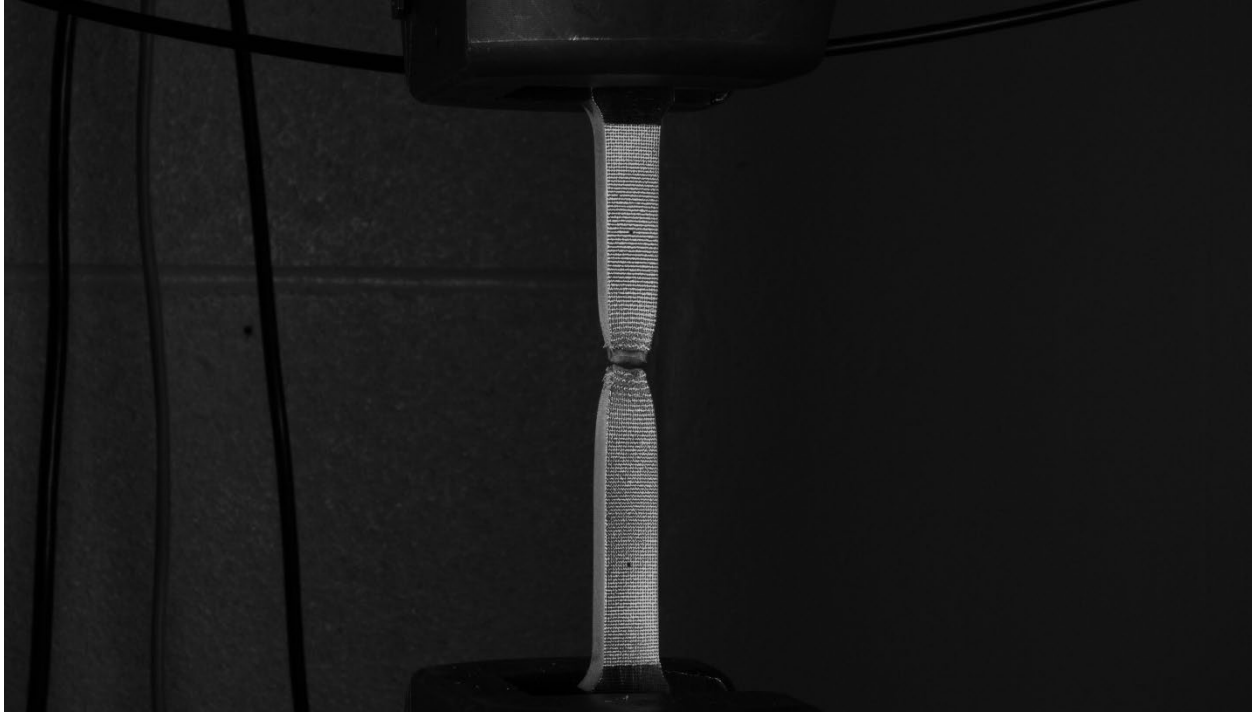
Source: FHWA.

**Figure 60. Photo. Specimen F70Hi-45-2 in UTM grips post fracture.**



Source: FHWA.

**Figure 61. Photo. Specimen F70Hi-45-3 in UTM grips post fracture.**



Source: FHWA.

**Figure 62. Photo. Specimen F80Lo-BD-1 in UTM grips post fracture.**



Source: FHWA.

**Figure 63. Photo. Specimen F80Lo-BD-2 in UTM grips post fracture.**



Source: FHWA.

**Figure 64. Photo. Specimen F80Lo-BD-3 in UTM grips post fracture.**



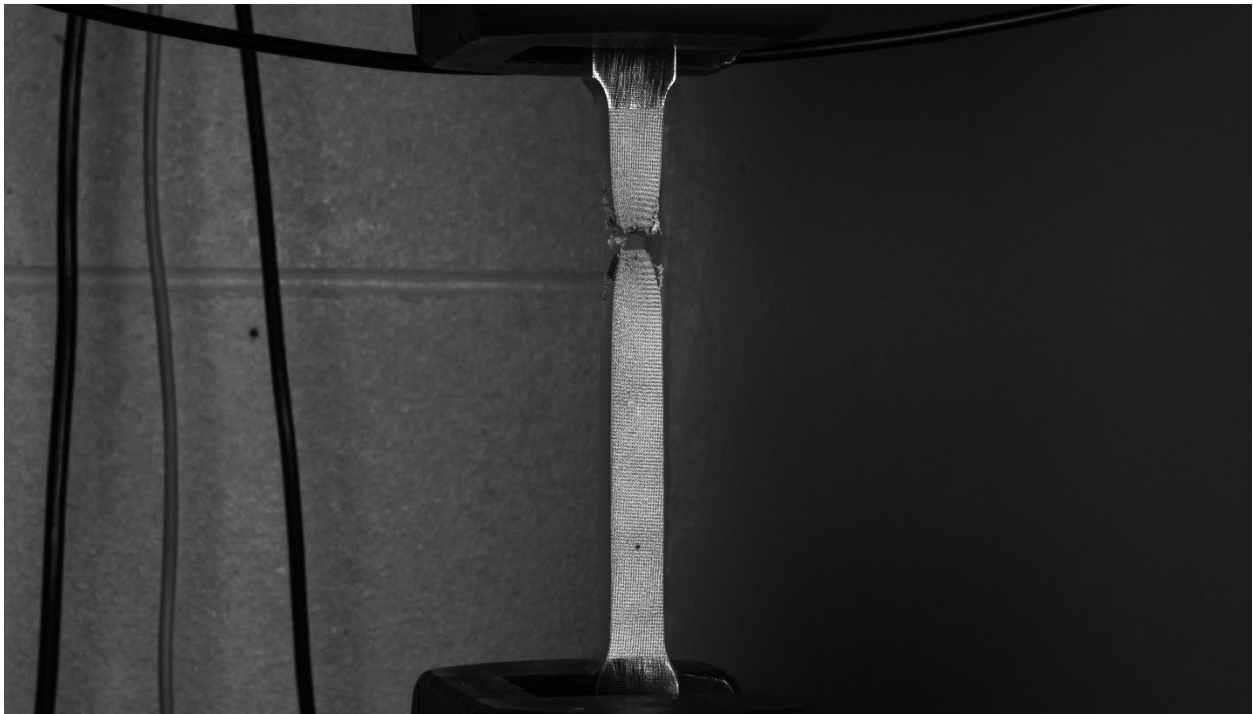
Source: FHWA.

**Figure 65. Photo. Specimen F80Lo-DD-3 in UTM grips post fracture.**



Source: FHWA.

**Figure 66. Photo. Specimen F80Lo-DD-4 in UTM grips post fracture.**



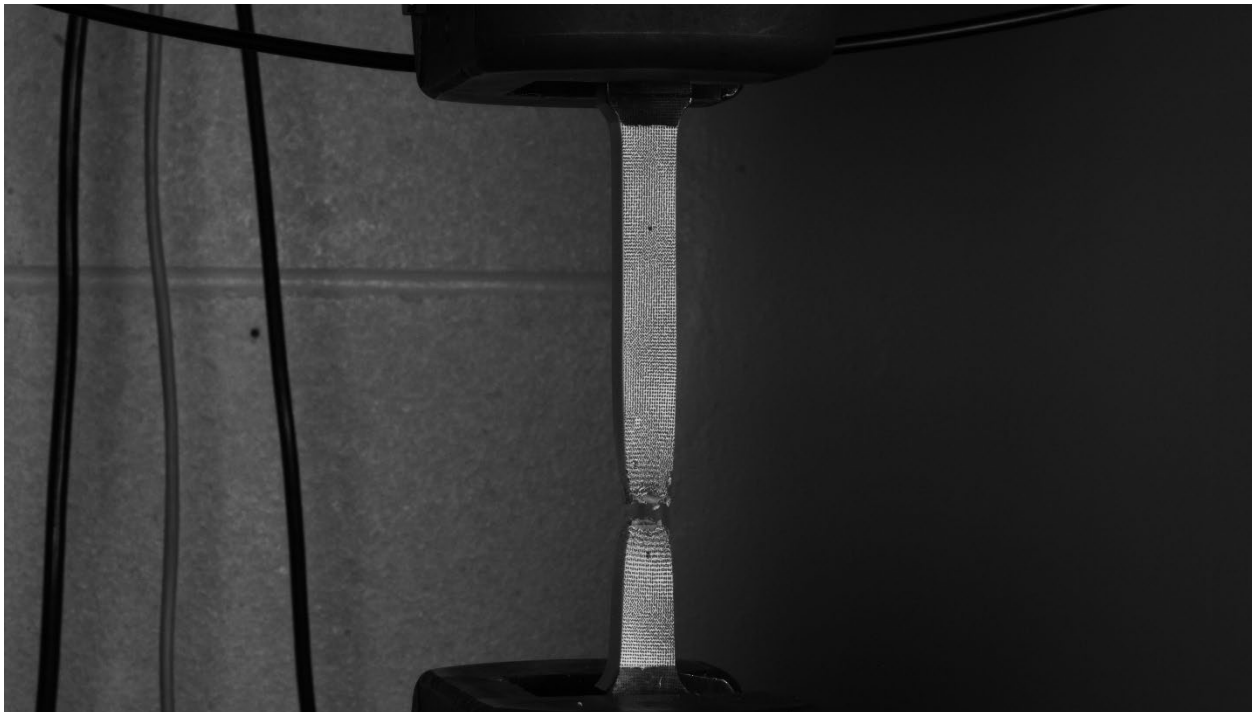
Source: FHWA.

**Figure 67. Photo. Specimen F80Lo-45-1 in UTM grips post fracture.**



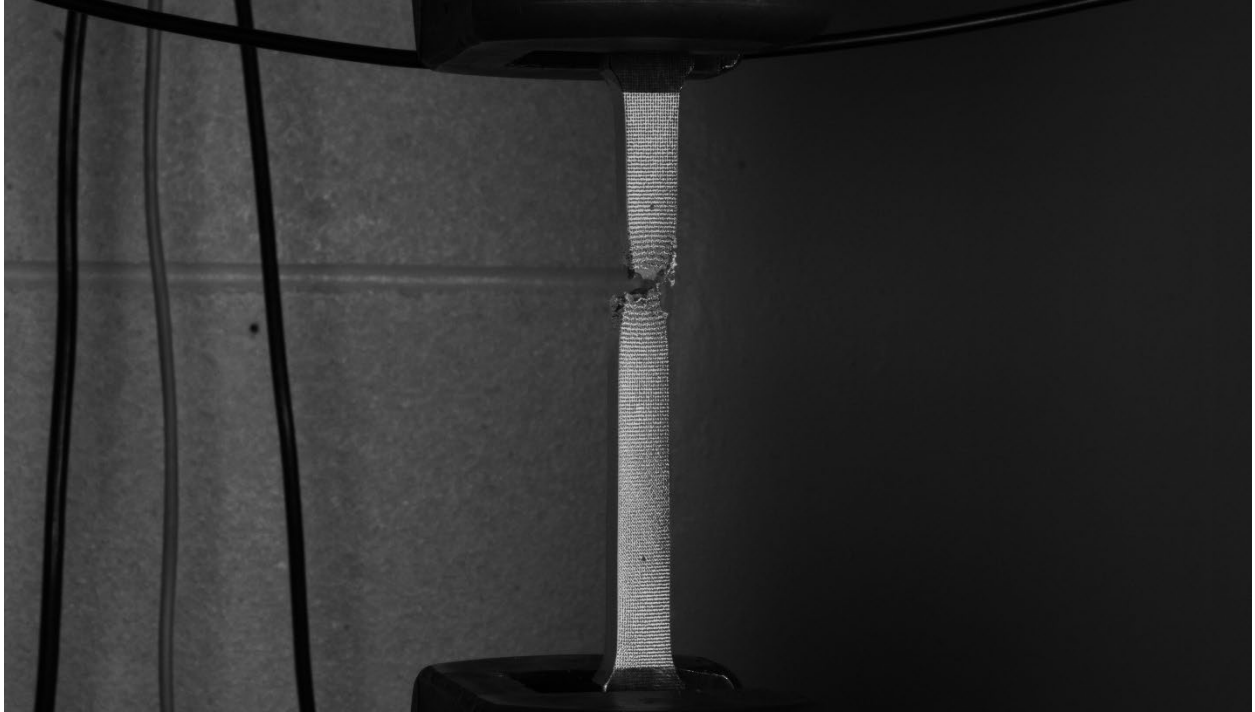
Source: FHWA.

**Figure 68. Photo. Specimen F80Lo-45-2 in UTM grips post fracture.**



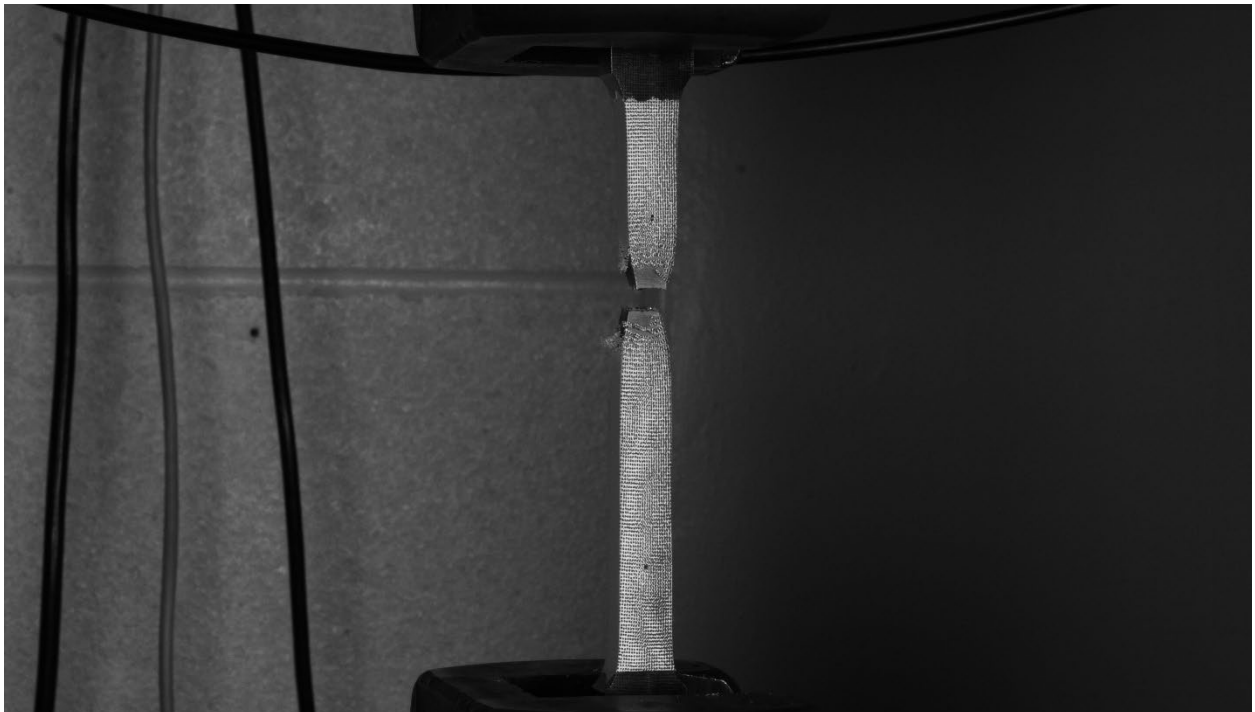
Source: FHWA.

**Figure 69. Photo. Specimen F80Lo-45-3 in UTM grips post fracture.**



Source: FHWA.

**Figure 70. Photo. Specimen F80Hi-BD-1 in UTM grips post fracture.**



Source: FHWA.

**Figure 71. Photo. Specimen F80Hi-BD-2 in UTM grips post fracture.**



Source: FHWA.

**Figure 72. Photo. Specimen F80Hi-BD-3 in UTM grips post fracture.**



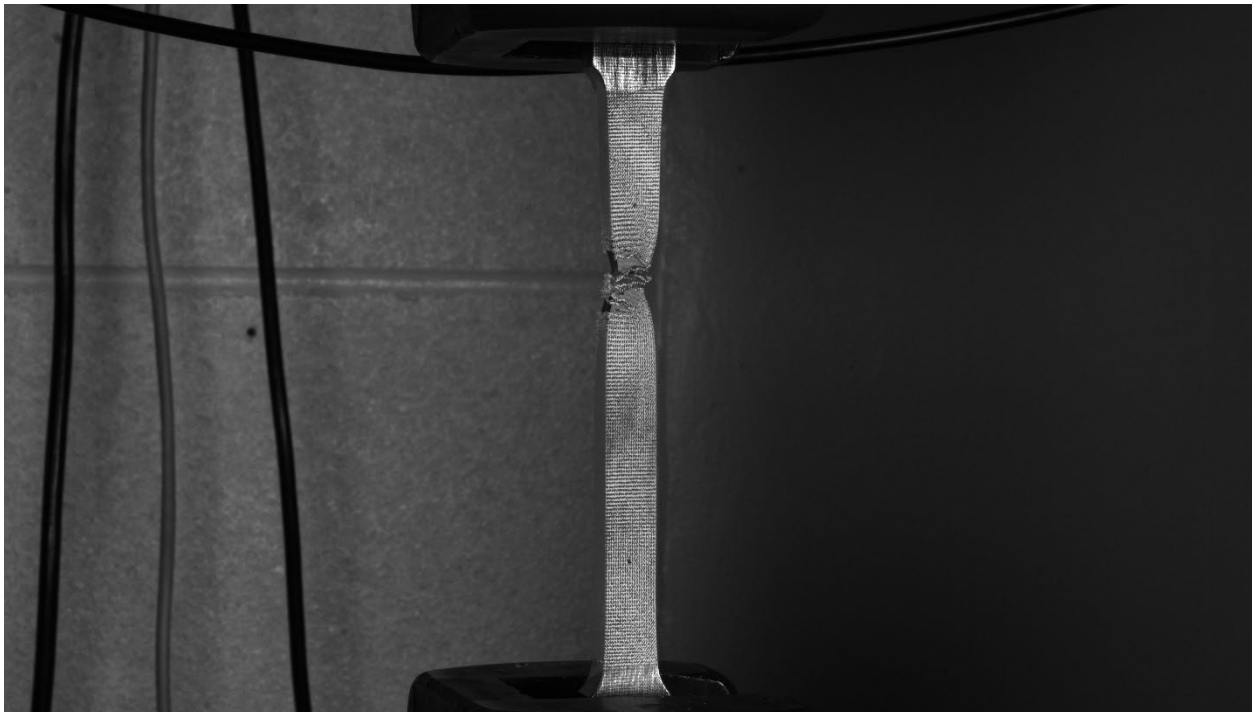
Source: FHWA.

**Figure 73. Photo. Specimen F80Hi-DD-1 in UTM grips post fracture.**



Source: FHWA.

**Figure 74. Photo. Specimen F80Hi-DD-2 in UTM grips post fracture.**



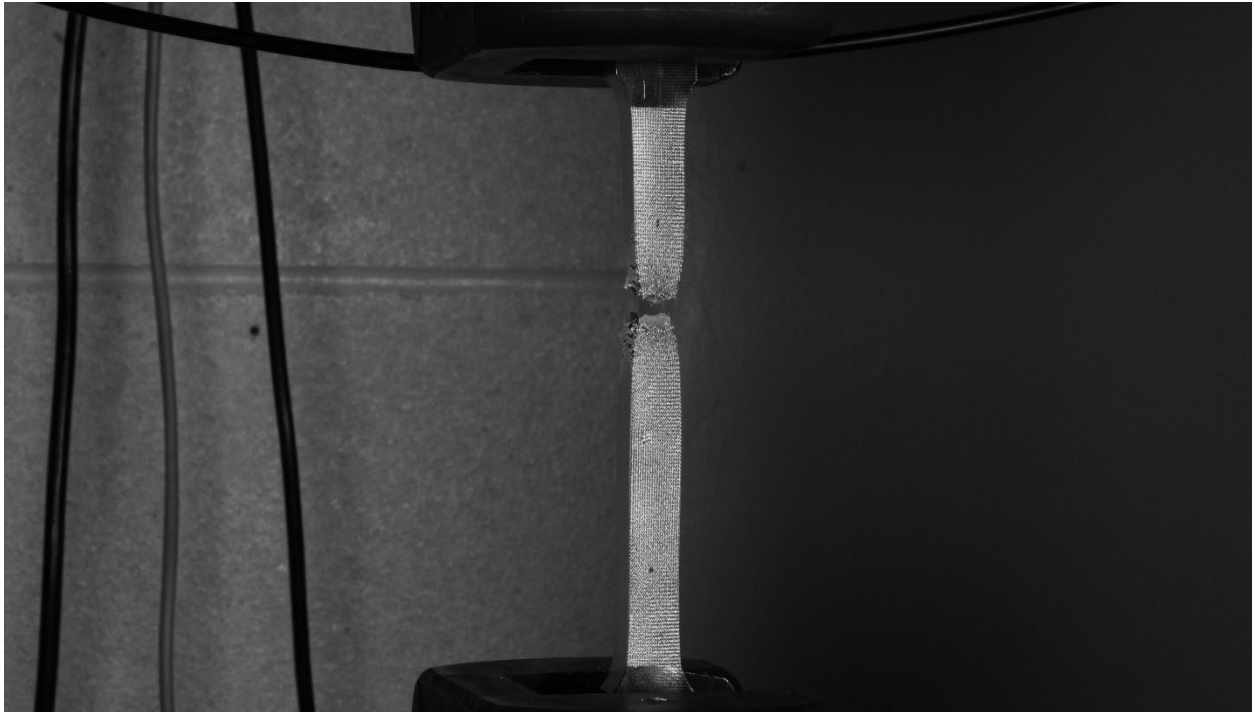
Source: FHWA.

**Figure 75. Photo. Specimen F80Hi-DD-3 in UTM grips post fracture.**



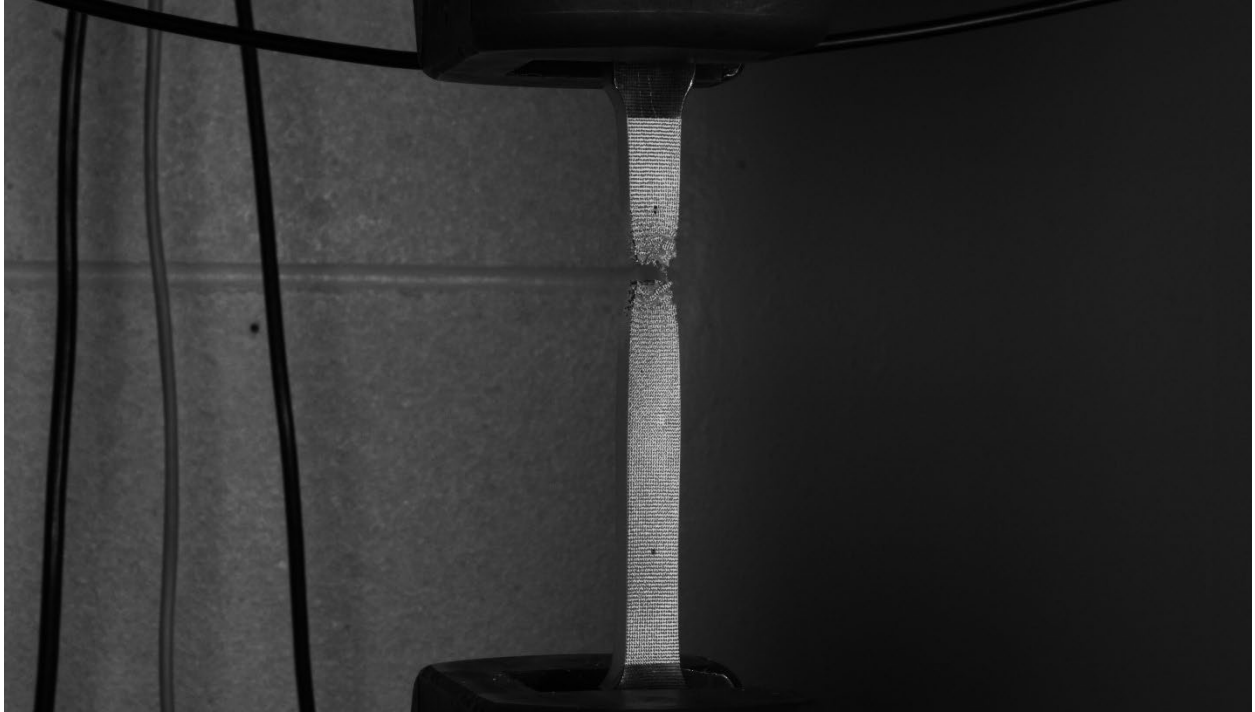
Source: FHWA.

**Figure 76. Photo. Specimen F80Hi-45-1 in UTM grips post fracture.**



Source: FHWA.

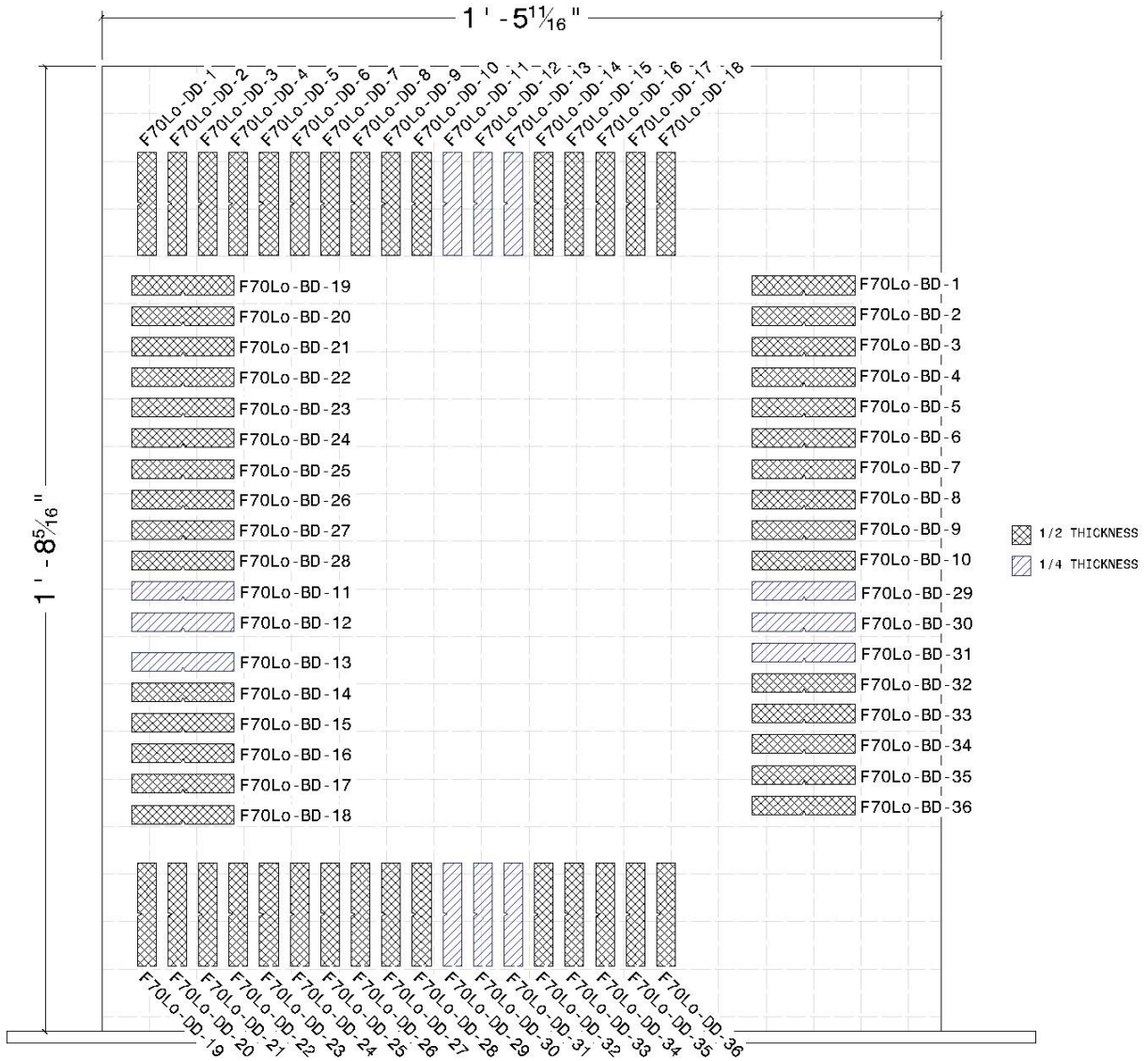
**Figure 77. Photo. Specimen F80Hi-45-2 in UTM grips post fracture.**



Source: FHWA.

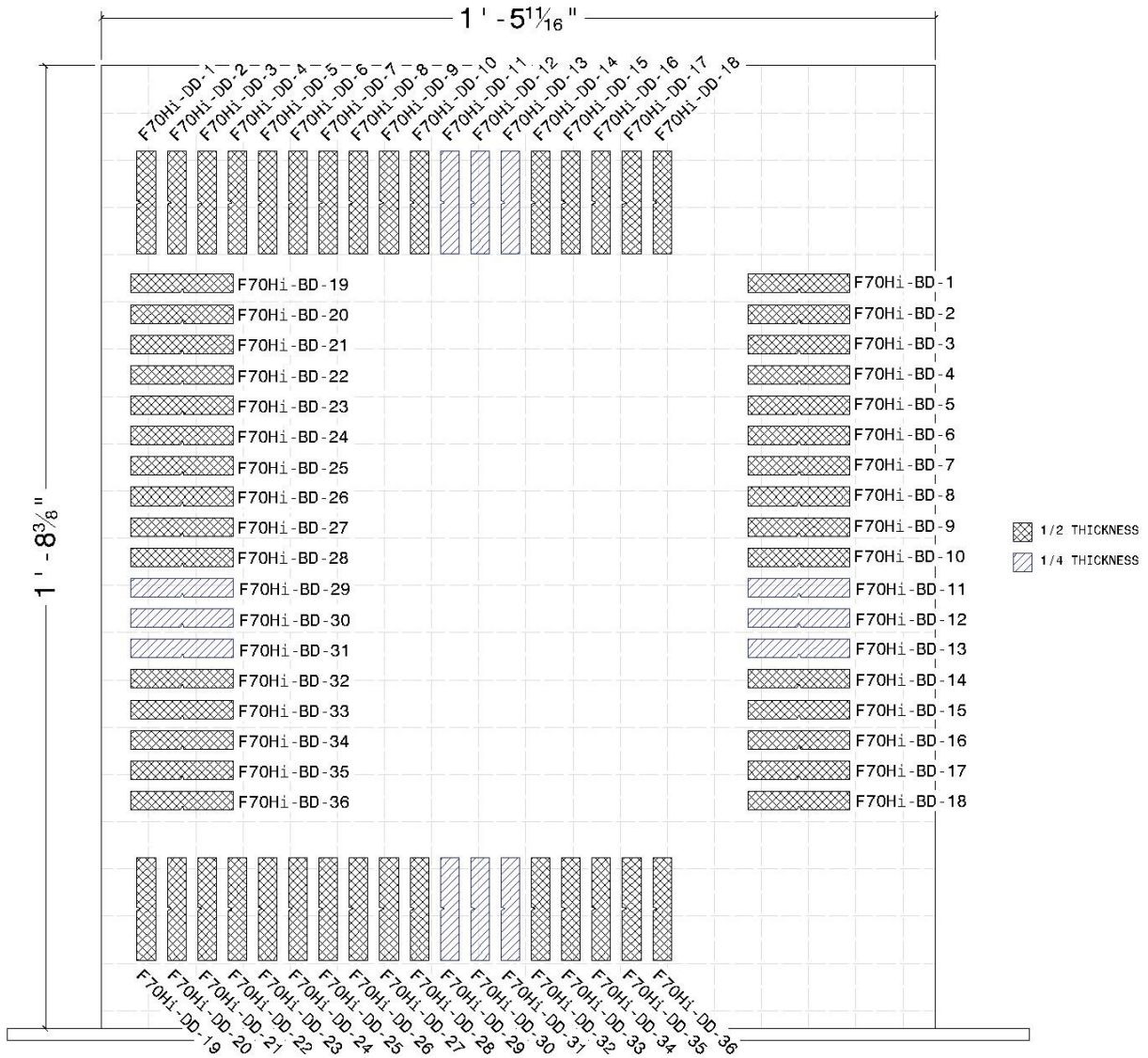
**Figure 78. Photo. Specimen F80Hi-45-3 in UTM grips post fracture.**

## APPENDIX C: CVN LOCATIONS IN EACH WALL



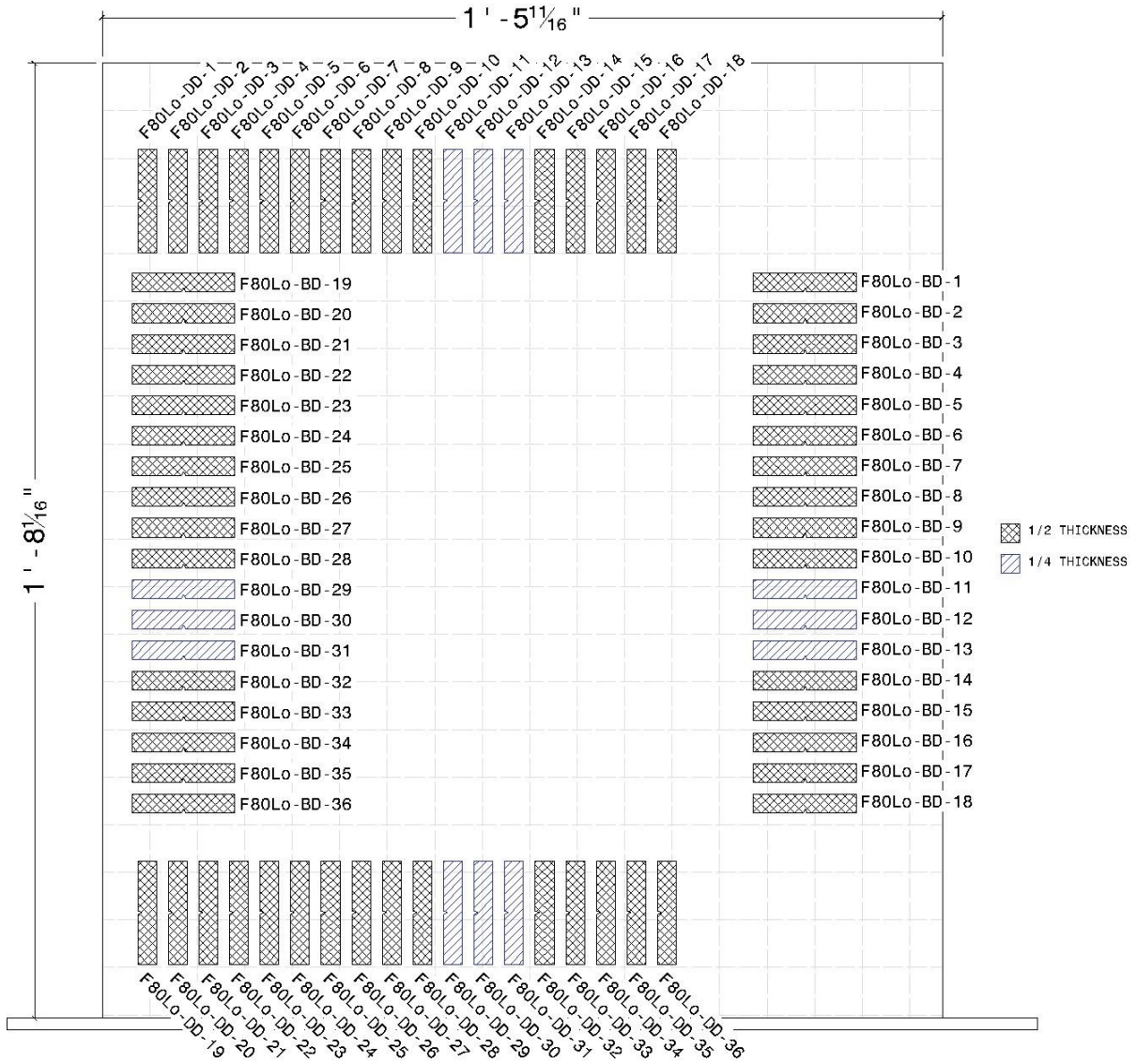
Source: FHWA.

**Figure 79. (Drawing). Approximate locations from which CVN specimens were removed from F70Lo.**



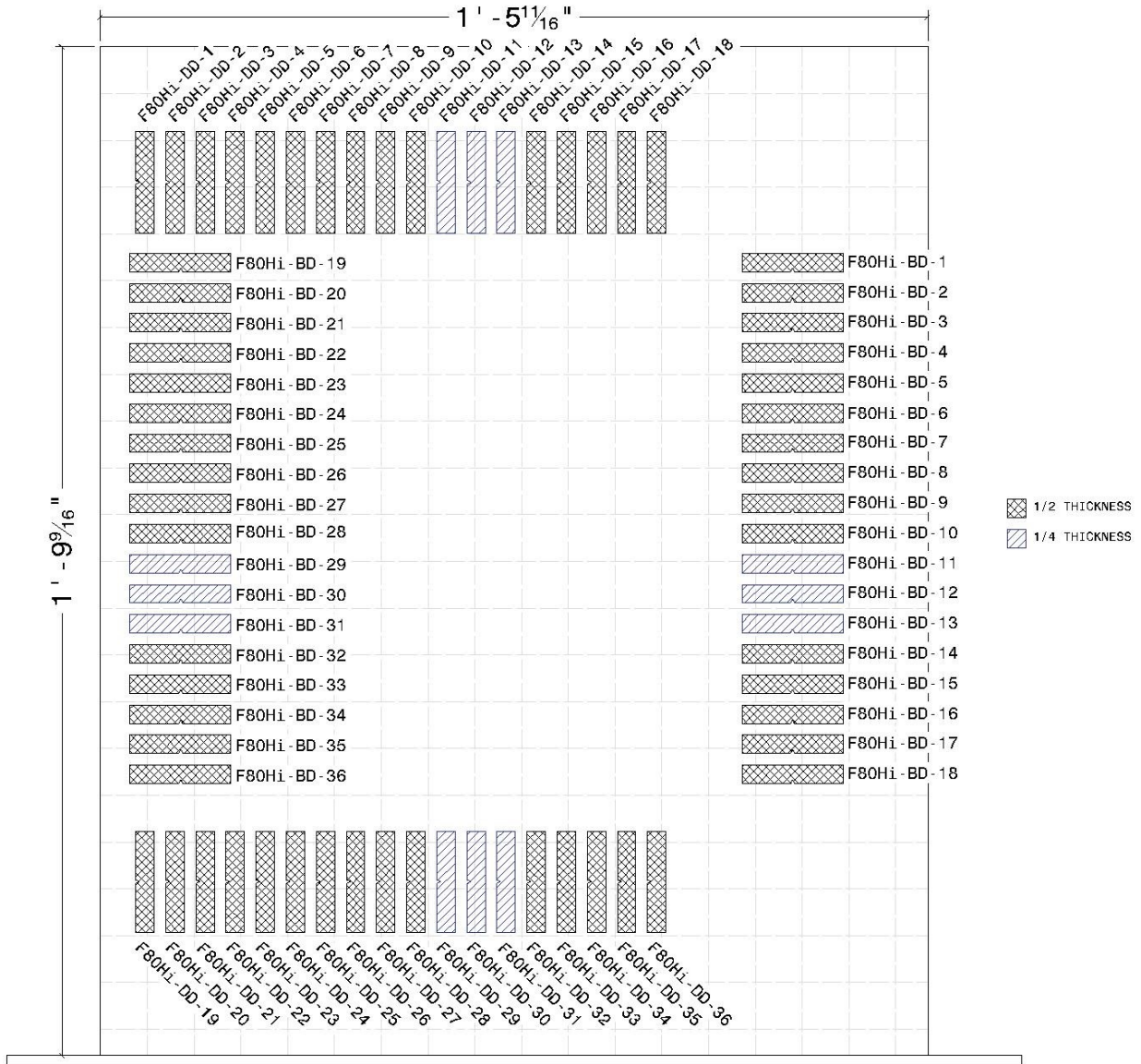
Source: FHWA.

**Figure 80. (Drawing). Approximate locations from which CVN specimens were removed from F70Hi.**



Source: FHWA.

**Figure 81. (Drawing). Approximate locations from which CVN specimens were removed from F80Lo.**



Source: FHWA.

**Figure 82. (Drawing). Approximate locations from which CVN specimens were removed from F80Hi.**